



HAL
open science

Polarimetry of the polarized hydrogen deuteride HDice target under an electron beam

Vivien Laine

► **To cite this version:**

Vivien Laine. Polarimetry of the polarized hydrogen deuteride HDice target under an electron beam. Other [cond-mat.other]. Université Blaise Pascal - Clermont-Ferrand II, 2013. English. NNT : 2013CLF22394 . tel-00975926

HAL Id: tel-00975926

<https://theses.hal.science/tel-00975926>

Submitted on 9 Apr 2014

HAL is a multi-disciplinary open access archive for the deposit and dissemination of scientific research documents, whether they are published or not. The documents may come from teaching and research institutions in France or abroad, or from public or private research centers.

L'archive ouverte pluridisciplinaire **HAL**, est destinée au dépôt et à la diffusion de documents scientifiques de niveau recherche, publiés ou non, émanant des établissements d'enseignement et de recherche français ou étrangers, des laboratoires publics ou privés.

Université Blaise Pascal

U.F.R. Sciences et Technologies

ÉCOLE DOCTORALE DES SCIENCES FONDAMENTALES
N° 768

THÈSE

présentée pour obtenir le grade de

DOCTEUR D'UNIVERSITÉ

Spécialité: Physique corpusculaire

Par

Vivien LAINE

POLARIMETRY OF THE POLARIZED HYDROGEN
DEUTERIDE HDICE TARGET UNDER AN ELECTRON
BEAM

Soutenue publiquement le 21 novembre 2013, devant la commission d'examen:

M ^{lle} Hélène FONVIELLE	<i>Président du Jury</i>
M. Andrew SANDORFI	<i>Rapporteur</i>
M. Eric VOUTIER	<i>Rapporteur</i>
M. Jacques BALL	<i>Examineur</i>
M. Louis-Pierre SAYS	<i>Examineur</i>
M. Alexandre DEUR	<i>Directeur de thèse</i>

Abstract

The study of the nucleon structure has been a major research focus in fundamental physics in the past decades and still is the main research line of the Thomas Jefferson National Accelerator Facility (Jefferson Lab). For this purpose and to obtain statistically meaningful results, having both a polarized beam and a highly efficient polarized target is essential. For the target, this means high polarization and high relative density of polarized material.

A Hydrogen Deuteride (HD) target that presents both such characteristics has been developed first at Brookhaven National Lab (BNL) and brought to the Hall B of Jefferson Lab in 2008. The HD target has been shown to work successfully under a high intensity photon beam (BNL and Jefferson Lab). However, it remained to be seen if the target could stand an electron beam of reasonably high current (nA). In this perspective, the target was tested for the first time in its frozen spin mode under an electron beam at Jefferson Lab in 2012 during the g14 experiment.

This dissertation presents the principles and usage procedures of this HD target. The polarimetry of this target with Nuclear Magnetic Resonance (NMR) during the electron beam tests is also discussed. In addition, this dissertation also describes another way to perform target polarimetry with the elastic scattering of electrons off a polarized target by using data taken on helium-3 during the E97-110 experiment that occurred in Jefferson Lab's Hall A in 2003.

Résumé

L'étude de la structure du nucléon est un sujet actif de la recherche et un des objectifs majeurs du Thomas Jefferson National Accelerator Facility (Jefferson Lab). Une cible et un faisceau hautement polarisés sont essentiels afin d'obtenir suffisamment de données pour en extraire des observables avec une précision acceptable. C'est le cas du faisceau d'électrons délivré par l'accélérateur à Jefferson Lab qui remplit amplement cette condition avec un faisceau polarisé à près de 85%. Pour la cible, outre une grande polarisation, une densité de matériel polarisé (facteur de dilution) élevée est nécessaire. Cette thèse présente une cible de deutérum d'hydrogène, ou cible de HD, qui remplit ces deux conditions. Deux méthodes de polarimétrie sont également décrites: une par Résonance Magnétique Nucléaire (RMN) appliquée à la cible de HD pendant des tests sous un faisceau d'électrons durant l'expérience g14 en 2012 dans le Hall B de Jefferson Lab. La seconde utilise la réaction de diffusion élastique d'un faisceau d'électrons sur une cible gazeuse polarisée. Nous l'avons appliquée avec des données élastiques sur l'hélium-3 prises en 2003 pendant l'expérience E97-110 dans le Hall A de Jefferson Lab.

La cible de HD est une cible polarisée à "spin gelé" (i.e. sa polarisation ne change pas ou très peu dans le temps), dont les deux noyaux sont polarisés ($P_H \sim 60\%$ et $P_D \sim 15-30\%$). La cible est cryogénique et à l'état solide, sa température opérationnelle est d'environ 80 mK. Elle est composée à 77% de molécules de HD (les 23% restant étant des fils d'aluminium pour évacuer la chaleur de la cible et le plastique constituant l'extérieur de la cible). De fait son facteur de dilution est l'un des plus élevés des cibles polarisées actuelles. Une autre caractéristique qui rend la cible de HD si attractive est son temps de relaxation qui évolue avec le temps: d'abord très court (quelques secondes) quand la cible est créée, il augmente avec le temps quand la cible est placée à très basse température et peut atteindre plusieurs années. (Le temps de relaxation est le taux de recouvrement de la polarisation vers

l'équilibre thermique et traduit la capacité d'une cible à conserver sa polarisation.) Un tel comportement du temps de relaxation est une nécessité pour pouvoir polariser la cible de HD et l'utiliser dans une expérience. En effet, la cible est polarisée en utilisant une méthode dite de "force brute" qui consiste à placer la cible à très basse température (10 mK) dans un champ magnétique de très forte magnitude (15 T). La cible se polarise rapidement due au temps de relaxation initialement court. Il reste à attendre deux à trois mois que le temps de relaxation de la cible augmente. Et contrairement à d'autres cibles couramment utilisées qui peuvent être polarisées dynamiquement et donc repolarisées durant une expérience, la cible de HD n'est polarisée qu'une seule fois durant sa phase de polarisation (début de vie de la cible) et ne peut donc pas être repolarisée par la suite. Seule la polarisation du deutéron peut être augmentée au prix d'une perte partielle de la polarisation du proton.

Par le passé, il a déjà été montré que la cible de HD pouvait être utilisée avec succès sous un faisceau de photons de haute intensité. Néanmoins, il restait à vérifier si la cible pouvait également supporter un faisceau d'électrons de courant relativement élevé (nA). Dans ce but et aussi afin d'acquérir davantage de données de photo-production, la cible a été transférée en 2008 de Brookhaven National Lab, où elle avait été originellement développée, à Jefferson Lab. Durant l'expérience g14 sous faisceau de photons à Jefferson Lab, deux tests sous faisceau d'électrons ont pu être réalisés et ont permis d'étudier et comprendre les pertes de polarisation sous un tel faisceau en suivant l'évolution de la polarisation de la cible par RMN. Au cours de ces tests, plusieurs effets de pertes de polarisation ont pu être identifiés, mais l'analyse a été rendue difficile par le fait que ces effets se cumulent et n'avaient pas nécessairement été prévus, du moins pas avec autant de poids. Ces effets sont entre autre l'ionisation du HD, la recombinaison des molécules de HD en molécules de H₂ et D₂, ainsi qu'une forte dépendance vis-à-vis de la température et du champ magnétique. Bien que ces tests ne permettent pas ultimement de confirmer ou non l'utilisation possible de la cible de HD sous un faisceau d'électrons, ils donnent néanmoins des pistes et améliorations à effectuer sur la cible afin d'atténuer fortement, voire de supprimer, ces effets néfastes de pertes de polarisation lors de futurs tests.

Lors des tests sous faisceau d'électrons de la cible de HD, une autre méthode de polarimétrie utilisant la réaction de diffusion élastique avait aussi été envisagée, mais la faible polarisation des cibles utilisées pendant ces tests avait rendu cela impossible. L'analyse des données de la cible d'hélium-3 de l'expérience E97-110 dans le Hall A de Jefferson Lab, également présentée dans cette thèse, avait pour but d'être un exercice pour une analyse similaire de la cible de HD. Une analyse de

ce type pour la cible d'hélium-3 était de plus nécessaire, car les différentes méthodes de polarimétrie utilisées (RMN et Résonance Paramagnétique Électronique, RPE) pour cette cible étaient en désaccord et la détermination de la polarisation par une méthode indépendante devait permettre de lever cette indétermination. Le résultat de cette analyse favorise les résultats de la RPE. Néanmoins, cette conclusion est affectée par l'incertitude statistique élevée.

En conclusion, la cible de HD a de nouveau prouvé lors de l'expérience g14 qu'elle était parfaitement adaptée aux faisceaux de photons. Néanmoins, des tests additionnels doivent encore être effectués afin de déterminer son utilisation sous un faisceau d'électrons. De tels tests pourraient avoir lieu de nouveau dans le Hall B de Jefferson Lab ou plus probablement dans le futur petit accélérateur d'électron qui devrait être installé dans le Test Lab de Jefferson Lab. En ce qui concerne la cible d'hélium-3, plusieurs expériences l'utilisant sont déjà prévues au sein des Hall A et C de Jefferson Lab.

Acknowledgments

First of all, I am deeply thankful to my advisor, Alexandre Deur, for his continuous help, support and numerous advices about work and life in general throughout my thesis. He took part and guided me on every aspect of my work (HDice target, E97-110 experiment, writing of this dissertation, etc). Without his support and efforts to pull me up, I would have most likely given up on my work many times. I am highly indebted to H el ene Fonvieille for having hosted me in her office a few months, not giving up on me and pushing me relentlessly so I would finish to write down this dissertation. I also want to thank the members of my thesis jury for every comments and corrections concerning my dissertation and above all for taking the time to read it.

I am thoroughly grateful to Andy Sandorfi for giving me the opportunity to work with him and his group on the HDice target, as well as for inviting me to his HDice dinners and my very first american 4th of July. And I am genuinely thankful to Volker Burkert, leader of JLab's Hall B, who also made this opportunity possible. Then, I want to thank Tsuneo Kageya, who I believe is the person of the HDice group that I worked the most with, for his patience, help and teaching me so many things in the most rigorous way, because there is no greater gift than the gift of knowledge. I also have another big thank to Xiangdong Wei for his kindness, help and taking a lot of his time to answer my questions (even the not-so-bright ones). Although I did not have the chance to work a lot with Michael Lowry, I developed over time great respect toward him. As well, I have really appreciated to work with Gary Dezern, without him we would not have been able to put the parts of the In-Beam Cryostat together. I want to thank Annalisa D'Angelo for the year she spent working with the HDice group, because working with her was always pleasant. I am thankful to Werth Teachey for his help while I was building the second NMR rack and for letting me intruding in his office when I was looking for parts. I am pleased I worked with

Christopher Bass, Charles Hanretty and Thomas O'Connell, as well as Dao Ho, Peng Peng and Natalie Walford, who shared with me the babysitting of the target for quite some time. Eventually, I really enjoyed to work alongside with the Hall B tech crew, especially Calvin Miller.

I am very appreciative of Jian-Ping Chen and Vincent Sulkosky for welcoming me on the analysis of the E97-110 experiment data. Although it was at the beginning only an exercise for the HDice target, I am satisfied that I could learn a lot about another polarized target and computer simulation.

Furthermore, I am thankful to other people I met at Jefferson Lab or Clermont-Ferrand. First, the french community of Jefferson Lab so I was not eating on my own and I could have great discussion with people during lunch, people such as (and I am probably forgetting many of them): Jacques Ball, Alexandre Camsonne, Eric Fuchey, François-Xavier Girod, Florian Itard, Piotr Konczykowski, Mehdi Meziane, Taya Mineeva, Yohann Perrin, Lionel Quettier, Eric Voutier, etc. With an extra thank to Yohann and Mehdi for being such good roommates. Then, I would like to thank the people who work at the Quark Cafe at Jefferson Lab for their kindness, especially Patty Barry who always had a word to cheer me up. Finally, I am pleased I could share the office at Clermont-Ferrand with someone as nice as Loup Correa.

Retrospectively, I am really happy and feel lucky that I had the chance to meet and work with such great people. I know I have a lot of ups and downs, and that I am not easy to live with every day, thus I would like to thank everybody I have met until now for putting up with me.

Table of contents

Abstract	iii
Résumé	iv
Acknowledgments	vii
Table of Contents	ix
List of figures	xii
List of Tables	xv
Introduction	1
1 Theoretical aspects	6
1.1 Polarized scattering experiments and polarized targets	6
1.1.1 Motivations	6
1.1.1.1 Inclusive experiments	7
1.1.1.2 Elastic scattering on nuclei	10
1.1.1.3 Exclusive (and semi-inclusive) experiments with multi- particle final states	10
1.1.2 Overview of polarized targets	11
1.2 Polarimetry	15
1.2.1 Introduction	15
1.2.2 Nuclear Magnetic Resonance polarimetry	17
1.2.2.1 Principle	17
1.2.2.2 Adiabatic fast passage	19
1.2.3 Electron paramagnetic resonance	20

TABLE OF CONTENTS

1.2.4	Polarimetry using electron scattering asymmetry	21
2	HDice target	22
2.1	Target cell and HD material	22
2.1.1	Description	22
2.1.2	Target cell design	23
2.1.3	HD material	24
2.1.3.1	Relaxation	24
2.1.3.2	Gas purification	26
2.1.3.3	Gas characterization	27
2.2	Cryostats	27
2.2.1	General description	28
2.2.2	Production dewar	29
2.2.3	Transfer cryostat	31
2.2.4	Dilution fridge	32
2.2.5	Storage dewar	33
2.2.6	In-beam cryostat	34
2.3	Target life	35
2.3.1	Overview	35
2.3.2	Condensing the target	37
2.3.3	Thermal equilibrium calibration	37
2.3.4	Transfer between dewars	38
2.3.5	Polarizing and aging	39
2.3.6	Polarization measurement	41
2.3.7	Transport to hall	41
2.3.8	Final polarization measurement	42
2.3.9	Gas collection and storage	42
3	Experiment with the HDice target	43
3.1	Motivations	43
3.1.1	Photon beam run	43
3.1.2	Electron beam test runs	44
3.2	Experimental setup	45
3.2.1	Accelerator Facility	45
3.2.2	Hall B	46
3.2.2.1	Beam-line	47
3.2.2.2	Target	49
3.2.2.3	CLAS detector	49

TABLE OF CONTENTS

4	Polarimetry technical aspects	52
4.1	HDice NMR system	52
4.1.1	Apparatus	52
4.1.2	Fast resonance scan - System response	54
4.1.3	NMR measurements	55
4.1.3.1	Field sweeps	55
4.1.3.2	Frequency sweeps	57
4.2	T_1 measurements	57
4.3	Spin transfer	59
4.4	Spin transfer improvement	62
4.4.1	Field homogeneity definition	62
4.4.2	Birdcage coil project	62
5	Behavior of HD under electron beams	69
5.1	Introduction	69
5.1.1	Fourier transform	69
5.1.2	Kramers-Kronig relations	71
5.2	Polarization extraction	72
5.2.1	Signal normalization	72
5.2.2	Baseline correction	74
5.2.3	Y channel signal transformation	75
5.2.4	Integration of the signal	76
5.2.5	Error estimation	77
5.3	Polarization results	78
6	Polarimetry with electron scattering	87
6.1	Experiment details	88
6.2	Polarization extraction	89
6.2.1	Simulation	89
6.2.2	Data selection and polarization calculation	90
6.3	Polarization results	94
	Conclusions	100
	A Acronyms list	102
	References	

List of Figures

1.1	First order Feynman diagram for an electron scattering off a nucleon or a nucleus.	8
1.2	Energy level splitting, for $S=1/2$	16
1.3	Thermal equilibrium polarizations of hydrogen and deuterium versus magnetic field over temperature ratio (B/T).	18
1.4	Radio frequency transitions in a nucleus of spin $S=1/2$	20
2.1	HDice target cell schematic.	23
2.2	Spin exchanges between ortho- H_2 (and para- D_2) and H (and D) nuclei in the HD molecule. The amounts of ortho- H_2 (initially 75% of the H_2 content) and para- D_2 (initially 33% of the D_2 content) decay with a lifetime of 6.3 and 18.6 days respectively.	25
2.3	Schematic of the Production Dewar.	30
2.4	Flow schematic of the dilution refrigerator.	33
2.5	Schematic of the In-Beam Cryostat in transfer configuration (vertical orientation on the left) and in experimental configuration (horizontal orientation on the right).	35
2.6	HDice target life cycle	36
2.7	Evolution of the proton polarization in the DF to its thermal equilibrium with the aging time. Figure, courtesy of A. Sandorfi.	40
3.1	Schematic representation of the Jefferson Lab accelerator, including the 12 GeV upgrade.	45
3.2	Schematic of the Hall B beamline in photon run configuration.	47
3.3	Schematic of the HDice target in CLAS in the electron run configuration.	48
3.4	Side view of CLAS with its different subsystems.	50
3.5	Front view of CLAS with its different subsystems.	50

LIST OF FIGURES

4.1	Schematic of the NMR system used for the HDice target.	54
4.2	Example of a fast resonance scan in the PD.	55
4.3	Passage through the NMR resonance (twice) during a field sweep (hydrogen). The top plot shows the magnetic field sweep and the bottom one the response of the receiver coil. The NMR resonance occurs at B_0 and induce the peaks.	56
4.4	T_1 measurement of a short relaxation time target (deuterium).	58
4.5	Schematic of the NMR system used with the Qualifier for the HDice target.	59
4.6	Energy level splitting and transitions between levels in HD.	60
4.7	Representations of the 2-pole saddle coils in the PD.	64
4.8	Representation of the 8-pole birdcage coils in the IBC. Some posts have two turns to create a stronger magnetic field.	65
4.9	Simulation with MicroWave Studio of the magnetic field created by an 2-pole saddle coil in the xy plane in the middle of the coil.	66
4.10	Simulation with MicroWave Studio of the magnetic field created by an 8-pole birdcage coil in the xy plane in the middle of the coil. The magnetic field is higher around the four 2-turn posts (top and bottom posts).	67
4.11	Drawing of the birdcage coil form in the IBC.	68
5.1	Fourier Transform of an NMR signal (Lock-in X channel).	70
5.2	Kramers-Kronig transformation of an NMR signal (Lock-in X channel).	71
5.3	Correction of the baseline of an NMR signal (Lock-in X channel).	74
5.4	Correction of the exponential decay in an NMR signal (Lock-in Y channel).	75
5.5	Transformation of a Y channel NMR signal.	76
5.6	HDice target polarization for H from NMR measurements during the first electron run. The yellow areas represent the periods of exposure of the target to the electron beam.	82
5.7	Idem as figure 5.6 but for D.	83
5.8	HDice target polarization for H from NMR measurements during the second electron run. The yellow areas represent the periods of exposure of the target to the electron beam.	85
5.9	Idem as figure 5.8 but for D.	86
6.1	Schematic of the E97-110 experimental setup (target area).	88
6.2	y_{tg} VS ϕ_{tg} before and after collimators cuts for run 2441 (6° , 2.1GeV).	92
6.3	Target coordinate in the Hall A HRS system.	93

LIST OF FIGURES

6.4	Comparison between experimental and simulated data for kinematics variables with asymmetry cuts for run 2441 (6° , 2.1GeV).	93
6.5	Hall A ^3He experiment E97-110 polarizations from asymmetries at 6° and 2.1 GeV.	95
6.6	Hall A ^3He experiment E97-110 polarizations from asymmetries at 6° and 2.8 GeV.	96
6.7	Hall A ^3He experiment E97-110 polarizations from asymmetries at 9° and 1.1 GeV.	97
6.8	Hall A ^3He experiment E97-110 polarizations from asymmetries at 9° and 2.2 GeV.	98
6.9	E97-110 polarizations ratios formed with the polarization extracted from the elastic reaction over the NMR or EPR results.	99

List of Tables

1.1	Summary of the different polarizable targets, their dilution factor f , typically achievable target polarization P_t , typical beam current that can be used I , and in-beam magnetic fields B	14
1.2	Calculated thermal equilibrium polarizations of hydrogen and deuterium at different magnetic field over temperature ratio (B/T). . . .	19
5.1	Beam exposures of the target during the first electron test period. . .	81
5.2	Magnetic field and temperature conditions of NMR measurements taken in between electron exposures during the first electron test period.	81
5.3	Beam exposures of the target during the second electron test period. .	84
5.4	Magnetic field and temperature conditions of NMR measurements taken in between electron exposures during the second electron test period.	84
6.1	Kinematic cuts for the asymmetry calculations.	92

Introduction

Our description of Nature is based on a small number of fundamental elements:

- Four fundamental forces (or interactions): electromagnetic, strong, weak and gravitational forces.
- Broken symmetries: Dynamical Chiral Symmetry Breaking, which accounts for about 98% of the visible mass of the universe. (The Higgs field accounts for less than 2%.)
- A few fundamental particles: the electron, the up (u) and down (d) quarks and the electronic neutrino (ν_e) (as well as 2 heavier versions of this family), and the Higgs particle (most likely now observed at the Large Hadron Collider (LHC) [1]).
- Two, not yet well understood, phenomena: Dark matter and dark energy.

Of the four fundamental forces, only the strong force is not well understood in the presently experimentally accessible domain¹. For instance, it is not satisfactorily known why quarks are never found isolated, but always confined by the strong force within two kinds of hadrons: Baryons (three valence quarks) and mesons (valence quark and antiquark). Only two of these baryons are stable: the proton (uud valence structure) and the neutron² (udd), collectively called “nucleons”. They are, with the electrons, the building blocks of the visible matter.

¹Gravity is not well understood at the quantum level, but this is far from being experimentally accessible.

²The neutron is stable only when it is embedded in nuclear matter. Free neutrons have a lifetime of about 15 minutes.

INTRODUCTION

Therefore, an understanding of the properties of matter, at the fundamental and nuclear level, requires knowledge of the behavior of quarks and the strong force. However, the task is rendered difficult because the magnitude of the strong force is typically very large. Consequently, the usual theoretical tool of quantum field theory -perturbation theory- cannot be used. One possibility is to use the unusual property of the strong force at high energy, the asymptotic freedom, that causes the magnitude of the force to decrease at small distances (i.e. high energy). This feature enables the application of perturbation theory in Deep Inelastic Scattering (DIS) processes [2] and has allowed studies of the nature of the strong force and the distribution of quarks and gluons in the nucleon at small distances. Thanks to DIS it was established that the strong interaction can be described by Quantum ChromoDynamics (QCD), a quantum field theory of the strong interaction. In the QCD theory, quarks carry one of three different color charges and the interaction is mediated by gluons (massless bosons carrying a color and an anti-color charge). However important DIS is to our knowledge of the strong force and of the short-distance quark distribution, it does not inform us directly about quarks and QCD at low energy (confinement regime). This is still not well understood at the theoretical level and the nature of confinement remains one of the most important questions in fundamental physics [3].

To study confinement, several approaches have been actively explored:

1. Computational non-perturbative calculations of QCD, such as lattice QCD [4]. These calculations are the closest to full QCD, particularly for the nucleon in the confinement regime. However, the method has caveats, because to obtain results in a reasonable time, different approximations need to be done which can produce spurious effects. Numerical calculations of lattice QCD can be extremely computationally intensive; in conditions close to those found in nature, calculations can last weeks even with the most powerful computers. Some observables are too computationally intensive to be calculable.
2. Analytical non-perturbative calculations of QCD. These methods necessitate approximations or/and assumptions due to the important non-linear nature of the strong interaction. Three leading non-perturbative analytical approaches, which are often used in concert with lattice QCD, are:
 - Chiral Perturbation Theory [5]: This uses the effective (i.e. non-fundamental) degrees of freedom of baryons and mesons instead of quarks and gluons. It is a perturbative method based on the approximate chiral symmetry

of the strong interaction or, equivalently, the fact that quarks have small masses (MeV) compared to hadron masses (at hundreds of MeV) and the scale of confinement (a few hundreds of MeV).

- Schwinger-Dyson equations [6]: These provide an infinite set of relations between the Green functions of QCD (or any quantum field theory). To solve them, the infinite set must be truncated, which leads to approximate solutions of QCD. However, the choice of truncation can again induce spurious effects that need to be identified and controlled. Comparisons of solutions of the Schwinger-Dyson equations with Lattice-QCD calculations have demonstrated how mass appears at low momenta from dynamical Chiral symmetry breaking [7].
- AdS/CFT relation [8]: This approach takes advantage of a relation between gravity in a five-dimensional (5D) Anti-de Sitter (AdS) space-time and a conformal field theory limited to the four-dimensional (4D) boundary of the AdS space-time. This 4D boundary corresponds to our usual space-time. An AdS space is a space with an intrinsic negative curvature. A Conformal Field Theory (CFT) is a theory for which the force's magnitude does not change with distance. This is the case for QCD at small distances (DIS scaling, due to asymptotic freedom [9] [10] [11]) but also at large distances, below the confinement scale. Hence, weak field gravity calculations in AdS can be used to predict the non-perturbative behavior of QCD at large distance³.

3. Models of the hadron structure. Many models exist and are used to understand the quark structure of hadrons. The most widely used model, and also the oldest approach used to understand the non-perturbative quark behavior, is the Constituent Quark Model (CQM) [12]. In this model, hadrons are made of two or three “constituent” quarks. Constituent quarks are “dressed” valence quarks (“current” quarks surrounded by clouds of gluons and quark/anti-quark pairs from the Dirac sea⁴) bounded together by collapsed “flux tubes” of gluons. They share the same quantum numbers as the real (or “current”) quarks, but their mass is considerably higher (about the third of the nucleon mass). The

³Conversely, perturbative QCD calculations (e.g. DIS) are also used to understand strong gravity (e.g. near a black hole).

⁴The Dirac sea is a theoretical model of the vacuum. The vacuum is seen as an infinite sea of particles with negative energies.

constituent quark model has been very valuable for a general understanding of how many of the properties of hadrons arise from confinement and the symmetries of QCD, particularly the excited hadron spectra. However, this model also predicts excited states (resonances) that have never been seen. Other models, such as quark/di-quark models of the nucleon, do not predict them. The comprehension of the excited spectrum of the hadron would bring us a long way toward understanding confinement, since the spectrum is directly resulting from QCD in its non-perturbative regime.

4. A fourth way to study QCD and confinement is to explore how phenomena evolve from the analytically calculable and well known DIS domain to the more mysterious confinement domain. This can be achieved using appropriate observables that can be defined at all distance/energy scales. The leading tool for such an endeavor is Sum Rules [13], which are relations that link a static property of the nucleon (such as its mass or its anomalous magnetic moment) to a dynamical quantity (such as a scattering cross section).

Our contribution to the experimental investigations of two of these approaches (CQM and Sum Rules) will be discussed in this dissertation.

Recently, Lattice QCD calculations have confirmed the CQM predictions for many more excited states that have yet to be observed experimentally [14]. Such states are expected to be very short lived, and because of the time-energy uncertainty principle, will manifest themselves as broad overlapping resonances that can only be disentangled through Partial Wave Analyses (PWA). Ambiguities in PWA, which are bound to occur when different components overlap, can only be overcome by constraints from measurements of large numbers of different spin asymmetries [15]. The initial reaction state can be controlled by specifying the polarization of the beam (photons or electrons) and the polarization of the target nucleon. In addition, the decay of resonances through the production of hyperons, whose weak-decay distribution determines their final state polarization, provides unique opportunities to apply maximal constraints in the search for new resonances. This has already been done in the past (e.g. experiment with the FROzen Spin Target (FROST) [16] that occurred in Jefferson Lab's Hall B). However, a highly efficient target is needed to obtain statistically meaningful results for all useful reactions. This means high polarization (like FROST [16] or Dynamic Nuclear Polarization (DNP) [17] type targets) and high relative density of polarized material (unlike FROST and DNP-type targets). A Hydrogen Deuteride (HD) target that presents both such

INTRODUCTION

characteristics has been developed first at BNL [18] and brought to the Hall B of Jefferson Lab (JLab) in 2008. Much work was necessary to adapt the target to the new JLab conditions and to improve it. The target was then used with a photon beam to search for missing excited nucleon states during the g14 experiment[19]. It was also tested for the first time under an electron beam. In this dissertation, we will describe our contribution to the preparation and use of the HD target at JLab, in particular to the domain of the HD polarimetry.

Polarization is also fundamental for some of the Sum Rule studies; again, using polarized beams and targets adds extra degrees of freedom to constrain better our understanding of QCD. Such programs have been on-going in JLab Hall B (DNP-type targets) and Hall A (polarized gaseous ^3He targets). In the second part of this dissertation, we will describe our contribution to the polarimetry of the polarized ^3He target of Hall A.

Chapter 1

Theoretical aspects

1.1 Polarized scattering experiments and polarized targets

1.1.1 Motivations

The canonical tool to investigate deep into matter is to scatter a beam of particles off a target containing the material to study (see section 1.1.2). The energy of the incident particles determines the minimal distance probed. The method was pioneered by Rutherford in 1910 and led to the discovery of the atom's nucleus. Rutherford observed the scattering of alpha particles (${}^4\text{He}$) through a thin foil of gold. Energies of the order of GeV are necessary to access the excited states of the nucleon and its quark content.

Many types of beams are available: photon beams, lepton (electrons, muons, positrons, etc) beams or hadronic (protons, neutrons, light or heavy ions, pions, kaons, etc) beams. Hadronic beams have the advantage of interacting strongly with targets hence yielding large cross sections. However, except in rare cases such as the Drell-Yan reaction [20] [21], the non-perturbative interaction of the beam with the target and the structure of the probing particles make the interpretation of the results more delicate. Photon and lepton beams have less probable interactions with

targets but these structureless particles offer a cleaner interpretation of the reaction.

In this dissertation, we will discuss some of the targets used and experiments that used them at Thomas Jefferson National Accelerator Facility (TJNAF), a particle accelerator located in Virginia, United States. TJNAF, commonly called Jefferson Lab, is an electron accelerator designed to probe matter with a 1-6 GeV continuous electron beam (see section 3.2.1). The beam, targets and detectors designs offer high luminosity capabilities. Photon beams can be produced with the primary electron beam and we will discuss experiments using both types of beams. The formalism and experimental aspects of lepton scattering off a fixed target are discussed e.g. in [22] or [23].

The beams can be polarized, i.e. the spin of the particles can have a preferred direction. This is important since some observables average out if one uses unpolarized beams. Hence, more information on the nucleon structure and behavior can be obtained from polarized beams. Likewise, if the target is polarized, one has access to additional information. A more complete case is when both target and beam are polarized. Such a “double-polarization” set-up is a requirement for inclusive experiments probing the spin structure of the nucleon, such as the experiment discussed in Chapter 6. Double-polarization is also mandatory if one wants to provide stringent constraints on PWA in a search for new resonances, such as in the experiment discussed in Chapter 3.

1.1.1.1 Inclusive experiments

In inclusive experiments, only the scattered electron is detected. Figure 1.1 shows the Feynman diagram of the inclusive $N(e,e')X$ reaction (where X represents the particles produced in the scattering) in the one-photon exchange leading approximation (Born approximation) [24].

Inclusive experiments have the advantage of being simple and precise. However, they obviously ignore some of the information resulting from the scattering. The halls A and C of Jefferson Lab, with their small-acceptance high-resolution detectors are well suited for such type of experiments.

At fixed beam energy, only two kinematics variables are necessary for character-

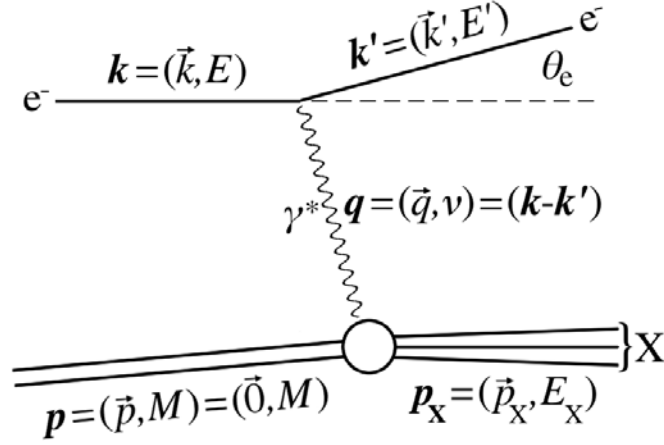


Figure 1.1: First order Feynman diagram for an electron scattering off a nucleon or a nucleus.

izing an inclusive reaction. Otherwise, a third kinematics variable is required. Many kinematics variables exist and some are more relevant than others depending on the context of the study. Relevant kinematics variables for inclusive reactions are:

- The energy transferred from the beam to the target, $\nu = E - E'$, where E is the energy of the incident electron of the beam and E' the one of the scattered electron. In the first Born approximation, ν is the energy of the virtual photon probing the nucleon (or nucleus).
- The angle between the incident and the scattered electrons, θ_e .
- The four-momentum squared exchanged between the beam and target particle, $Q^2 = -\mathbf{q}^2$, with $\mathbf{q} = (\vec{q}, \nu)$. In the one-photon exchange approximation, it is the mass squared of the exchanged virtual photon. For real photons, Q^2 is equal to zero. Q^2 gives the space-time scale at which the nucleon is probed.
- The invariant mass of the recoiling hadronic system, W . It gives the mass of the excited nucleon that was probed. It thus is particularly relevant for experiments investigating the nucleon spectrum or occurring in the resonance domain. $W^2 = (\mathbf{p} + \mathbf{q})^2$, where \mathbf{p} is the four-momentum of the scattering center.

- The Bjorken scaling variable [9], x . In the parton model¹, x gives the fraction of the nucleon momentum carried by the struck quark. Typically, x is about 0.3 or lower for DIS experiments. It is larger in the resonance region and reaches 1 for nucleon elastic scattering. $x = \frac{Q^2}{2pq} = \frac{Q^2}{2M\nu}$, where M is the mass of the scattering center².

In general, the inclusive cross section depends on two independent kinematics variables and four dynamical quantities called “structure functions”. Structure functions encompass the information on the nucleon structure. Since this one is ruled by low-energy QCD, structure functions are non-perturbative quantities. Obtaining the structure functions (or their ratios) is usually the goal of experiments investigating QCD and nucleonic or nuclear structure.

The inclusive inelastic cross section σ , for a beam and target of polarizations P_b and P_t respectively, is given by (e.g. equation in section 2.1.3 in [24]):

$$\begin{aligned} \frac{d^3\sigma}{d\Omega dE'} = \sigma_{Mott} & \left(W_2(Q^2, \nu) \right. \\ & + 2 W_1(Q^2, \nu) \tan^2 \frac{\theta_e}{2} \\ & \pm 2 P_b P_t \tan^2 \frac{\theta_e}{2} (E + E' \cos \theta_e) M G_1(Q^2, \nu) \\ & \mp 2 P_b P_t Q^2 \tan^2 \frac{\theta_e}{2} G_2(Q^2, \nu) \left. \right), \end{aligned} \quad (1.1)$$

where Ω is the solid angle of the scattered electron, W_1 , W_2 , G_1 and G_2 are the structure functions and σ_{Mott} is the cross section for scattering off a point-like target (see equation 1.2). The signs before the third and fourth terms depend on the beam and target polarizations are either parallel or anti-parallel. The structure of this expression makes clear that the structure functions contain the information on the target structure. The Mott cross-section is given by:

$$\sigma_{Mott} = \frac{Z^2 \alpha^2 \cos^2 \frac{\theta_e}{2}}{4E^2 \sin^4 \frac{\theta_e}{2}}, \quad (1.2)$$

¹The parton model is the first approximation of the interpretation of deep inelastic scattering, in which quarks are viewed as point-like free massless objects.

²Proton: $M_p=0.9383$ GeV/c², deuteron: $M_D=1.875$ GeV/c², helium-3: $M_{3He}=2.808$ GeV/c².

where Z is the electric charge of the scattering center and α the fine structure constant.

As it is clear from equation 1.1, experiments that do not have both the target and the beam polarized are only sensitive to the W_1 and W_2 structure functions. Thus, half of the target structure information is missing. This underlines the importance of developing highly polarized beams and targets for complete QCD and nucleon structure experiments.

1.1.1.2 Elastic scattering on nuclei

In the case of elastic scattering, the cross section depends only on two factors containing the structure information. They are called “form factors”. The unpolarized elastic cross-section is given by (equation 2.8 in [24]):

$$\frac{d^2\sigma}{d\Omega} = \sigma_{Mott} \left(\mathbf{W}_2(Q^2) + 2 \mathbf{W}_1(Q^2) \tan^2 \frac{\theta_e}{2} \right), \quad (1.3)$$

where \mathbf{W}_1 and \mathbf{W}_2 are the form factors. Doubly polarized elastic scattering does not bring additional information on the nucleon/nucleus structure compared to unpolarized elastic scattering. However, it is still a very useful reaction to consider since it can be used to obtain more simply and more precisely the form factors by measuring the elastic cross section asymmetry. Asymmetries are relative quantities that are typically more easily and reliably extracted than the cross-sections. The latter are absolute quantities depending on normalization factors sometimes hard to estimate with high accuracy, for example the acceptance of the detector. Conversely, if the form factors are well known, doubly polarized elastic cross sections or asymmetries can be used for beam and target polarimetry, allowing the extraction of the factor $P_b P_t$. We will discuss this technique in Chapter 6.

1.1.1.3 Exclusive (and semi-inclusive) experiments with multi-particle final states

In exclusive experiments, most of the particles produced in the reaction are detected (undetected particles can be determined by other means, such as the missing mass technique). This demands ideally a complete coverage of the solid angle around

the target. Jefferson Lab's Hall B CLAS detector, with its large ($\sim 2\pi$) solid angle coverage is especially designed to study exclusive and semi-inclusive experiments. In semi-inclusive experiments, only part of the reaction product is detected. Exclusive experiments can cleanly isolate the reaction of interest by requesting that all decay products of the nucleon excited state under study are detected or inferred. Hence, this allows to study reactions that otherwise would be hopelessly buried under background, if they were looked at with inclusive experiments. Semi-inclusive reactions can be used to tag a particular process. For instance, one way to investigate the strange quark content of the nucleon would be to request that a meson of strangeness ± 1 (Kaon) is detected in an otherwise DIS kinematics.

The single (beam) longitudinally polarized exclusive cross-section is given by:

$$\begin{aligned} \frac{d^3\sigma}{d\Omega dE'} = \sigma_{Mott} & \left(U_L W_L + U_T W_T^+ + P_b U_T' W_T^- \right. \\ & + U_{TT} (\cos 2\phi W_{TT} + \sin 2\phi \tilde{W}_{TT}) \\ & + U_{TL} (\cos \phi W_{TL} + \sin \phi \tilde{W}_{TL}) \\ & \left. + P_b U_{TL} (\cos \phi W_{TL}^+ + \sin \phi \tilde{W}_{TL}^-) \right), \end{aligned} \quad (1.4)$$

where the U are kinematics factors and the W are various structure functions [25]. ϕ is the angle between the scattering plane and the reaction plane, and P_b is the beam polarization.

The doubly polarized exclusive cross section contains even more structure functions and can be found e.g. in [26], equation (29). This equation and equation 1.4 show the necessity to have both a polarized beam and polarized target, and to be able to cover a large ϕ range to completely separate all the structure functions.

1.1.2 Overview of polarized targets

The main requirements for an efficient polarized target are a high content of polarizable nucleons, a high polarization, a small polarization build up time but slow loss rate of the polarization and the possibility for the target to reverse its polarization direction. Many targets meet those criteria with varying degrees of success. A few of them, used at Jefferson Lab, will be described in this section.

One type of targets relies on Dynamic Nuclear Polarization (DNP). Commonly used materials for DNP-type targets are ammonia [27] (NH_3), butanol ($\text{C}_4\text{H}_9\text{OH}$) and lithium hydride (${}^7\text{LiH}$), as well as their deuterated counterparts (ND_3 , $\text{C}_4\text{D}_9\text{OD}$ and ${}^6\text{LiD}$ [28]). These are solid state targets and can achieve very high polarizations for the hydrogen species within the molecules (80-90% for protons and 40-80% for deuterons), but their polarizations are highly diluted due to the presence of other heavier nuclei, which create undesired background. The polarization builds up, within a few hours, by inducing radio-frequency transitions (see section 1.2.1) between nucleons and electron energy levels. However, those materials are diamagnetic substances (all electrons paired), thus it is necessary to dope the material to introduce free electrons (paramagnetic radicals) into the target material. The doping is made by irradiation for ammonia and lithium hydride targets and by addition of a chemical dopant for butanol targets. In the case of the FROzen Spin Target (FROST) [16] in Hall B, the butanol is mixed by weight with 5% of H_2O and 0.5% of TEMPO³, which is frozen in 1-2 mm beads and placed in a target cup of 50 mm long and 15 mm in diameter. The FROST is a frozen spin mode target operating at 50 mK and 0.56 T and has to be repolarized every few days. This creates, like for DNP-type targets used with high current (50-100 nA), a significant overhead that reduces the overall target efficiency.

Another target commonly used in Jefferson Lab's Hall A is a gaseous helium-3 polarized target. It is a good substitute to a polarized free neutron target, which cannot be realized due to the short lifetime of free neutron (~ 15 minutes) and its neutral charge. Indeed, both proton spins in the ${}^3\text{He}$ nucleus form antiparallel pairs, thus, because the nucleons are predominantly in a S-wave, the spin of the neutron aligns with the one of the ${}^3\text{He}$ nucleus. The advantage of the ${}^3\text{He}$ target over the previous (DNP-type) targets is that the ${}^3\text{He}$ target is almost pure ${}^3\text{He}$. (It only includes a small amount of nitrogen gas of about 1%.) An obvious drawback of this target is its lower density (typically 1% of a solid target) due to its gaseous nature, which is partly compensated by a longer target cell and higher beam current. Fortunately, ${}^3\text{He}$ target can stand several tens of μA beam current, contrarily to the FROST target (which can only be run with photon beam) and DNP-type targets that typically use about 10 nA (although high currents of about 0.1 μA were achieved in Hall C at a price of larger overhead due to the necessary very frequent anneals⁴). The

³TEMPO or (2,2,6,6-tetramethylpiperidin-1-yl)oxidanyl is a heterocyclic chemical compound used as chemical dopant for butanol targets with the formula $(\text{CH}_2)_3(\text{CMe}_2)_2\text{NO}^\bullet$.

⁴An anneal consists to warm up the target to a characteristic temperature, usually around 100 K, which allows to recover most of the target polarization.

target is polarized by optical pumping⁵ (see section 1.2.3). During the experiment described in Chapter 6, the target polarization was about 40%. New techniques of hybrid optical pumping [29] allow now to reach a polarization of about 65%.

Recently, in 2008, the Hydrogen Deuteride (HD) target has been added to the Jefferson Lab polarized targets collection in Hall B. This target is a transfer from Brookhaven National Laboratory, where it was developed. Only a few other HD targets were developed across the world. For instance, in France with the Hydile target [30] at GRAAL, or in Japan with the new HD target [31] at the Super Photon ring-8 GeV facility. The HD target is a solid state target made of 99.9% pure HD molecules (see section 2.1.1), where both proton and deuteron are polarized. It allows to study both nuclei in the exact same experimental configuration with ideally scattering only from nuclei (H and D) of interest. Unlike the DNP-type targets, the HD target is polarized by a “brute force” method. Reaching a long enough polarization lifetime takes 2-3 months. Thus, the target cannot be repolarized. However, the target can also achieve extremely long relaxation times (polarization loss rate), which is usually enough to perform weeks of experiment. Like FROST, the HD target is a frozen spin target operating at 50 mK with the same target cell dimensions (50 mm long and 15 mm in diameter).

The table 1.1 shows a summary of the previously mentioned targets with their “naive” dilution factor⁶, f , and typically achievable target polarization, P_t . The dilution factor is the ratio of scattering events from proton (deuteron, etc) in the target over the total number of events from all nuclei in the target. It denotes the quality of the target (the higher, the better). The dilution factors, for protons (f_H) and deuterons (f_D) respectively, are calculated according to the following formulae:

$$f_H = \frac{n_H \sigma_H}{\sum_A n_A \sigma_A} = \frac{n_H}{\sum_A A n_A} \text{ and} \quad (1.5)$$

$$f_D = \frac{n_D \sigma_D}{\sum_A n_A \sigma_A} = \frac{2n_D}{\sum_A A n_A}, \quad (1.6)$$

where A is the mass number of the nucleus (number of nucleons), n_A the number

⁵Optical pumping is also used with protons, but it is less common and not employed in the Jefferson Lab experimental program.

⁶Those dilution factors are naive, because they do not take into account any peripheric material within the target. The actual dilution factors are usually lower.

CHAPTER 1. THEORETICAL ASPECTS

Proton				
Target	f	P_t	I	B
$^{15}\text{NH}_3$	0.167	75-90%	10-100 nA	5 T
^7LiH	0.125	80%		5 T
$\text{C}_4\text{H}_9\text{OH}$	0.135	85%	only photons ($\sim 10^7/\text{s}$)	0.56 T
HD	0.333	60%	photons: $\sim 10^8/\text{s}$ electrons: 0.1-1 nA	0.1-1 T

Deuteron				
Target	f	P_t	I	B
$^{15}\text{ND}_3$	0.286	25-45%	10-100 nA	5 T
^6LiD	0.25	50-55%		5 T
$\text{C}_4\text{D}_9\text{OD}$	0.238	80%	only photons ($\sim 10^7/\text{s}$)	0.56 T
HD	0.667	15-35%*	photons: $\sim 10^8/\text{s}$ electrons: 0.1-1 nA	0.1-1 T

*15-20% D polarization achieved simultaneously with 60% H. Up to 35% D polarization achieved by moving spin from H.

Helium-3				
Target	f	P_t	I	B
^3He	1	40-80%	10-30 μA	0.005 T

Table 1.1: Summary of the different polarizable targets, their dilution factor f , typically achievable target polarization P_t , typical beam current that can be used I , and in-beam magnetic fields B .

of those nuclei in the molecule and σ_A their cross section with $\sigma_A \sim A\sigma_H \sim \frac{A}{2}\sigma_D$. Dilution, just like polarization, has direct consequences on measurements and their precision, because measured observables, such as an asymmetry, are proportional to the target polarization, but their uncertainty ϵ is also, for most of them, inversely proportional to the square root of measured data number N_{data} , as:

$$\epsilon_{measured} \propto f P_t \epsilon_{target} \propto \frac{1}{\sqrt{N_{data}}}. \quad (1.7)$$

Thus, a factor 2 down on the dilution factor or polarization means a factor 4 up on the amount of data to collect to achieve a comparable uncertainty on the target

observables.

1.2 Polarimetry

1.2.1 Introduction

Polarimetry is the measure of the polarization of a material. Within the context of this thesis, “polarization” implies the spin polarization of electrons or atomic nuclei, also known as magnetization.

Spin is a fundamental property of particles and can be thought of as a magnetic moment vector, which causes the particle to act like a small magnet in the presence of an external magnetic field. It is a purely quantum mechanical quantity without classical equivalent. It naturally appears in the theory describing elementary particles combining quantum mechanics and special relativity. Electrons and many atomic nuclei carry a non-zero spin S in their ground state. Consequently, the particle will be in one of the $2S + 1$ spin states of the ground state.

In the absence of a magnetic field, spin states are degenerated, as they all have the same energy. However, when a magnetic field B is applied to the material, a separation of those spin states at different energy levels can be observed, as shown in figure 1.2. This phenomenon, discovered in 1896 by Pieter Zeeman, is called the Zeeman effect.

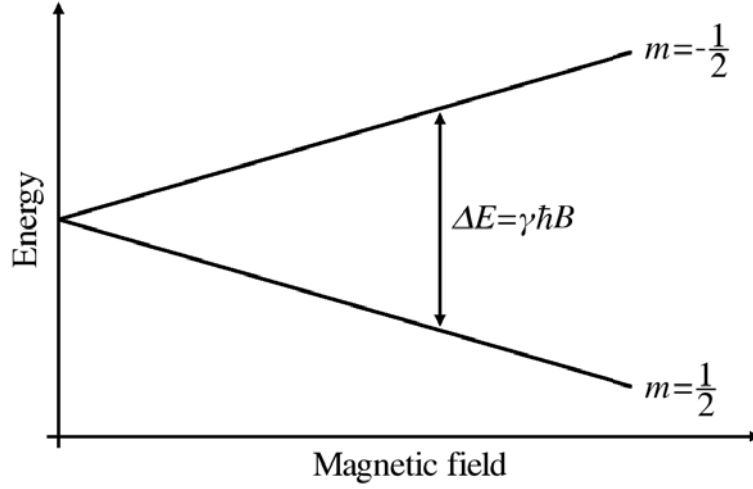
The energy relative to the ground state of the spin state of value m is:

$$E_m = -m\gamma\hbar B, \quad (1.8)$$

where $m = -S, -S + 1, \dots, S - 1, S$, γ is the gyromagnetic ratio of the nucleus or electron⁷, \hbar is the reduced Planck constant and B is the magnitude of the magnetic field applied.

The spin polarization provides information on the occupancy of the different magnetic substates for a large number of nuclei or electrons. It is a unitless quantity

⁷Electron $\gamma_e/(2\pi) = 28.025 \text{ GHz}\cdot\text{T}^{-1}$. Hydrogen $\gamma_H/(2\pi) = 42.58 \text{ MHz}\cdot\text{T}^{-1}$. Deuterium $\gamma_D/(2\pi) = 6.54 \text{ MHz}\cdot\text{T}^{-1}$.


 Figure 1.2: Energy level splitting, for $S=1/2$.

ranging between -1 and 1, and is defined as:

$$P = \frac{1}{S} \sum_{i=-S}^S i \frac{N_i}{N}, \quad (1.9)$$

where N_i is the number of particles in the spin state i and N is the total number of particles in the considered sample, making $\frac{N_i}{N}$ the occupancy ratio of the spin state i .

If all spin states are equally populated, the polarization is zero. In general, a material at temperature T and under a magnetic field B has a (usually small) polarization, called Thermal Equilibrium (TE). At the thermal equilibrium, the spin state population follows the statistical distribution of Boltzmann, which gives the occupancy ratio of the spin state m as:

$$\frac{N_m}{N} = \frac{g_m e^{-\frac{E_m}{kT}}}{\sum_{i=-S}^S g_i e^{-\frac{E_i}{kT}}}, \quad (1.10)$$

where $m = -S, -S+1, \dots, S-1, S$, g_m (g_i) is the degeneracy of spin state m (i), E_m (E_i) is the energy of spin state m (i) given by equation 1.8, k is the Boltzmann constant and T is the sample temperature.

The thermal equilibrium polarization can be deduced from the previous equations 1.8, 1.9 and 1.10:

$$P_{\text{TE}} = \frac{1}{S} \frac{\sum_{i=-S}^S i g_i e^{\frac{i\gamma\hbar B}{kT}}}{\sum_{i=-S}^S g_i e^{\frac{i\gamma\hbar B}{kT}}}. \quad (1.11)$$

For a given material, the thermal equilibrium polarization essentially depends on the magnetic field B and the temperature T of the sample. It will grow as the magnetic field magnitude increases and the temperature decreases.

In the special case of spin $S = 1/2$ (e.g. electron or hydrogen nucleus), equation 1.11 becomes:

$$P_{\text{TE}} = \frac{1 - e^{-\frac{\gamma\hbar B}{kT}}}{1 + e^{-\frac{\gamma\hbar B}{kT}}} = \tanh\left(\frac{\gamma\hbar B}{2kT}\right), \quad (1.12)$$

and in the case of spin $S = 1$ (e.g. deuterium), it becomes:

$$P_{\text{TE}} = \frac{1 - e^{-\frac{2\gamma\hbar B}{kT}}}{1 + e^{-\frac{\gamma\hbar B}{kT}} + e^{-\frac{2\gamma\hbar B}{kT}}} = \frac{4 \tanh\left(\frac{\gamma\hbar B}{2kT}\right)}{3 + \tanh^2\left(\frac{\gamma\hbar B}{2kT}\right)}, \quad (1.13)$$

The dependency of the thermal equilibrium polarizations of hydrogen and deuterium with the ratio of the magnetic field over the temperature (B/T) is shown in figure 1.3, and a couple of those polarizations are given for different ratios in table 1.2.

1.2.2 Nuclear Magnetic Resonance polarimetry

The polarization of nuclei can be measured by using the Nuclear Magnetic Resonance (NMR) phenomenon.

1.2.2.1 Principle

This phenomenon is observed when the energy levels of nuclei are split with a magnetic field of magnitude B , as described in the previous section 1.2.1, and

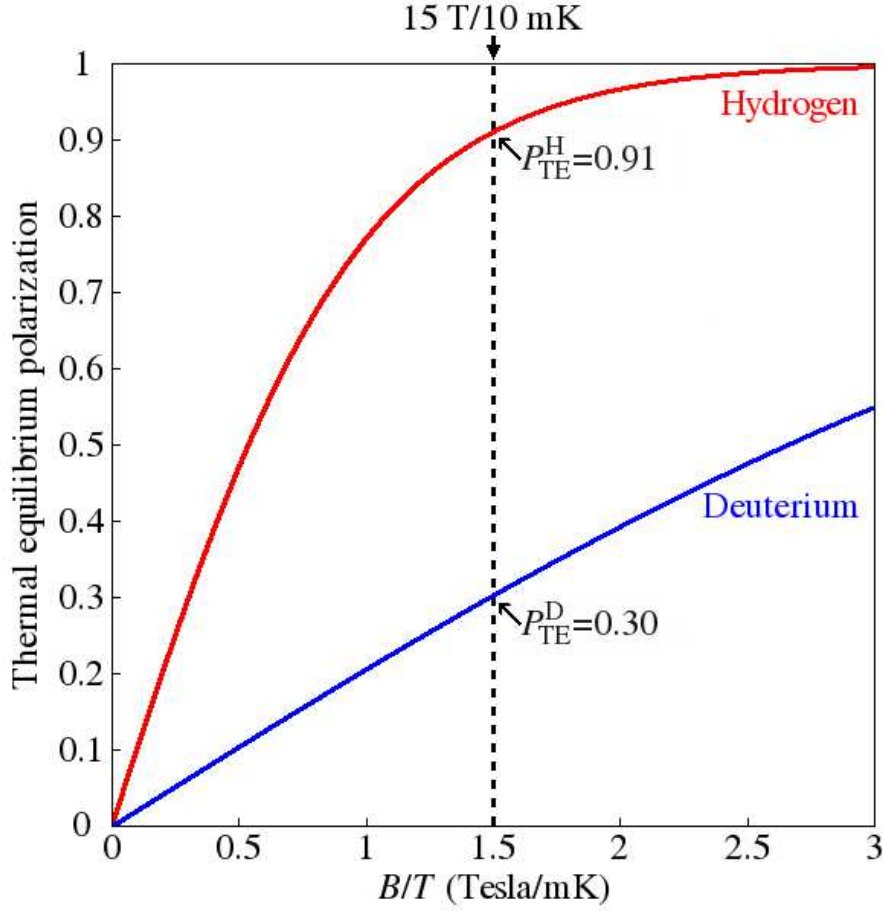


Figure 1.3: Thermal equilibrium polarizations of hydrogen and deuterium versus magnetic field over temperature ratio (B/T).

transitions are induced between those levels with a Radio Frequency (RF) magnetic field emitted at a specific frequency by a transmitter coil. Then, the observation of the resonance by a receiver coil allows to deduce the polarization.

The frequency ν of the RF field is chosen according to the magnetic field magnitude. Indeed, the resonance condition occurs when the energy of the photons (equation 1.14) associated with the RF field matches the energy gap between the split levels (equation 1.15). This frequency is known as resonance frequency or Larmor frequency, and can be deduced from the equations:

$$E_{\text{photon}} = h\nu; \quad (1.14)$$

B/T (T/mK)	P_{TE}^H	P_{TE}^D
0.01	0.01	0.002
0.1	0.102	0.021
0.5	0.471	0.104
1	0.771	0.206
1.5	0.911	0.303
2	0.967	0.393
2.5	0.988	0.476
3	0.996	0.55

Table 1.2: Calculated thermal equilibrium polarizations of hydrogen and deuterium at different magnetic field over temperature ratio (B/T).

$$\Delta E = E_{m+1} - E_m = \gamma \hbar B; \quad (1.15)$$

as

$$\nu_{Larmor} = \frac{\gamma B}{2\pi}. \quad (1.16)$$

In fact, even away from the resonance condition, transitions induced by the RF field can still happen, but are very unlikely and will considerably increase when the resonance condition is met. The probability of transitions is close to a Dirac delta distribution centered on the Larmor frequency. Those transitions are either absorption or stimulated emission, which have equal probability to occur. The absorption will make the nucleus to move to a more energetic spin state, while the stimulated emission will move it to a less energetic one (see figure 1.4). Those transitions then induce an RF field proportional to the polarization, which induces a signal in the receiver coil.

1.2.2.2 Adiabatic fast passage

The Adiabatic Fast Passage (AFP) is a commonly known technique used to reverse the polarization of nuclei by setting a condition on the sweep rate. The sweep must be slow enough so that every nuclear spin can follow the sweeping magnetic field and pass through the resonance condition. However, it must be fast enough to pass quickly by the resonance condition in order to avoid polarization losses since each

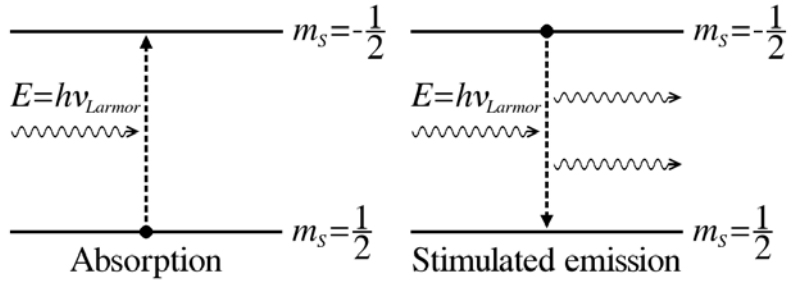


Figure 1.4: Radio frequency transitions in a nucleus of spin $S=1/2$.

RF induced transition is a loss of polarization. For a field sweep (see section 4.1.3.1), the AFP condition in solids is:

$$\left| \frac{B_{RF}}{T_1} \right| \ll \left| \frac{dB}{dt} \right| \ll |\gamma B_{RF}^2|, \quad (1.17)$$

where B_{RF} is the magnitude of the RF field, T_1 is the relaxation time of the material (see section 2.1.3.1) and dB/dt is the sweep rate of the main magnetic field.

Ideally, the spin populations are reversed by inducing a single transition on every nucleus in the sample with no polarization loss. In certain cases, such as the HD target, the RF transitions are not completely efficient and the RF power required for the AFP might be too large or might heat up the target, which may cause polarization losses. Thus, NMR measurements are usually performed with a power of e.g. 10^{-5} lower, which only induces transitions in a fraction ($\sim 10^{-5}$) of nuclei and leads to very little polarization loss, of the order of a hundredth of a percent.

1.2.3 Electron paramagnetic resonance

The polarization of nuclei can also be measured by using a phenomenon analogous to the NMR one, the Electron Paramagnetic Resonance (EPR) phenomenon. Its principle is similar to the one of NMR, but focuses on the resonance of the unpaired electrons of atoms.

An application of the EPR is the measure of the polarization of the helium-3 (^3He) targets [32] by using the rubidium (Rb) level splitting. (Rubidium is used to polarize the helium-3 by optical pumping.)

The electron energy levels of the rubidium are split by the Zeeman effect with a magnetic field B_0 . The difference between those levels is given by the EPR frequency ν_{EPR} (Larmor frequency of the electrons), which is proportional to the effective magnetic field B as:

$$\nu_{EPR} = \frac{\gamma_e}{2\pi} B, \quad (1.18)$$

and B is:

$$B = B_0 + \delta B, \quad (1.19)$$

where δB is the additional magnetic field (~ 100 mG) created by the presence of the polarized helium-3, which is proportional to the polarization of the helium-3 nuclei.

Consequently, the resonance frequency is shifted by a value, $\delta\nu_{EPR}$, also proportional to this polarization, as:

$$\nu_{EPR} = \nu_0 \pm \delta\nu_{EPR}, \quad (1.20)$$

where ν_0 is the resonance frequency in absence of polarized helium-3, proportional to the holding field B_0 (equation 1.18). The sign in the equation depends on the anti-parallel (+) or parallel (-) polarization with respect to the holding field. Thus, measuring the difference between the frequency in anti-parallel and parallel cases gives a precise measurement of the helium-3 polarization.

1.2.4 Polarimetry using electron scattering asymmetry

The polarization can also be determined from measurements of a well-known electron scattering reaction, such as elastic scattering off nuclei. In this case, experimental asymmetries A_{exp} can be computed by simulation (see section 1.1.1.2), while raw asymmetries A_{raw} can be obtained from physical data. This method will be described in detail in Chapter 6, where polarimetry using elastic electron scattering off a polarized ^3He target is discussed.

The relation between the experimental and raw asymmetries is, in the absence of background (polarized or unpolarized) :

$$A_{exp} \propto \frac{A_{raw}}{P_b P_t}. \quad (1.21)$$

The beam polarization P_b can be measured with a polarimeter, such as Møller polarimeter or Compton polarimeter (see section 3.2.1). Thus, P_t can be obtained.

Chapter 2

HDice target

2.1 Target cell and HD material

2.1.1 Description

The HDice target is a Hydrogen Deuteride (HD) polarized target. It is mostly made of HD molecules in the solid state including a few H_2 and D_2 impurities. The presence of those impurities is essential for polarizing the target, as it will be explained later in section 2.1.3. The polarization of the target is achieved at very low temperature (~ 10 mK) with a strong magnetic field (~ 15 T), as described in section 2.3.5.

The HDice target offers many interesting features for the study of nucleons (protons and quasi-free neutrons). First, the target ideally contains only protons and deuterons, which can both be polarized, in principle up to 90 % for H and 30 % for D with the current setup at Jefferson Lab. As already explained in Chapter 1.1.2, other types of targets contain additional nuclei that are unpolarized and unwanted. For instance, ammonia targets (NH_3 and ND_3) contain nitrogen creating undesirable background. Therefore, with an HD target we largely minimize such unwanted background. Another advantage of an HD target is that it can hold its polarization for a long time in “frozen-spin mode”, several months to years in the experimental

conditions (<500 mK and ~ 1 T).

However, the counterpart of those benefits is that the target handling procedures are complex and the polarization is impossible to recover when lost. A polarized HDice target in frozen spin mode requires at least three months to mature to its optimal properties (high polarization and long polarization relaxation time) and does not forgive any mistake. A rise in temperature or a drop of the magnetic field can lead to unrecoverable loss in polarization. Consequently, the monitoring of the target parameters (temperature, magnetic field) is needed at all time, excepted in a few dewars, where permanent magnets are installed.

2.1.2 Target cell design

The target cell consists of an outer shell and an inner shell, aluminum wires and a copper ring, see figure 2.1.

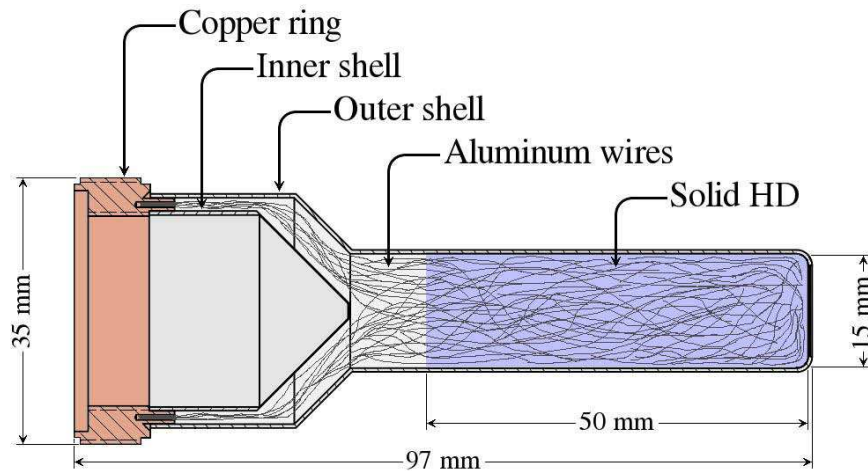


Figure 2.1: HDice target cell schematic.

The shells are made of a fluoropolymer, PCTFE (PolyChloroTriFluoroEthylene) Kel-F, that offers interesting features even at extremely low temperatures (~ 10 mK); low permeation, low deformation, and good mechanical, chemical and radiation

resistance. The shells also do not contain any hydrogen or deuterium atoms. Thus, there is no background to the H or D signals measured with NMR, while the NMR signal on Fluorine, which is at about 5% higher field than H at the same frequency, provides a reliable magnetic field calibration. The shells are glued on the copper ring and the cylindrical side of the outer shell is filled with solid HD, that takes the form of a 50 mm long and 15 mm diameter cylinder.

The HDice target cell contains 750 intertwined aluminum wires (50 μm diameter and 99.9998% purity). They conduct out of the HD the heat generated in the polarization process, as well as heat produced by beam interaction or energy level transitions. As part of the wires are in the beam path, because of its good thermal conductivity, low density and low nucleons count, aluminum is a good choice to limit background interactions with the beam. The wires are packed and soldered to 60 holes in the ring.

The copper ring ensures the support of the target and efficiently dissipates the heat brought by the aluminum wires into the dewar. As the ring is not in the way of the beam or in the sight of a detector, copper with its superior heat transfer can be used. The ring has a right-handed outside thread, which allows to mount the target on the cold-finger (see section 2.2.1), and a left-handed inside thread, which allows the installation and the removal of the target by the transfer cryostat (see section 2.2.3).

2.1.3 HD material

2.1.3.1 Relaxation

One of the most important parameters of the HD material is its spin-lattice relaxation time T_1 . T_1 is the recovery time of the polarization to the thermal equilibrium (section 1.2.1) via :

$$P(t) = P_{TE} + (P_0 - P_{TE}) e^{-t/T_1}, \quad (2.1)$$

where $P(t)$ is the polarization at the time t , P_0 is the initial polarization at $t = 0$ and P_{TE} is the polarization at thermal equilibrium.

In the case of pure HD, the relaxation times T_1^H for H and T_1^D for D are very long

(greater than several years). Although a long relaxation time is a great advantage to hold the polarization for the duration of an experiment, it also is a problem: Using the polarizing method described in section 2.3.5, it would take decades to reach the desired polarization.

However, in 1967, A. Honig [33] suggested that the relaxation times could be adjusted by adding a small fraction ($\sim 10^{-4}$) of ortho- H_2 and para- D_2 impurities to the pure HD. Indeed, HD protons and ortho- H_2 nuclei have comparable Larmor frequency values that allow them to exchange energy by cross relaxation (figure 2.2). The same phenomenon is observed between HD deuterons and para- D_2 nuclei.

Because of this cross relaxation process and the short relaxation times of ortho- H_2 and para- D_2 (a few seconds), the relaxation times T_1^H and T_1^D of the HD mixture strongly depend on the concentrations of ortho- H_2 and para- D_2 respectively. For an HD target, the lower is the impurity concentration, the longer is the relaxation time.

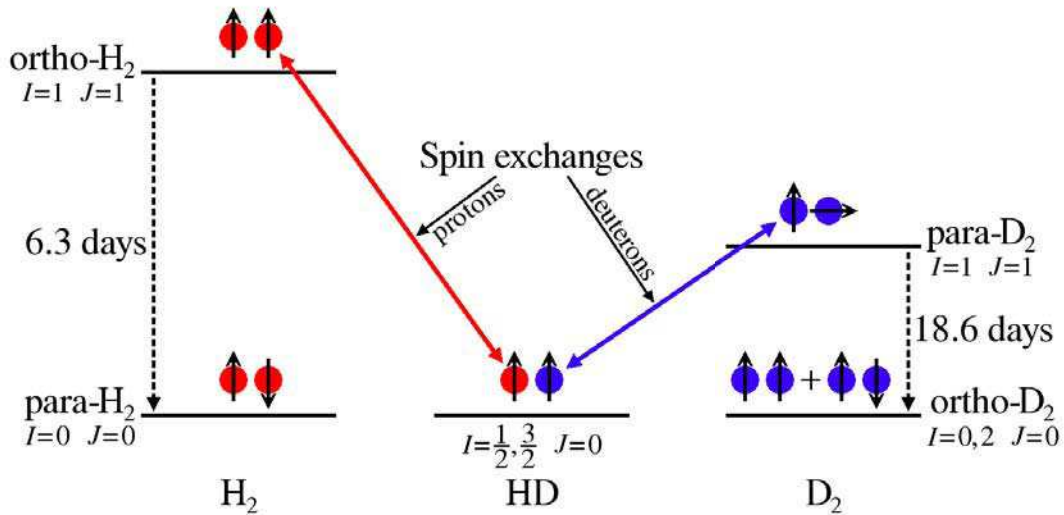


Figure 2.2: Spin exchanges between ortho- H_2 (and para- D_2) and H (and D) nuclei in the HD molecule. The amounts of ortho- H_2 (initially 75% of the H_2 content) and para- D_2 (initially 33% of the D_2 content) decay with a lifetime of 6.3 and 18.6 days respectively.

Ortho- H_2 ($J = 1$) and para- D_2 ($J = 1$) are the names of rotational states J of

H₂ and D₂ with para-H₂ ($J = 0$) and ortho-D₂ ($J = 0$). Ortho refers to the group of states of higher nuclear spin degeneracy and para refers to the lower one, see e.g. [34]. At room temperature, ortho-H₂ amounts to 75% of the H₂ content and para-D₂ to 33% of the D₂ content. Following the Fermi-Dirac distribution for H and Bose-Einstein distribution for D, the populations of ortho-H₂ and para-D₂ decay at liquid helium temperature with a lifetime of 6.3 days and 18.6 days respectively (figure 2.2). Consequently, the HD relaxation times T_1^H and T_1^D depend on time and will increase as the concentrations of ortho-H₂ and para-D₂ decrease.

Therefore, we can have short relaxation times during the polarization phase and, once the HD is polarized, still achieve long relaxation times by waiting at low temperature.

In practice, impurities do not need to be added because commercial HD gas already contains about 1.5% of H₂ and 0.5% of D₂, which are two orders of magnitude too high for the HD target. Thus, the HD gas must be first purified to the desired level of 10^{-4} .

2.1.3.2 Gas purification

The purification is done by distillation [35][36] and enables the extraction of H₂ and D₂ from the HD mixture because the vapor pressures of H₂, D₂ and HD differ at low temperature.

The purification is performed in a column distiller operating at a temperature of 20 K. The lightest molecules move to the upper part of the column, while the heaviest ones drop to the lower part. Once the separation is established, we can distinguish three different gases that can be extracted and stored in individual tanks; an H₂ enriched HD gas, a purified HD gas and a D₂ enriched HD gas.

Each distillation cycle roughly reduces the concentration of impurities in the HD mixture by one order of magnitude. A double distillation process is often needed in order to reach the required purity for the HD target.

2.1.3.3 Gas characterization

Knowing the evolution of the relaxation times of the HD gas as a function of the impurities is essential, because it helps to have a better control on the target polarization process.

Two complementary approaches can help characterizing the purified HD gas. The first approach is to observe the time-evolution of the relaxation times T_1 by making T_1 measurements periodically at given temperatures, usually 2 K and 4 K. These T_1 measurements will be described later in section 4.2. Then, an estimation of the evolution at very low temperature can be made. However, this method is very time consuming and can take months to study a single gas.

The second approach is to directly measure the impurity concentrations and to predict the evolution of the relaxation times theoretically. To measure those concentrations, one can use a Residual Gas Analyzer (RGA), gas chromatography or Raman spectroscopy. However, due to the low impurity concentrations in the purified HD gas, $\sim 10^{-4}$, the Raman spectroscopy is the most adapted. Indeed, the RGA and the gas chromatography only have a sensitivity of 10^{-2} and 10^{-3} respectively, while the Raman spectroscopy set-up used by the HD collaboration has a sensitivity of 10^{-4} and potentially 10^{-5} with a few improvements.

Raman spectroscopy, named after C. V. Raman, is used to observe rotational modes in the HD gas. It induces transitions with a laser between rotational states J such that $\Delta J = \pm 2$. Para- H_2 or ortho- D_2 : J even, $(J = 2n) \leftrightarrow (J = 2n + 2)$. Ortho- H_2 or para- D_2 : J odd, $(J = 2n + 1) \leftrightarrow (J = 2n + 3)$.

As the transitions only occur between para states or between ortho states, the measured intensities for each transition allow to evaluate the ortho and para concentrations of the HD gas [37].

2.2 Cryostats

The following sections will detail all the cryogenic devices used to operate the HDice target:

- The Production Dewar: a cryostat used for target fabrication and polarimetry with a temperature of 4.2 K (possibly down to ~ 2 K) and a magnetic field up to 3 T.
- The Transfer Cryostat: a cryostat used to transfer targets between cryostats with a temperature of 2 K and a magnetic field of 0.1 T.
- The Dilution Fridge: a cryostat used to polarize targets with a temperature of 10 mK and a magnetic field of 15 T.
- The Storage Dewar: a cryostat used to store and transport targets with a temperature of 4.2 K (possibly down to 1.6 K) and a magnetic field of ~ 6 T.
- The In-Beam Cryostat: a cryostat used to operate the target under a particle beam with a temperature range of 50 mK to 300 mK, a longitudinal magnetic field up to 0.9 T and a transverse magnetic field up to 0.07 T.

2.2.1 General description

All the cryostats used for the HDice target, except the transfer cryostat, consist of a “cold finger”, a cooling system, a superconducting magnet, a transfer coil (excluding the storage dewar) and a liquid nitrogen shield (excluding the in-beam cryostat). The following does not apply to the transfer cryostat. It will be described in section 2.2.3.

The cold finger allows a direct access to the cell. It contains a M35x1 copper right-handed threaded pedestal or target holder into which the cell is screwed. The cooling system cools down the cold finger, thus the cell, and will be described later for each cryostat. The liquid nitrogen shield is a liquid nitrogen volume which purpose is to reduce the consumption of the liquid helium used by the cooling system.

The superconducting magnet provides the magnetic field to build or to preserve the target polarization. It is often located in a helium bath and has to remain immersed in liquid helium to prevent any magnet “quench”. A magnet quench occurs when the magnet enters the resistive state and starts to heat up. Due to the high energy stored in the magnet (equation 2.2), it can cause an extremely fast

chain reaction, which can lead to the evaporation of a large volume of helium that is dangerous to personal, and can severely damage the magnet. The stored energy in the magnet is :

$$E = \frac{1}{2}L.I^2, \quad (2.2)$$

where L is the inductance of the magnet and I is the current, up to 100 A.

The superconducting magnet can be equipped with a “persistent current switch” between the two ends of the coil that allows the magnet to change between “normal” and “persistent” mode. In normal mode, the switch is heated to be in the resistive state and the current in the coil is set by a high current power supply (120 A, 10 V). Once the desired magnetic field is reached, the magnet can be placed in persistent mode by stopping the heating of the switch. In persistent mode, the switch becomes superconducting and the current of the magnet is trapped in a superconducting loop that preserves the magnetic field without any power requirement. The power supply can then be ramped down to zero and turned off, making the magnet safe from power outage.

Usually off, the transfer coil is powered during target transfer. It ensures that the target cell always stays under a minimum field to preserve the polarization at any moment. It is a simple superconducting solenoid coil spanning the whole length of the cold finger.

2.2.2 Production dewar

The Production Dewar (PD) is designed for target cell fabrication, polarimetry and cell studies.

The PD is the alpha and the omega of HDice targets. Usually, every cell starts and ends its life cycle in the PD. The PD is also used for polarimetry, such as cell calibration, as well as many cell characterizations, T_1 measurements for instance.

The cell is mounted in a copper pedestal in the cold finger of the PD, which also contains a pair of radio frequency coils used for polarimetry. The cooling of the cell is provided by the liquid helium in the “VariTemp” space (see figure 2.3). The VariTemp space is a pumpable volume fed by the helium bath through a needle valve.

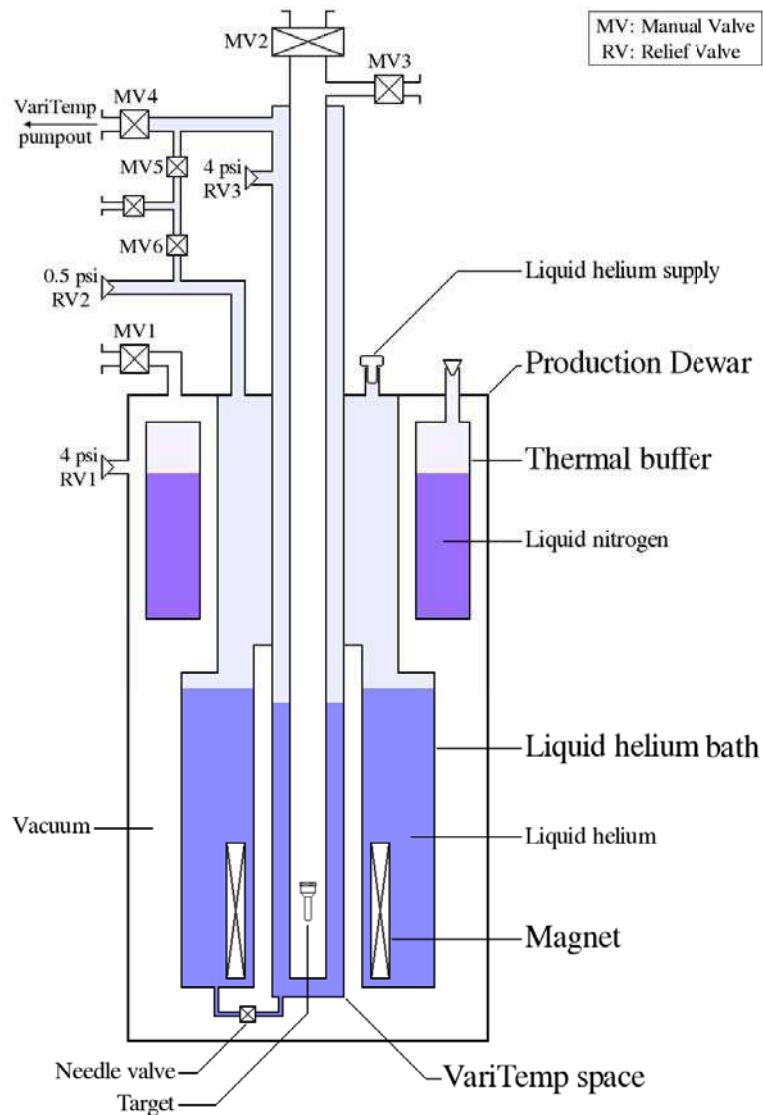


Figure 2.3: Schematic of the Production Dewar.

The usual temperature of the cell in the PD is about 4 K, but it can be lowered below 2 K by pumping on the surface of the helium in the VariTemp space. The helium level in the VariTemp space is then kept stable by adjusting the incoming flow of liquid helium controlled by the needle valve. Since the needle valve is a manual valve, it requires the presence of a person to monitor and to manually adjust it.

The cryogenic filling of the PD has to be done at least once a day for both liquid nitrogen and liquid helium. This may be repeated depending on the cryogenic consumption.

The magnetic field, up to 3 T, is provided by a superconducting magnet.

2.2.3 Transfer cryostat

The Transfer Cryostat (TC) [38] can be viewed as a 3 meter long screwdriver cooled down to 2 K and used to transfer target cells between two cryostats.

The TC consists of a long liquid helium tube that can be pumped and cooled down to 2 K. The tube allows to access the cell in the other cryostats with the left-handed threaded “coldhead” on its end. The coldhead is a threaded piece of copper that is screwed into the inner thread of the target cell ring. The tube is surrounded by a liquid nitrogen filled tube with a radiation shutter to reduce the liquid helium consumption.

When the cell is in the TC, the magnetic field is provided by a Halbach cylinder¹ [39] producing a permanent transverse magnetic field of 0.1 T. The transverse direction of the magnetic field allows to extract and to insert the cell regardless the orientation of the longitudinal magnetic field of the cryostat. Indeed, if the TC had instead a longitudinal magnetic field, the orientation of all magnetic fields should match or a zero field region would exist on the path of the cell transfer. Thus, a transverse magnet avoids such magnetic field cancellation with a longitudinal magnet. However, because of the relatively low magnetic field and the relatively high temperature, the cell cannot remain in the TC for too long as the relaxation time decreases considerably in these conditions. The cell typically stays 40 to 60 minutes in the TC during a standard transfer operation.

¹A Halbach cylinder is a ferromagnetic cylinder made of rare-earth permanent magnets, that can ideally produce a strong magnetic field in its center. It can be magnetized in various patterns (dipole, quadrupole, etc).

2.2.4 Dilution fridge

The Dilution Fridge (DF) is designed to polarize up to 3 target cells at the same time (section 2.3.5).

The DF is remotely controlled by a computer and only requires one cryogenic filling per day. The magnetic field is provided by a superconducting magnet of 15 T when it is cooled down at 4.2 K and up to 17 T at 2.2 K. Unfortunately, no monitoring of the polarization is currently possible during the polarization process.

The cooling of the DF [40], down to 10 mK, is provided by a mixture of ^3He and ^4He (see figure 2.4). The mixture undergoes spontaneous phase separation below 870 mK to form a concentrated phase (almost 100% ^3He) and a dilute phase (about 6.6% ^3He and 93.4% ^4He), which is an endothermic process and is the effective cooling mechanism of the system.

The mixture is stored in gaseous phase in a gas tank. It is first purified by the liquid nitrogen trap, precooled and liquefied by the “1K-pot”, also known as a condenser. The 1K-pot is a pumped liquid helium volume working in the same way as the VariTemp space of the PD. The flow of liquid helium from the bath is automatically adjusted by a needle valve to keep a temperature of about 1.3 K.

Then, the mixture, now liquid, is cooled down by the still and two sets of counter-flow heat exchangers (continuous spiral tube-in-tube² and discrete disks). Thereafter, the mixture enters the mixing chamber, where the phase boundary is. The pure ^3He dissolves into the diluted phase, the ^3He molecules cool as they expand freely into the super fluid ^4He . This processus allows to cool down the mixing chamber and the target cells, which are thermally connected with copper parts. The ^3He is then contiguously distilled out at the still and eventually moves back to the condensing side to rejoin the process. On its way out, to increase the efficiency of the system, the cold mixture cools down the incoming mixture going through the heat exchanger and the still.

²In the tube-in-tube heat exchanger set, the tube transporting the mixture to the mixing chamber is inside the tube transporting it out, which cools down the incoming mixture.

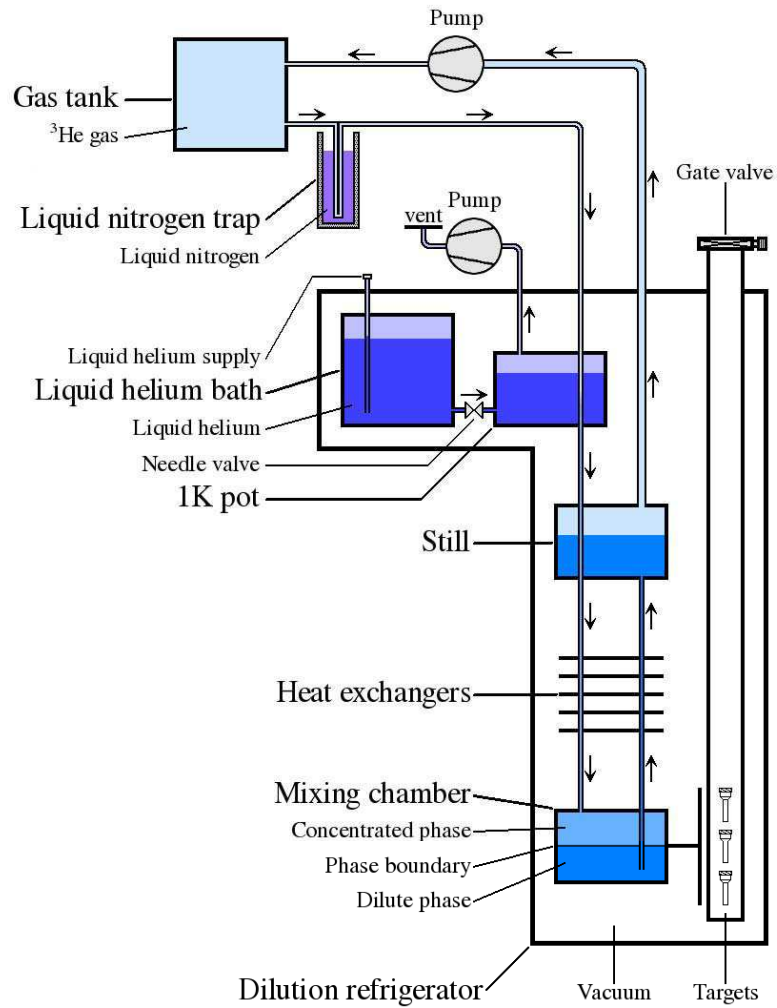


Figure 2.4: Flow schematic of the dilution refrigerator.

2.2.5 Storage dewar

The Storage Dewar (SD) is designed for the storage and the transport of three target cells once they have reach their frozen spin state. It can then free the DF and allow another batch of 3 cells to be produced.

The design of the SD is very similar to the PD. Like the PD, the cells can be

cooled down to 1.6 K by pumping a VariTemp space, but it does not usually need any manual adjustment as it is controlled by computer. The SD also has an enhanced cryogenic capacity and only requires to be filled every two days. Its holding field (~ 6 T) is stronger than the PD and covers a larger region, which nullifies the use of a transfer coil.

2.2.6 In-beam cryostat

The In-Beam Cryostat (IBC) is a dilution refrigerator designed to operate under a particle beam.

As the IBC is designed to operate under beam, the amount of material around the target cell has been minimized to reduce the energy loss of the particles coming in and out of the cell. This is to improve the accuracy of the nuclear physics measurements. For instance, every wall is made of thin aluminum of the order of a millimeter [41] and the two superconducting magnets have a limited number of layers of superconducting wire, which limits their magnetic field magnitudes.

The IBC is also designed to rotate in order to work in two different orientations (see figure 2.5). The vertical orientation allows the transfer of the target cell into the IBC, while the horizontal one is to align the target cell with the beam to conduct nuclear experiments.

The IBC has a similar cooling system as the DF (the IBC is indeed a dilution fridge). It can achieve temperatures down to 50 mK and generate high cooling power (maintaining ~ 200 mK under electron beam configuration). The IBC is also remotely controlled by computer and the cryogenic filling is done automatically.

The IBC has two superconducting magnets, a solenoid that creates a longitudinal magnetic field of 0.9 T and a “saddle coil” that creates a transverse magnetic field of 0.07 T. The saddle coil allows the rotation of the longitudinal magnetic field which allows to flip the polarity without creating a zero field period during the process and losing the polarization of the cell. Unfortunately, because the stored energy for those magnets is too small, a persistent current switch will not work. Thus, to preserve the polarization in case of a magnet quench, a non-superconducting coil is needed as back-up. Therefore, a “back-up coil” of 0.01 T, cooled down with water, is wound

on the outside of the cryostat.

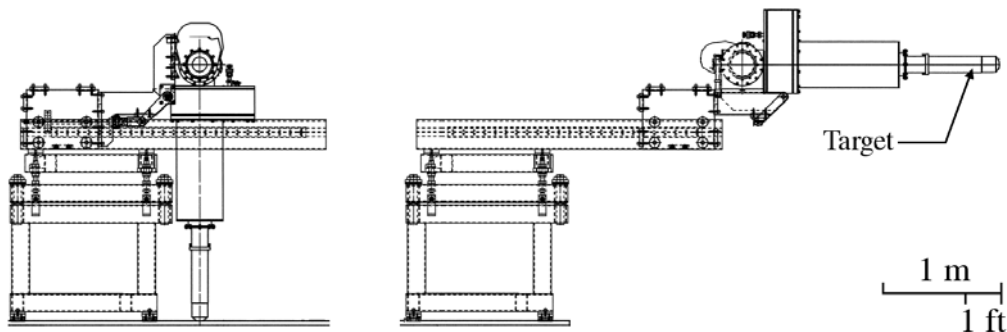


Figure 2.5: Schematic of the In-Beam Cryostat in transfer configuration (vertical orientation on the left) and in experimental configuration (horizontal orientation on the right).

2.3 Target life

2.3.1 Overview

The typical steps of an HDice target's life (see figure 2.6) are listed below:

- Condensation in PD (section 2.3.2);
- Calibration at thermal equilibrium (section 2.3.3);
- Transfer to DF (section 2.3.4);
- Polarizing and aging in DF for about 3 months (section 2.3.5);
- Transfer to PD;
- Check of the polarization (section 2.3.6);
- Possibly, transfer to SD for storage or transport;

- Transport of PD or SD to hall alongside with the TC (section 2.3.7);
- Transfer to IBC;
- Measure of the initial polarization in IBC and possible spin operations between \vec{H} and \vec{D} ;
- Experiment and monitoring of the polarization (section 3);
- Transfer to PD;
- Final polarization measurement (section 2.3.8);
- Evaporation and storage of the collected HD gas (section 2.3.9).

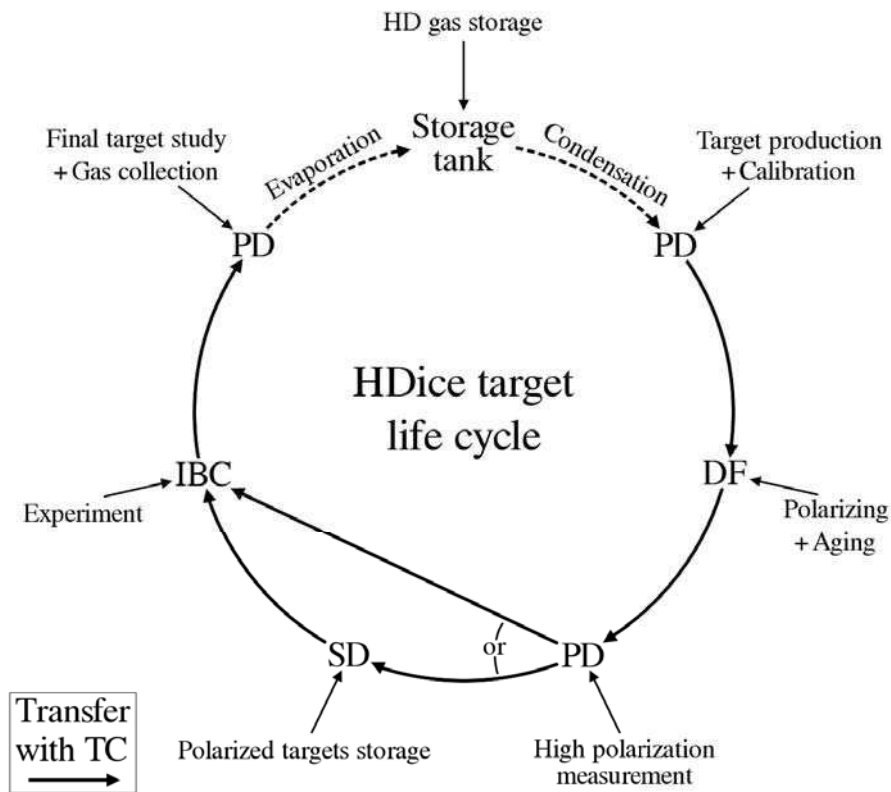


Figure 2.6: HDice target life cycle

As HD gas is difficult to make, it is reused and undergoes those steps as long as its H₂ and D₂ concentrations are acceptable. Those concentrations can change over time due to the HD recombining into H₂ and D₂ ($2 \text{ HD} \rightarrow \text{H}_2 + \text{D}_2$). The recombination may be accelerated due to the irradiation of the HD or the presence of chemical compound acting as a catalyst.

2.3.2 Condensing the target

As stated earlier, HDice targets are produced in the PD by condensing HD gas in the target cell.

The HD gas (~ 0.45 mole) is condensed in the cell through an injection tube glued to cell the day before and installed on top of the PD. The target cell is evacuated for cleaning and leak-checking. The cell is then slowly cooled down by lowering the tube in the PD. As the tube is lowered, the HD gas becomes liquid, then solid. The procedure has to be slow to avoid holes in the HD material or a half filled cell.

When the cell reaches the bottom of the PD, it is screwed in the pedestal of the PD until the glue seal is broken. Finally, the injection tube is removed and the cell is torqued³ to about 140 inch-pounds ($\sim 16 \text{ N.m}$). Torquing the cell is important for the transfer of the cell, as it will be explained in section 2.3.4.

2.3.3 Thermal equilibrium calibration

The polarization is proportional to the area of the signal of a NMR measurement (section 4.1).

$$\textit{Polarization} = C * \textit{Area}. \tag{2.3}$$

The calibration consists of determining the constant C of the target cell, which can be found by knowing the expected polarization and by measuring the area of the signal at thermal equilibrium. Because every cell is different (different amounts of HD and of aluminum wires), it has to be done individually for all the cells.

³Torque is the resultant moment of a Couple. It is used to measure how much tightening tension is applied to a nut or bolt with a torque wrench.

The calibration is done at thermal equilibrium, because this is the predictable known polarization (section 1.2.1). The thermal equilibrium polarization is reached within a few relaxation times of the target. Typically, the relaxation time before aging is of the order of seconds for H and minutes for D.

To reduce the uncertainty on the calibration constant, multiple NMR measurements are made. Indeed, if the noise is Gaussian, as the number of measurements n increases, the Signal-to-Noise Ratio (SNR) increases :

$$\text{SNR} \propto \sqrt{n}. \quad (2.4)$$

To achieve a good precision of the calibration, a full day is required (typically with ~ 400 measurements for H and ~ 200 for D), because the thermal equilibrium signal is small; of the order of 0.01% for H in typical PD condition. The D thermal equilibrium signal is smaller and would require in principle more measurements, but the H signal can be used to calibrate D, since the ratio between the H and D signals is known. We typically measure the D signal only as a consistency check and do only 200 measurements because of lack of time.

2.3.4 Transfer between dewars

The transfer of the target cell from one cryostat to another is the most critical time in the life of an HD target. Indeed, any issue during the transfer can lead to the unrecoverable loss of polarization or the loss of HD material in the cell. The transfer is a long process (~ 10 hours) that is mostly preparation. The actual transfer takes a few hours. The transfer consists of extracting the cell from a cryostat and inserting it into another cryostat.

The extraction of the cell starts by connecting the TC to the cryostat. The TC tube is lowered until it reaches the cell. Thereafter, the tube is rotated “counter-clockwise” to screw the TC coldhead into the cell ring and, then, to unscrew the cell from the cryostat. The rotation of the tube has to be done carefully, because of the friction when screwing and unscrewing the cell that can quickly heat up the cell. When the cell has been unscrewed, it can be lift up in the TC with the other cryostat’s transfer magnet powered to ensure a magnetic field at any time.

Once the cell is in the TC, it has to be transferred to the next cryostat as fast as

possible. Indeed, the TC is an inadequate place for the cell, because the cryogenic supply of the TC is limited and because the rate of polarization loss is higher as the magnetic field is low.

The TC is connected to the other cryostat and the cell is lowered to the bottom of the cryostat with its transfer magnet powered. Thereafter, the tube is carefully rotated clockwise to screw the cell into the cryostat and to unscrew the TC coldhead from the cell ring until it is released. Finally, the tube is lift up and the TC disconnected.

Due to the friction while screwing or unscrewing, the torque (see section 2.3.2) of the cell is reduced at each transfer. Thus, to avoid the release of the cell mid-way, the initial torque of the cell has to be enough. In addition, the cell could become very hard to retrieve and could evaporate if thermal conduction between the cell and the cryostat is not assured.

2.3.5 Polarizing and aging

The target cells are polarized, using the “brute force” method, by applying a high magnetic field at a low temperature and then waiting until the polarization reaches its thermal equilibrium. In the meantime, the target is aging, which means the relaxation time of the cell is increasing exponentially.

The polarizing process starts as soon as three cells have been transferred to the DF and is initiated by setting the magnetic field to 15 T and by lowering the temperature down to 10 mK. Stabilizing the temperature down to 10 mK takes several days, because of the energy released while the HD polarizes and the $J=1$ H₂ and D₂ species decay to their $J=0$ ground states (see figure 2.2), releasing heat. Thus, the optimal thermal equilibrium polarization condition cannot be achieved immediately. Indeed, as long as heat is produced, the thermal equilibrium polarization is lower than it would be in the optimal 10 mK and 15 T condition.

Furthermore, polarizing is more efficient when the relaxation time is short; the longer the relaxation time, the longer it takes to reach thermal equilibrium. Thus, since the relaxation time starts to increase as soon as the HD is condensed, all cells must be transferred quickly. Usually, one week is necessary to create and to transfer

the three cells to the DF.

After a few weeks, the polarizing process efficiency is greatly reduced, because the relaxation time grows longer. The cells polarize and age in the DF for a total period of about three months. This ensures the relaxation time will be long enough, when the cells are placed in the TC condition, to minimize the losses during the transfer process.

Figure 2.7 shows the evolution of the proton polarization in the DF for one of the target used during the experiment described in Chapter 3.

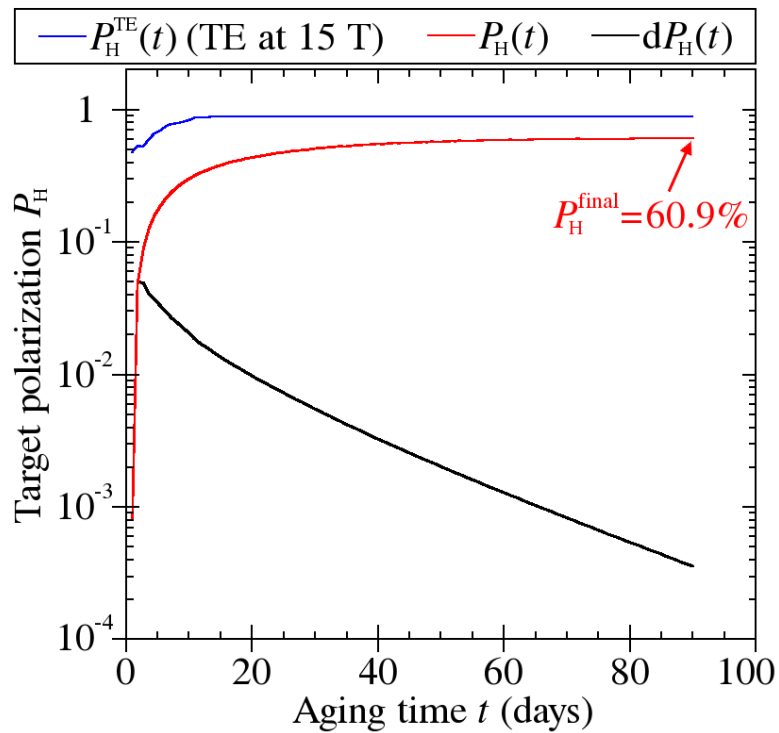


Figure 2.7: Evolution of the proton polarization in the DF to its thermal equilibrium with the aging time. Figure, courtesy of A. Sandorfi.

2.3.6 Polarization measurement

After the target cell extraction from the DF, H and D polarization measurements are performed in the PD to verify that the polarizations are high. Then, the polarizations are monitored for a couple of hours to confirm they do not change, i.e. that the relaxation times are long enough.

In the case of a low polarized cell, one cannot improve the HD polarizations. Two of the first three cells made for experiment g14 (see section 3.1) had low polarization because the initial relaxation times of the HD was already too long when the polarizing process started and, to a lesser extend, because the temperature of the DF was too high for too long.

If the relaxation time of the H or D, T_1 , is short, it means the initial T_1 was too short and the HD did not age long enough. If there is no immediate need for the cell and if the polarization losses during transfers and measurements were acceptable, the cell can be transferred back to the DF to age more. However, if the cell is needed for the experimental program, one can attempt to transfer the cell to the IBC as fast as possible, since in the colder IBC condition (50 mK instead of a few K), T_1 becomes large enough due to its temperature dependance.

2.3.7 Transport to hall

The PD, the SD and the DF are located in the HDice lab and the IBC is located in the experimental Hall B of Jefferson Lab (section 3.2.1). The HDice lab is about 400 meters away of the hall, as the crow flies, and about a kilometer along the standard truck route. Thus, after the target cell has been transferred to the PD or the SD, it is placed on a truck and moved to the hall alongside with the TC.

The cell can then be transferred to the IBC for the duration of the experiment. At the end of the experiment, the cell is transferred back to the PD or the SD and can be transported back to the HDice lab.

2.3.8 Final polarization measurement

Once the experimental use of the cell is over, the final polarizations of the HD are measured in the PD. The measurements can then be compared with the initial frozen spin measurements discussed in section 2.3.6 and with the thermal equilibrium measurement to confirm the calibration of the polarimetry made in the IBC.

Possibly, other studies can occur with the remaining polarization of the HD. Such studies can include spin diffusion study⁴, spin transfer improvement (section 4.3), T_1 measurements, new TE measurement with different configuration, etc.

2.3.9 Gas collection and storage

Finally, the HD can be retrieved by evaporating it in the PD.

To evaporate the HD, the needle valve of the PD is closed to increase the temperature: when the needle valve is closed, the VariTemp space runs out of liquid helium and the temperature of the cold-finger of the PD increases above 50 K (HD boiling point is about 20 K at 1 atm). Once the HD is evaporated in the sample space, the gas can be collected.

Then, the gas is pumped out of the cold finger by condensing it in a cold trap slowly lowered in a liquid helium supply dewar. After condensing and evaporating back and forth into smaller and smaller volume, the HD gas can be stored in a tank with minimum gas loss.

⁴Spin diffusion [42] is a process of continuous exchange of energy between the individual nuclear spins of the HD. It is characterized by a relaxation time T_2 . It allows to reduce the polarization differences within the sample faster than the T_1 relaxation effects. This effect is useful to study, because local depolarization can occur when the target cell is exposed to the beam.

Chapter 3

Experiment with the HDice target

3.1 Motivations

3.1.1 Photon beam run

The g14 experiment [19] took place between November 2011 and May 2012 in the Hall B of Jefferson Lab (see section 3.2.1). The goal of the experiment was the search for neutron resonances (N^*) in hyperon photo-production with a polarized HD target.

The Constituent Quark Model predicts many resonances that appear to be missing from the currently observed spectrum of πN states, while other models do not predict such resonances. Thus, to understand the nucleon structure within QCD, it is essential to characterize this excitation spectrum. Prior to g14, most of the available data had been taken with proton targets and very few neutron data were available. The g14 experiment thus offered the opportunity to expand this database by measuring simultaneously multiple channels ($\pi^- p$, $\pi^+ \pi^- N$, $K^0 \Lambda$, $K^0 \Sigma^0$ and $K^+ \Sigma^-$). In the meantime, a complete measure of the $\gamma N \rightarrow K^0 \Lambda$ amplitude was possible with the determination of 13 different polarization observables.

However, the goals of the g14 experiment could not be entirely fulfilled, because

of a target polarization somewhat lower than expected in the proposal and a lack of time. The g14 experiment ran just before the 12 GeV upgrade accelerator shutdown and it was not possible to extend the run to compensate for delays in the installation.

Nonetheless, the HD target enabled the collection of unique data, which will help to study the excited nucleon spectrum. During the g14 experiment, the HD target provided, for several weeks, highly polarized hydrogen (up to $\sim 50\%$) and deuterium (up to $\sim 30\%$ after spin transfer, see section 4.3) nuclei with little dilution compared to other polarized cryogenic targets. Although no new photon experiment is scheduled for the Hall B's 12 GeV program with the HD target, the target now constitutes a standard equipment for Hall B. Since the photon tagger will remain in the Hall for use with photon beams, extensions of the g14 experiment could be run during the 12 GeV era of Hall B. Alternatively, using the HD target in the new JLab Hall D, dedicated to photon beam experiments, is another possibility.

3.1.2 Electron beam test runs

In between photon runs, two electron test runs were performed during the g14 experiment. The purpose of those tests was to check the target polarization survival under an electron beam of typically a few nA current.

In the past, HD targets have been exposed to electron beams [43], but never with polarized targets in frozen spin mode. The relaxation time was measured after irradiation of an HD target with electrons (using the thermal equilibrium at a temperature of 1.7 K) in the Cornell electron synchrotron [43] and with protons in the Alternating Gradient Synchrotron (AGS) at Brookhaven National Laboratory (BNL).

For the first time, HD in frozen spin mode was monitored under an electron beam. Unfortunately, the two tests were done with low polarized (less than 5%) targets, when accidental quenches during the g14 run had dropped the polarizations to values that were too low for use in the photon experiment. Although those polarizations were not enough to be extracted from physics reactions, such as elastic scattering, it was still possible to monitor them through NMR measurements, as discussed in Chapter 5.

3.2 Experimental setup

3.2.1 Accelerator Facility

The data for the analysis discussed in chapters 5 and 6 have been taken at the Thomas Jefferson National Accelerator Facility (TJNAF), also known as Jefferson Lab (JLab), in Newport News, Virginia. Its main research facility is the Continuous Electron Beam Accelerator Facility (CEBAF), which consists of an electron accelerator (see figure 3.1) and three separate experimental halls: A, B and C. The main objectives of JLab are to conduct research on the atomic nucleus and the nucleon, and to study the fundamental laws of nature, mostly the strong interaction and searches for physics beyond the Standard Model.

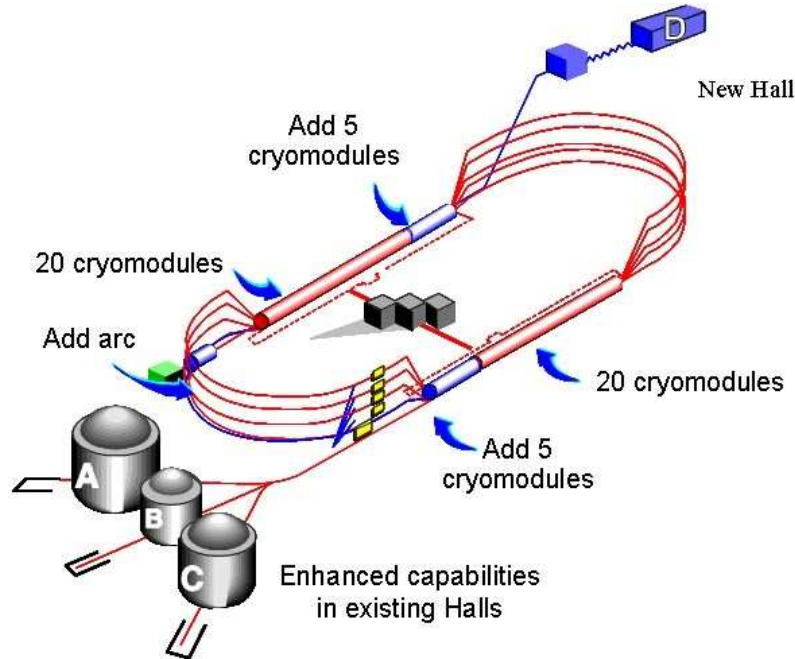


Figure 3.1: Schematic representation of the Jefferson Lab accelerator, including the 12 GeV upgrade.

The accelerator consists of polarized electron sources, an injector and a pair of radio frequency linear accelerators (LINAC) connected by two sets of recirculation

arcs which contain steering magnets. Each LINAC is made of 160 Superconducting Radio Frequency (SRF) cavities. Those cavities are made of superconducting niobium in a liquid helium bath. Every pass in one of the LINAC increases the energy of the electrons by 600 MeV.

At the electron source, laser light hits a gallium arsenide (GaAs) photo-cathode to knock off electrons. An anode provides an initial acceleration of 100 kV to the electrons, which are then accelerated to 67 MeV by 18 superconducting radio frequency cavities. The electrons are injected into the first LINAC in bunches of less than 1 picosecond in length every 670 picoseconds. Then, they are steered to the second LINAC through one of the five arcs at the end of the first LINAC to receive further acceleration. Finally, they are either sent back to the first LINAC through one of the four arcs of the second recirculation arc set or sent to one of the halls. The electrons can undergo this cycle for a total of 5 passes and be accelerated to a maximum energy of 6 GeV.

The electron beam is highly polarized: about 85%. The polarization of the beam can be measured by a Mott polarimeter [44] located at the injector, Møller polarimeters [45] at the entrance of each hall and Compton polarimeters [46] in Hall A and C.

In 2015, the accelerator will be upgraded to reach a maximum energy of 12 GeV by improving SRF cavities and adding 40 new ones to each LINAC. A fourth experimental hall, Hall D, will also be added as well as an additional recirculation arc to the second recirculation arc set.

3.2.2 Hall B

Hall B is 30 meters in diameter and 20 meters from floor to ceiling. At its center is located the main tool of the Hall B physics program, the CEBAF Large Acceptance Spectrometer (CLAS). Experiments in Hall B may either use electron beams or photon beams.

3.2.2.1 Beam-line

Once the electron beam enters the hall, it goes through the Møller polarimeter, Beam Position Monitors (BPM) and Harp scanners. The Møller polarimeter measures the beam polarization. Such a measurement is invasive: no experimental data can be taken at the same time. The BPMs measure the intensity and position in the plane orthogonal to the beam. They also allow to keep the beam centered on the target by a feedback mechanism. The Harp scanners measure the profile of the beam (invasive procedure). Then, it enters the CLAS detector, where it interacts with the target. Finally the beam is terminated in the beam dump, where it is stopped by a Faraday cup that collects the charge of the beam. The time derivative of the collected charge provides the main beam current measurement in Hall B.

The Hall B beam-line can be configured either for an electron beam or for a photon beam (see figure 3.2). A few days are required to switch from one configuration to another.

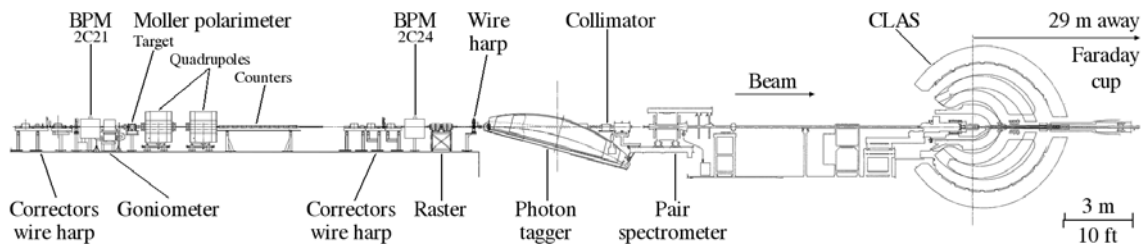


Figure 3.2: Schematic of the Hall B beamline in photon run configuration.

When it is configured for the electron beam, a raster [47] is added on the beam-line after the photon tagger and right before the target and the entrance in the CLAS detector (see figure 3.3). The raster spreads the very thin electron beam coming from the accelerator (about 0.2 mm in diameter) to cover a larger area of the target (15 mm in diameter). If the beam was directly sent on the target, it would cause a local heating and the loss of the polarization at the center of the target. The current would have to be reduced to prevent it and less physics events would be generated.

The photon beam can be produced from the electron beam by placing a thin radiator (located in the goniometer), a photon tagger [48] and collimators before the target. When the electron beam passes through the radiator, the electrons scatter

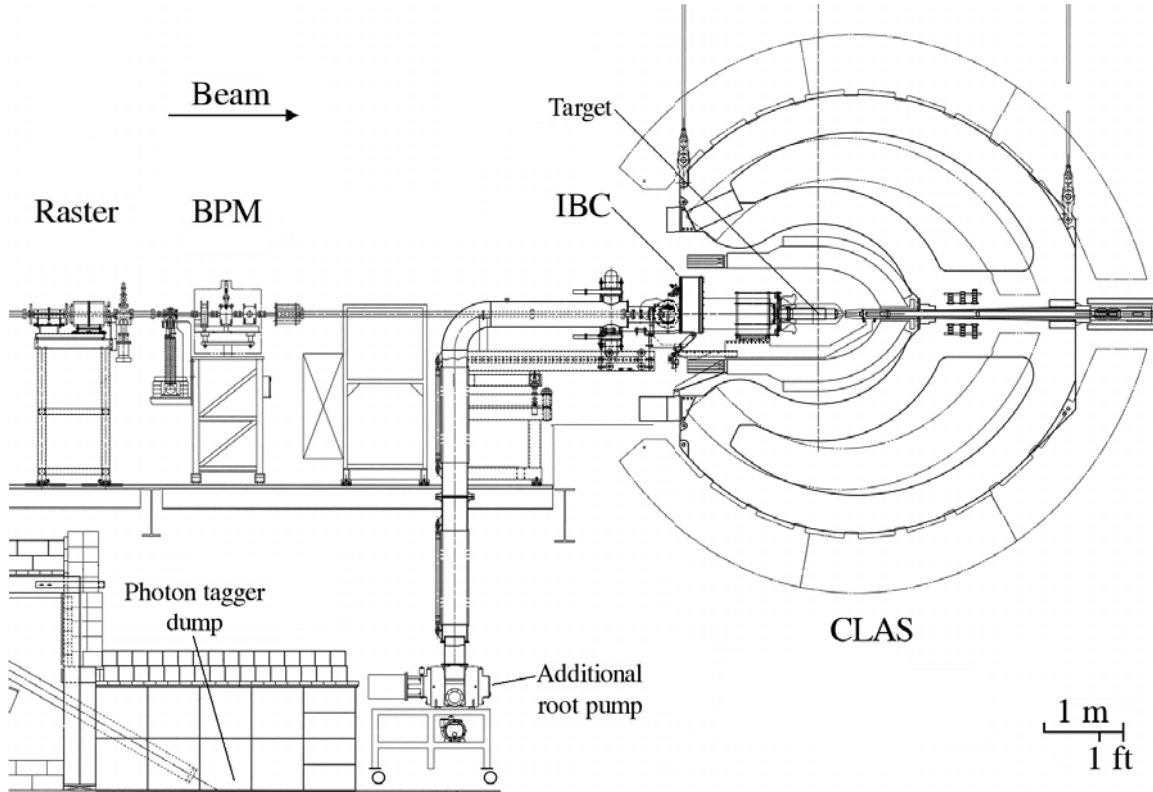


Figure 3.3: Schematic of the HDice target in CLAS in the electron run configuration.

slightly and produce Bremsstrahlung radiation. Then, the electrons are swept away from the photon beam by a magnet providing a dipolar field. While the full energy electrons go to the local beam dump of the tagger, the lower energy electrons, which generated Bremsstrahlung photons with significant energies (between 5% and 95% of the beam energy), face greater curvature and are detected by scintillator hodoscopes that provide the position of those electrons on the scintillator focal plane. This together with the knowledge of the magnetic field allows to measure the energy of the electron. Because the energy transferred to the nucleus of the radiator is negligibly small, it is possible to determine the energy of the photons E_γ with the relation:

$$E_\gamma = E_0 - E_e, \quad (3.1)$$

where E_0 is the beam energy and E_e is the energy of the outgoing electron measured by the tagger. Then, the photon beam passes through a set of collimators to define its profile and to avoid exposing the target walls, which could create background and

possibly damage fragile electronics. In Hall B, depending on the configuration, the photon beam can be polarized differently [48]. The combination of an amorphous metal radiator (often gold) and a longitudinally polarized electron beam is used to produce circularly polarized photons, while the combination of a diamond radiator and an unpolarized electron beam is used to produce linearly polarized photons.

3.2.2.2 Target

The HDice target used during the experiment with photon and electron beams and described in chapter 2 was placed at the center of the CLAS detector in the In-Beam Cryostat (IBC) (section 2.2.6), as shown on figure 3.3.

All the cryogenic and magnetic parameters of the IBC were under constant watch from one of the persons on shift. Special attention to the target temperature was paid when the target was under beam.

All the polarization measurements used for the analysis discussed in chapter 5 were taken with this cryostat during the electron beam runs. For those runs, a large root pump was attached to the cryostat to provide additional cooling (see figure 3.3).

3.2.2.3 CLAS detector

The CLAS detector [49] is at the center of Hall B and is a 9 meter large, roughly spherical, detector (figures 3.4 and 3.5). It is used to study the structure of mesons, nucleons, and nuclei using polarized and unpolarized electron and photon beams and targets. It is made of multiple layers of detection systems assembled around a six-coil toroidal magnet, the Torus magnet. It enables the classification and the kinematic measurement of the detected particles in a large fraction of the full solid angle.

The Torus magnet [50] provides a largely azimuthal magnetic field distribution with six large toroidal superconducting coils. The trajectories of the charged decay particles are curved by the field, which allows to determine their momentum. The coils segment the detector into six sectors.

Each sector consists of three regions of Drift Chambers (DC) (each region sitting

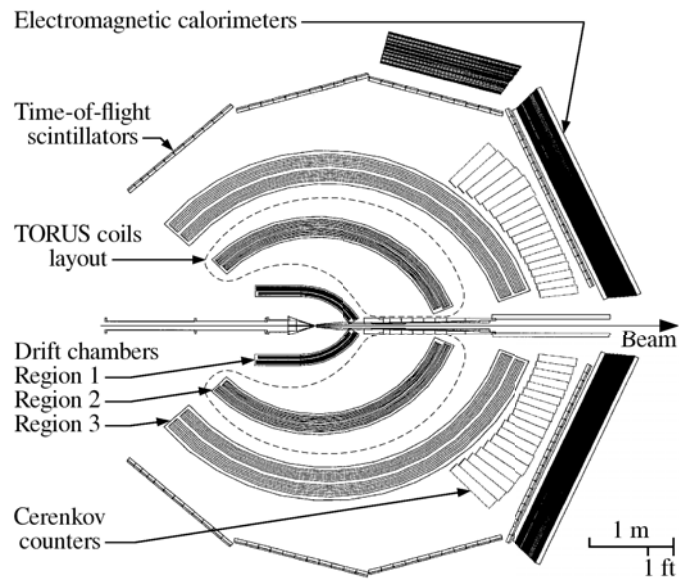


Figure 3.4: Side view of CLAS with its different subsystems.

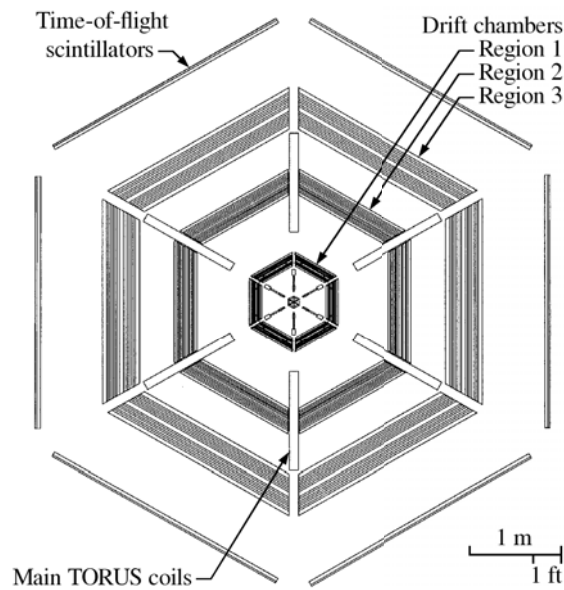


Figure 3.5: Front view of CLAS with its different subsystems.

at different radii: one inner, one middle and one outer DC region), Čerenkov Counters

(CC), Time-Of-Flight (TOF) scintillators and a forward Electromagnetic Calorimeter (EC). The drift chambers [51] allow to reconstruct the trajectories of charged particles and to determine their momentum. They are made of thousands of thin and long hexagonal drift cells in a mixture of argon (90%) and carbon dioxide (10%). The Čerenkov counters [52] are filled with perfluorobutane gas (C_4F_{10}), and help to identify light charged particles (electrons or positrons) when they pass through and emit Čerenkov radiation. The high refraction index of the gas ($n = 1.00153$) provides a pion momentum threshold of 2.5 GeV/c. The time-of-flight scintillators [53] are coupled with Photo-Multiplier Tubes (PMT) to measure the time-of-flight of the particles going between the target and the scintillator paddle. The “zero” time is given by the beam bunch arriving on the target. The time structure information of the beam is provided by the accelerator. The calorimeter [54] is made of 39 triangular shaped layers of lead and scintillator. It measures the deposited energy of the particles within the scintillator layers. Since the fraction of energy deposited in a given length of material depends on the particle mass, the calorimeter helps to identify the type of particle. Furthermore, since the fraction of deposited energy in a given material is well known, the calorimeter provides an alternate energy (i.e. momentum) measurement for the particle.

Chapter 4

Polarimetry technical aspects

4.1 HDice NMR system

4.1.1 Apparatus

The Nuclear Magnetic Resonance (NMR) system for the HDice target [55] (see figure 4.1) is made of:

- An Oxford IPS120-10 power supply which provides the current to the main solenoid of the dewar;
- A superconducting solenoid magnet which creates the main magnetic field in the z direction which causes a splitting in the energy levels of nuclei (see section 1.2.1);
- A Rohde and Schwarz SMB100A (or SMY01) signal generator which generates a Radio-Frequency (RF) signal to induce transitions between the energy levels split by the magnetic field. The frequency of the signal depends on the main magnetic field (usually, in the range of the megahertz with our typical values used for magnetic fields from ~ 0.1 to ~ 1 T);

- A module switching box which can attenuate the RF signal from 0 to -63 dBm by using highly reliable Pasternack attenuators. It also allows to switch between the regular NMR circuit and the spin transfer circuit. This latter circuit adds an amplifier to the circuit which increases the power of the RF signal;
- Two RF coils. The first coil is a transmitter which carries an RF signal from the generator and creates the RF magnetic field oriented in the x direction (see figure 4.7). The second coil is a receiver which provides a measurement of the RF response, in the y direction, of the material in the cell to the RF field applied to the target. The coils are in a “cross coils” configuration to minimize any magnetic flux from the transmitter coil passing through the receiver coil. Nevertheless, the transmitter coil still induces a signal into the receiver coil, which needs to be separated from the NMR signal;
- A Stanford Research Systems SR844 lock-in amplifier which extracts the NMR signal from the RF signal generated by the RF generator and also provides data acquisition;
- A computer which interfaces all the devices together and provides control during NMR measurements through LabVIEW¹ Virtual Instruments (VI). The current version (VI) used to make the NMR measurements allows us to perform a measurement (up and down sweeps) every two minutes.

All of those components, but the solenoid magnet and the NMR coils, are placed into a rack. The magnet and the coils are located inside the cryostat. The magnet is connected to the power supply with standard high current insulated copper cables. The coils are connected to the rest of the system with long water-cooled semi-rigid RG401 coaxial cables. The cables are cooled to about 10°C, because their material is temperature dependant and undergoes a transition near 18°C which changes the resistance of the cable. Because this temperature is close of the room temperature, the amplitude of the signal could change between two measurements if no cooling was provided. Therefore, the cooling of the cables avoids the transition and ensures a stable behavior of the cables. As each NMR measurement induces transitions between levels that reduce the target polarization, it is required to use as little power as possible. Thus, the whole system is designed to reduce the noise-over-signal ratio.

¹LabVIEW is a graphical programming environment from National Instruments. It allows to interface many instruments together with ease.

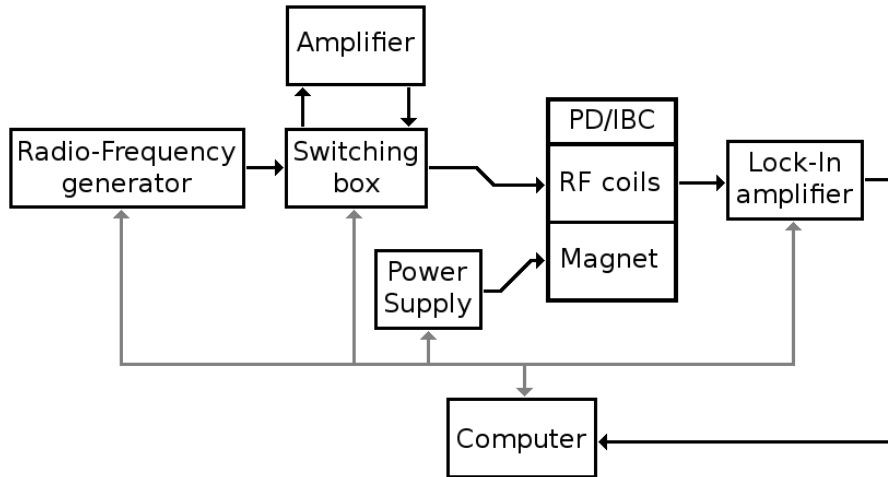


Figure 4.1: Schematic of the NMR system used for the HDice target.

4.1.2 Fast resonance scan - System response

The Fast Resonance Scan (FRS) measures the frequency dependency of the RLC circuit, which presents multiple resonances at different frequencies (see figure 4.2). This is done by measuring the magnitude and phase between the input RF and the output signal of the circuit response at different frequencies. The FRS provides the information needed to choose a frequency for the NMR measurements at which the signal-to-noise ratio is favored and to detect any change that could occur in the circuit that would require a new calibration of the system. Because the amplitude of the NMR signal depends on the magnitude of the response of the circuit, using one of the resonance frequencies maximizes this signal. The magnetic field range will be chosen so that with the choice of frequency (see section 4.1.3.1) the NMR condition is met (see equation 1.16).

The scans do not require any magnetic field, although if a target is present field is needed to maintain polarization. Thus the FRS must avoid passing the NMR resonance condition of any material, because they are performed at high power. This is especially true when a highly polarized target is in use, as a scan could considerably affect the target polarization. In this case, the frequency range is tightened to the range of interest and the magnetic field is shifted away of the resonance conditions at those frequencies (see equation 1.16).

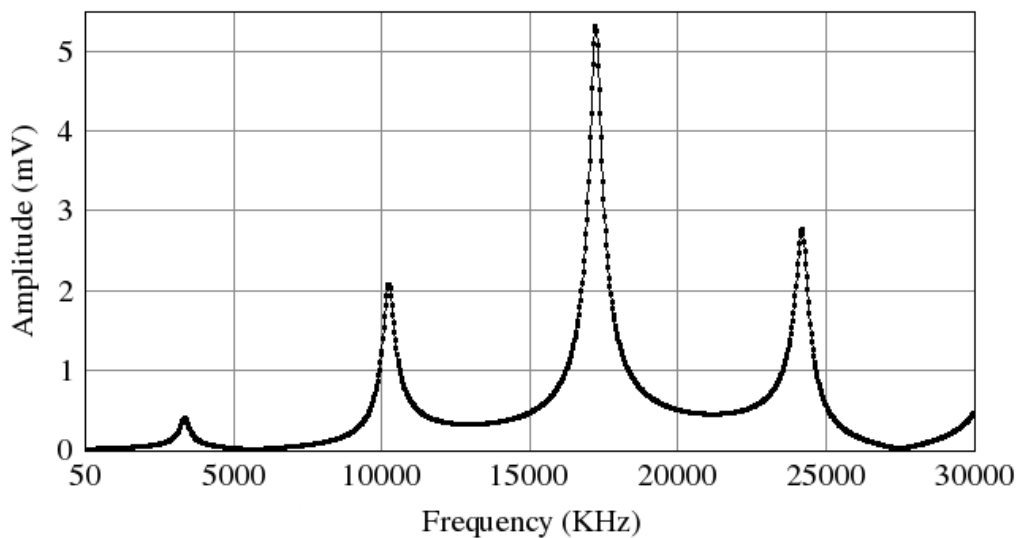


Figure 4.2: Example of a fast resonance scan in the PD.

4.1.3 NMR measurements

Two methods can be used to perform NMR measurements: field sweeps or frequency sweeps.

4.1.3.1 Field sweeps

Field sweeps consist of setting the frequency of the RF field and varying the magnitude of the main magnetic field (see figure 4.3). When the field passes the resonance condition, equation 1.16, we observe the NMR response of the target².

This is the method used for the polarimetry of the HDice target in the Production Dewar (PD) and the In-Beam Cryostat (IBC). Indeed, if no change occurs in the circuit and the RF frequency remains the same, the calibration of the system should not depend on the main magnetic field magnitude or change from one run to another.

²At a frequency of 10 MHz, the resonances of the proton and deuteron occur at magnetic fields of about 0.24 T and 1.55 T respectively.

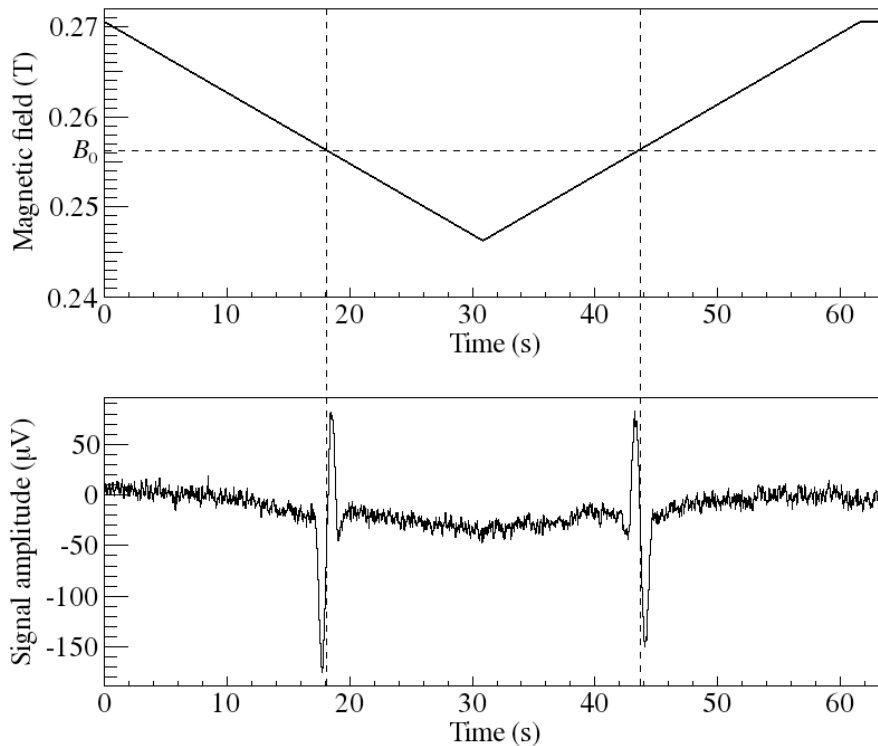


Figure 4.3: Passage through the NMR resonance (twice) during a field sweep (hydrogen). The top plot shows the magnetic field sweep and the bottom one the response of the receiver coil. The NMR resonance occurs at B_0 and induce the peaks.

For the HDice target, the procedure for such NMR measurements begins with the configuration of the system (frequency, power, etc). The data acquisition is made through the lock-in amplifier, which ensures that the data points are taken with a constant rate. The data acquisition is triggered as soon as the magnetic field starts to be ramped down, and it is stopped when it has been ramped back up. Then, for every sweep, the data are copied from the lock-in amplifier internal data buffer to the local disk of the computer. Thus, with this method, the NMR resonance condition is passed twice before coming back to the initial value of the magnetic field.

While for the fast resonance scans, the magnitude and the phase of the circuit response signal are monitored, the NMR absorption (x channel of the lock-in amplifier) and emission (y channel of the lock-in amplifier) spectra are monitored instead for an NMR measurement.

4.1.3.2 Frequency sweeps

For frequency sweeps, the main magnetic field is set while the frequency of the RF field is changed³.

This method has the great advantage that it does not require changes in magnetic field. Thus, it can be used with a magnet in persistent mode (section 2.2.1) and permits to measure both proton and deuteron polarizations without delay if the response of the circuit at those frequencies is acceptable. However, the efficiency (Q) of such a circuit is both temperature dependent (so RF heating during a measurement can alter the response) and frequency dependent (so that the background changes with frequency across the sweep). These issues can be handled with sufficient research and development (as is the case with the popular "Liverpool Q-meter" that is frequently used with a single loop NMR system). Field sweep offers an attractive alternative with a cross coil system, since the response is less temperature sensitive and the background is independent of the field. We remark that the Hall A helium-3 target, which uses a cross-coil NMR system design similar to the one of HDice, employs both field and frequency sweeps for polarimetry.

Currently, for the HDice target, frequency sweeps are primarily used to follow any change in the magnitude of the magnetic field in the Dilution Fridge (DF). In the future, frequency sweeps will be developed to enable the monitoring of the target polarization in cryostats for which field sweeps cannot be done, such as the DF and the Storage Dewar (SD). The SD magnet presents large hysteresis, due to manufacturing defects, and thus no reproducible down and up field sweeps can be done. And the magnetic field of the DF is too large to be moved, because moving it would create eddy currents which would significantly alter the polarizing temperature.

4.2 T_1 measurements

Relaxation time T_1 measurements, as mentioned in section 2.1.3.1, perturb the equilibrium of the system in order to perform NMR measurements to observe the

³At a magnetic field of 1 T, the resonances of the proton and deuteron should occur near the frequencies of 42.5 MHz and 6.5 MHz respectively.

recovery time of the polarization of the target to the thermal equilibrium (see equation 2.1). Finally, a fit on the data taken with the NMR measurement allows a determination of T_1 at given conditions (target temperature, aging (i.e. impurity levels) and magnetic field).

The time span between NMR measurements depends on the value of T_1 . Indeed, a short T_1 of the order of a minute requires measurements every few seconds, while a longer one (of the order of a month) only needs a measurement every one or two days.

The equilibrium can be perturbed in two ways. The first one consists of erasing the initial polarization by inducing a lot of transitions between energy levels with a high RF power to equalize them. We then measure the polarization growing back to the thermal equilibrium (see figure 4.4). This is adequate for targets that are not in frozen spin mode, having a relatively short T_1 , and is typically used for gas characterization (see section 2.1.3.3).

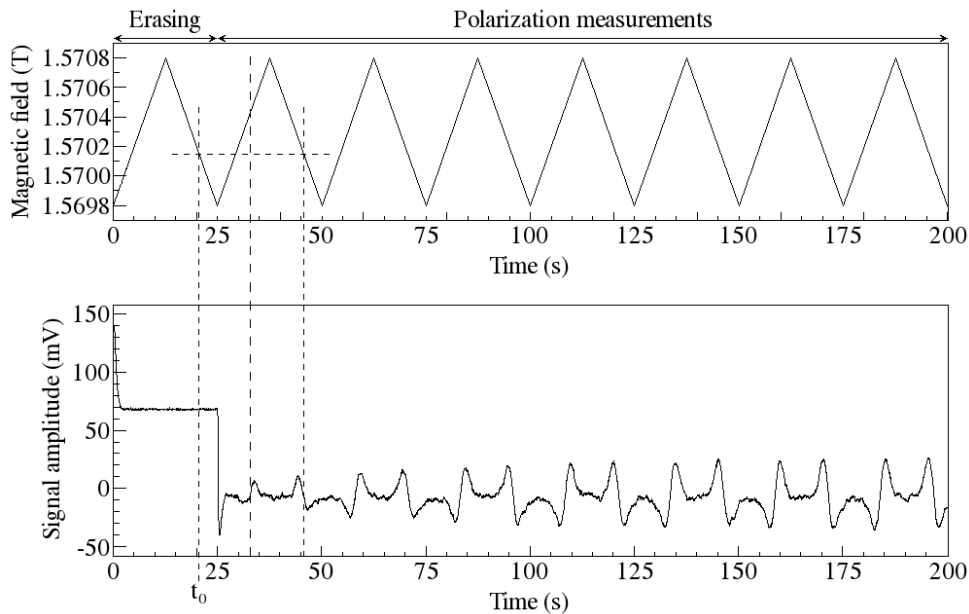


Figure 4.4: T_1 measurement of a short relaxation time target (deuterium).

The second way consists of modifying the thermal equilibrium value, which is easily done by changing the target temperature or the magnetic field magnitude. It

can be used with any target under the condition that its T_1 is long enough (at least 10 minutes long). Indeed, changing the magnetic field or the temperature cannot be done quickly, in contrast to killing the polarization. However, this method is well suited for polarized targets that have long T_1 of the order of hours or more, because the time to reach to a new condition is negligible compared to T_1 .

Because the NMR system presented in section 4.1 can only make an NMR measurement every two minutes, it is more suited to monitor T_1 for polarized target with long T_1 . For shorter T_1 , a faster, yet similar, system is preferred (see figure 4.5). The main differences are that this system uses a diode amplifier, frequency modulation and an oscilloscope for data acquisition. This system is used to characterize samples of new HD gas before it is selected to make a target. The gas sample characterization is carried out in the “Qualifier”, which consists of a small cell ($\sim 1 \text{ cm}^3$) with built-in RF coils at the end of a two-meter long tube. The gas is condensed into the cell through the tube and the RF coils are wound around the cell.

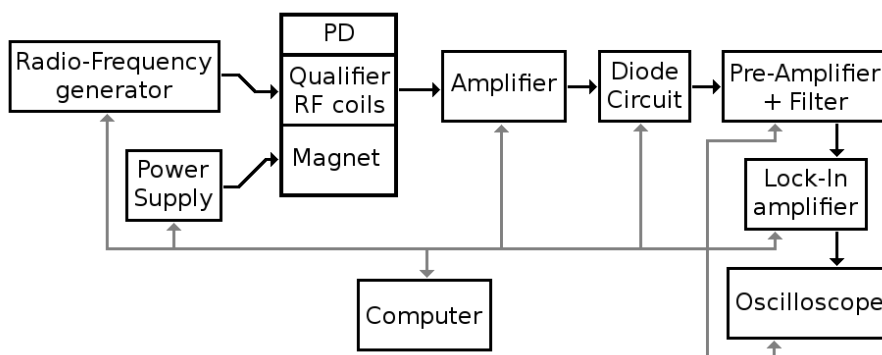


Figure 4.5: Schematic of the NMR system used with the Qualifier for the HDice target.

4.3 Spin transfer

After the polarization procedure discussed in section 2.3.5, the initial proton polarization ($\sim 60\%$) is about a factor three larger than the deuteron one ($\sim 20\%$). Although it is difficult to increase the polarizations using the static polarizing method, it

is possible to improve the deuteron polarization, at the cost of some loss of the proton one, by rearranging the repartition of the proton and deuteron spin populations.

Ideally, the spin transfer would be made using the Forbidden Adiabatic Fast Passage (FAFP) technique. The FAFP consists of inducing transitions between the energy levels of the proton and deuteron to equalize their spin populations, as shown on figure 4.6. Those transitions are forbidden within the proton and deuteron of a same molecule, but are permitted with the ones in their neighborhood. The result is a much higher deuteron polarization and a lower proton one; every percent gained in the deuteron polarization results in principle in two percent loss in the proton one. However, this technique requires a very efficient system with very uniform fields (holding field and RF field) and a high RF power. Currently, for the HDice target, this transfer is performed by a different technique, the Saturated Fast Passage (SFP). The technique is very similar to the FAFP, but aims to equalize the spin populations instead of reversing them.

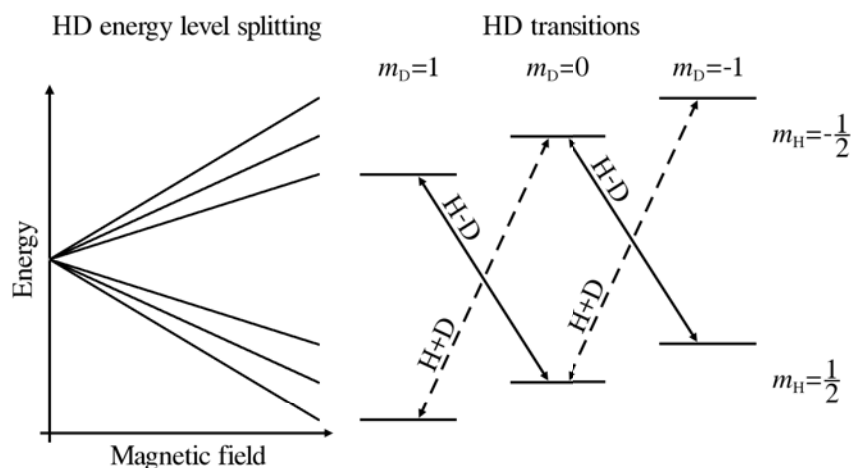


Figure 4.6: Energy level splitting and transitions between levels in HD.

As seen on figure 4.6, two types of transition are possible:

- H-D transitions⁴, which can result in an increase of the deuteron polarization and a decrease of the proton one, between spin states:

⁴At a magnetic field of 1 T, the H-D transitions occur near the frequency of 36 MHz.

- $(m_H = \frac{1}{2}, m_D = -1) \leftrightarrow (m_H = -\frac{1}{2}, m_D = 0)$, or
- $(m_H = \frac{1}{2}, m_D = 0) \leftrightarrow (m_H = -\frac{1}{2}, m_D = 1)$.

- H+D transitions⁵, which can result in a much larger decrease of both polarizations, which become anti-parallel, between spin states:

- $(m_H = -\frac{1}{2}, m_D = -1) \leftrightarrow (m_H = \frac{1}{2}, m_D = 0)$, or
- $(m_H = -\frac{1}{2}, m_D = 0) \leftrightarrow (m_H = \frac{1}{2}, m_D = 1)$;

The SFP procedure is made using the H-D transition lines by using the emitter coil resonance frequency to improve the RF transitions in the target instead of increasing the RF power. Capacitors are added to tune the circuit and to adjust the resonance frequency position. Generally frequency modulation is used to pass through the resonance condition as many times as possible. The spin transfer is performed at a magnetic field of about 700 Gauss. Several identical sweeps (5 to 10) are repeated until the spins are equilibrated. Because of the high RF power used, the temperature of the target increases significantly and it is necessary to wait between sweeps until it cools down to an acceptable level. Then, both polarizations are measured and the process is repeated if necessary. During the experiment (described in chapter 3), in the IBC, 40 to 50 sweeps were required to perform this transfer and the temperature of the target was varying from 80 to 180 mK. For one of the targets (target 22b), the H and D polarizations before the SFP spin transfer procedure were 52% and 14% respectively, and were both about 27% after.

While the FAFP is theoretically a reversible procedure, the SFP is irreversible. However, both techniques may present risks of polarization losses. First, they require a high RF power, which increases significantly the temperature of the target and thus reduces the relaxation time of the target. Similarly, the low magnitude of the magnetic field contributes to further relaxation time reduction. Second, in the case of a mismanipulation, if the sweep span is too wide, the resonance condition of the proton (about 15% away of those transitions conditions) can be reached. Due to the high RF power, it may completely erase the proton polarization.

⁵At a magnetic field of 1 T, the H+D transitions occur near the frequency of 49 MHz.

4.4 Spin transfer improvement

Spin transfers are usually long procedures (several hours). They can be sensitively improved by using a more uniform RF magnetic field. A uniform field allows to optimize the power distribution through the target (the power is limited by the heat brought at the center of the target, where the RF magnetic field is the highest) and thus increase the total number of transitions at each sweep. Consequently, less sweeps are required and the overall procedure is faster and less risky.

4.4.1 Field homogeneity definition

The field uniformity u can be computed by the following formula:

$$u = \frac{\sigma_B}{\bar{B}}, \quad (4.1)$$

where σ_B is the standard deviation and \bar{B} the average of the magnetic field B inside the target of radius R and length L , given by:

$$\bar{B} = \frac{1}{\pi R^2 L} \iiint_{\substack{x^2+y^2 \leq R^2 \\ |z| \leq \frac{L}{2}}} B(x, y, z) dx dy dz, \text{ and} \quad (4.2)$$

$$\sigma_B = \sqrt{\frac{1}{\pi R^2 L} \iiint_{\substack{x^2+y^2 \leq R^2 \\ |z| \leq \frac{L}{2}}} (B(x, y, z) - \bar{B})^2 dx dy dz}. \quad (4.3)$$

If $u = 0$, the magnetic field inside the target is perfectly uniform (the value of the field is identical everywhere in the target). In practice, this never occurs and $u > 0$. However, it is still possible to optimize the coils to have u closer to 0.

4.4.2 Birdcage coil project

Just as it was crucial to minimize the main magnetic field inhomogeneities, it is also important to minimize the RF field inhomogeneities. This would allow to

minimize the RF power used in the spin transfer operations (see section 4.3). Using less power would keep the In-Beam Cryostat (IBC) temperature low during the spin transfer, therefore minimizing the polarization transfer losses, and also shortening the time of the manipulation. In addition, uniform main magnetic and RF fields allow to obtain the true shape of the NMR signal. This true shape is expected to be a Lorentzian convoluted with a gate function which width depends on the polarization (see section 5.2.4). This is useful, first as a check that the system is functioning properly, but also because the polarization can be extracted from the width of the NMR signal. This would provide a polarimetry monitoring fully independent of the integration method discussed in section 5.2.4.

A technique to minimize the RF field inhomogeneities is to replace the usual RF saddle coils (see figure 4.7) by birdcage coils (see figure 4.8). They are referred to as “Birdcage coils” due to their resemblance to a bird cage. Each coil is made of a single conductor wire wound around a coil form made of Kel-F (see section 2.1.2) and creates a fairly uniform magnetic field along a unique direction as shown on figure 4.10. Currently, the coils used in the Production Dewar (PD) are 2-pole saddle coils in a cross-coil configuration, while the ones in the IBC are 8-pole birdcage coils in the same configuration. This method has been used successfully in medical MRI [56] [57], but had not been applied yet in the field of nuclear and particle physics. It was implemented for the first time with the Hall B HDice target. The difficulty for such target stems from space constraints: the nose of the IBC is crowded and additional correction coils, as employed in medical MRI, cannot be added. Therefore, it was necessary to carefully simulate an approximate bird cage that would provide an adequately homogeneous RF field. We used the CST MicroWave Studio⁶ [58] software for such a simulation.

A birdcage coil can have as many poles as desired (always a multiple of two). A large number of poles gives a better control on the magnetic field distribution, which usually improves its uniformity. However, the obvious limitations to the number of poles are the available space to wind the coils and the total length of the wire used. A longer wire will increase the inductance and the resistance of the coil, which can alter significantly the efficiency of the coil.

For the IBC birdcage coils, 8-pole coils is a good compromise between having a large number of poles and the space to wind two coils on the same form (a cylinder

⁶CST MicroWave Studio is a specialist tool for three dimensional electromagnetic simulations of high frequency components.

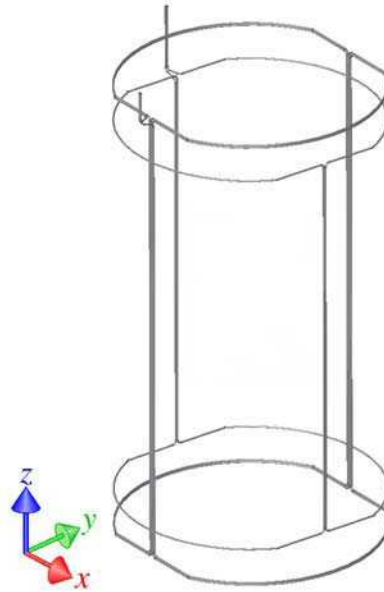


Figure 4.7: Representations of the 2-pole saddle coils in the PD.

of about 4cm diameter).

Prior to building the birdcage coils for the IBC, simulations of the expected magnetic field were performed. The simulations were done with Mathematica⁷ and CST MicroWave Studio. Mathematica simulations provide first order results (e.g. by approximating the wires of the poles as extremely long) and help to optimize the position of the poles in the xy plane of the coils. MicroWave Studio simulations (see figures 4.9 and 4.10) are more complete and closer to reality because they can take into account the edges of the coils, the frequency dependency of the materials used, and the presence of the main solenoid (acting as a ground plane) and the target cell's copper ring. However, those simulations involve a lot of mesh calculation, which can take up to several hours depending on the complexity of the simulation and the size of the mesh.

The MicroWave Studio simulations show a net improvement between the PD coils and the IBC ones. The uniformity (inside the target region) for the PD (2 poles)

⁷Mathematica is a computational software program developed by Wolfram Research. It is a powerful program to solve, integrate and plot equations, which can often provide an analytical solution to the problem.

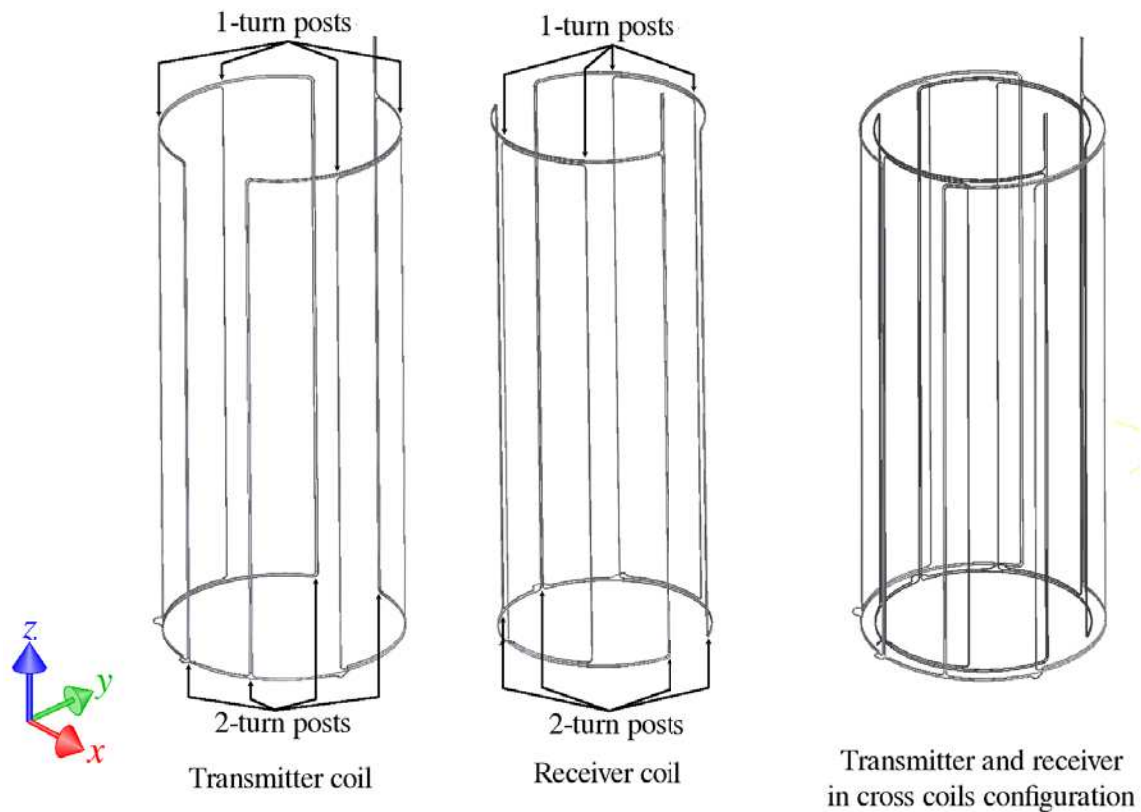


Figure 4.8: Representation of the 8-pole birdcage coils in the IBC. Some posts have two turns to create a stronger magnetic field.

is 16.87%, while the uniformity for the IBC (8 poles) is 3.82% for the shortest coil (70 mm long) and 2.41% for the longest one (76 mm long). Those latter results are consistent with the idea that the wires on the edges of the coil create inhomogeneity near the center. As well, those simulations showed that the target cell's copper ring was far enough of the target region, so that it has a negligible effect on the field uniformity (of the order of 10^{-4}).

The simulations also showed that the uniformity improves as the diameter of the coil increases. However, this diameter cannot be too big due to several limitations. First, as the diameter increases, the inductance of the coil increases slightly and the magnitude of the magnetic field in the center of the coil decreases. Then, the presence of a metal shield (here to preserve the vacuum in the target region) around

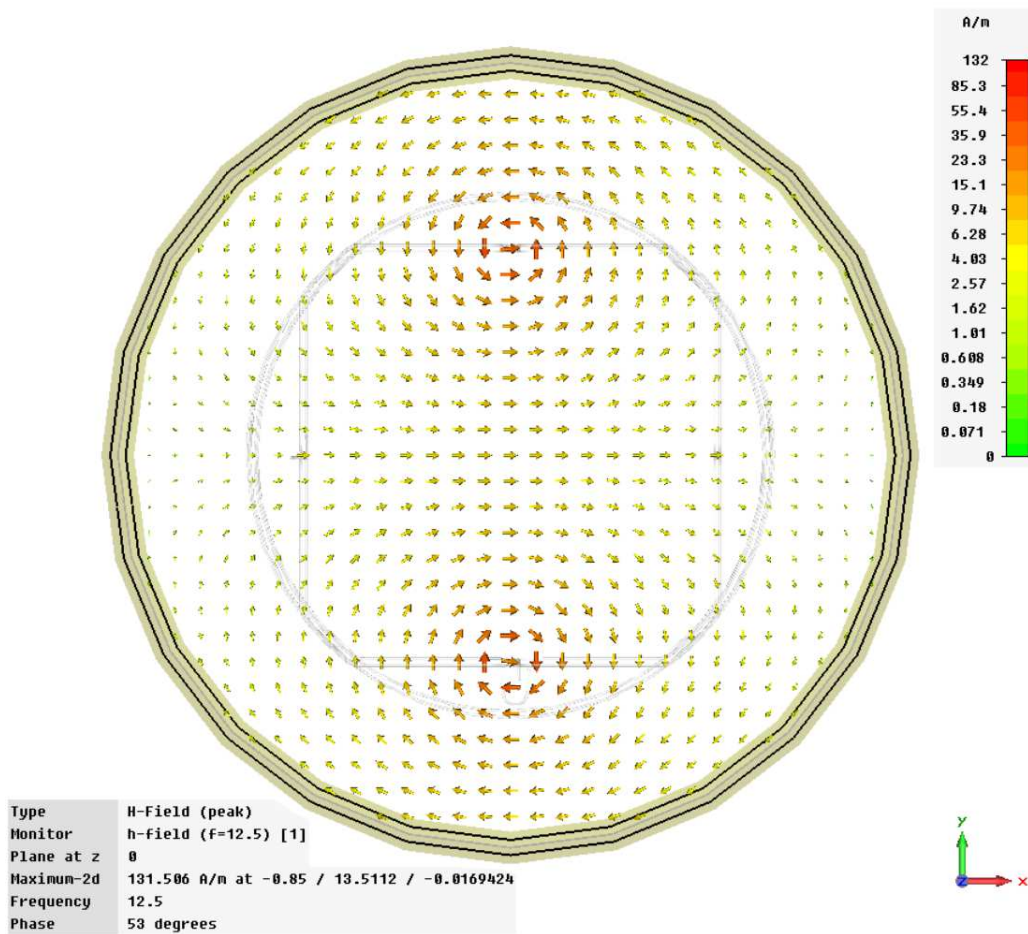


Figure 4.9: Simulation with MicroWave Studio of the magnetic field created by an 2-pole saddle coil in the xy plane in the middle of the coil.

the target adds further constraints. Besides setting a physical limitation on the maximum diameter of the coil (the coil cannot be outside the shield), this shield acts as a mirror for the magnetic field (the mirrored field is in the opposite direction to the incident field) and thus attenuates the magnitude of the field in the center, which slightly alters the uniformity if the coil is not too close to the shield. Therefore, the coil diameter must be large enough to avoid inhomogeneities near the posts and the coil must not be too close to the shield to prevent the cancelation of the magnetic field due to the mirrored field.

Once the design of the birdcage coils was final, a coil form was made (see figure

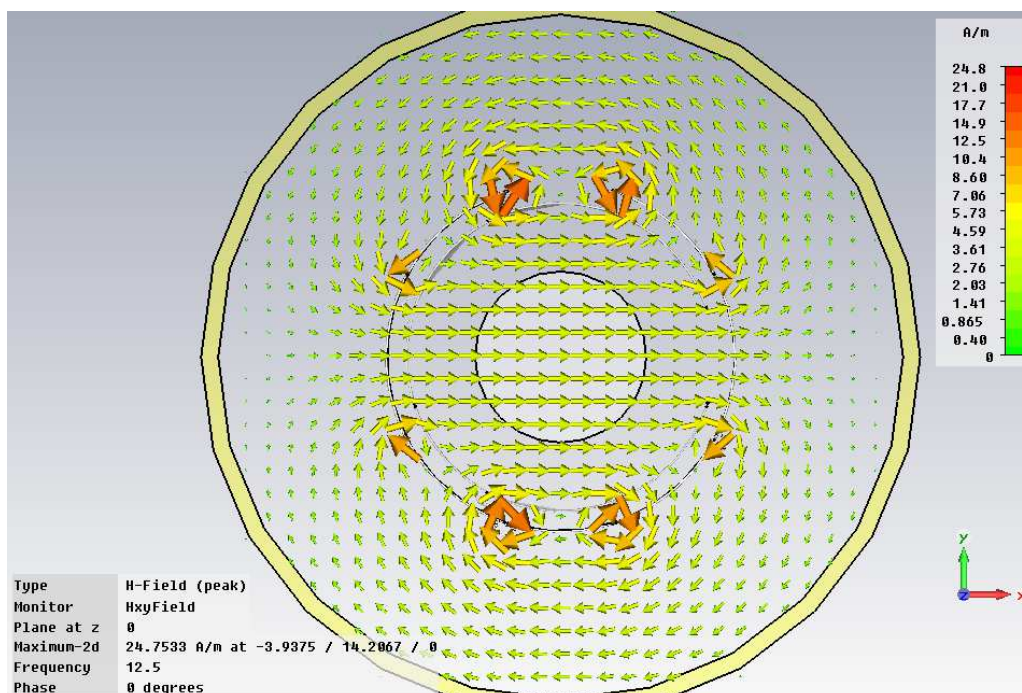


Figure 4.10: Simulation with MicroWave Studio of the magnetic field created by an 8-pole birdcage coil in the xy plane in the middle of the coil. The magnetic field is higher around the four 2-turn posts (top and bottom posts).

4.11) and the coils wound around it. Due to the experimental requirements, the coil form had to be as thin as possible and to stay in the shadow of the CLAS magnetic coils. Therefore, the coil form is very thin (0.7 mm) in the middle. However, it might be possible to slightly reduce this thickness, as well as the one of the sides, with further studies (e.g. by studying the possibility to machine and strengthen a thinner form).

The use of such a birdcage coil for the first time in a nuclear/particle physics polarized target was especially important for the g14 experiment. Although the temperature of the Hall B IBC was cooler than the one for the LEGS IBC, the Hall B IBC cooling power was less and hence, with the birdcage coil configuration, the potential increase of temperature due to the RF power used during spin transfer manipulations was minimized. The time necessary for the saturated transition spin transfer was also greatly improved: it was typically 2 hours with the LEGS IBC and only 20 minutes for the JLab IBC.

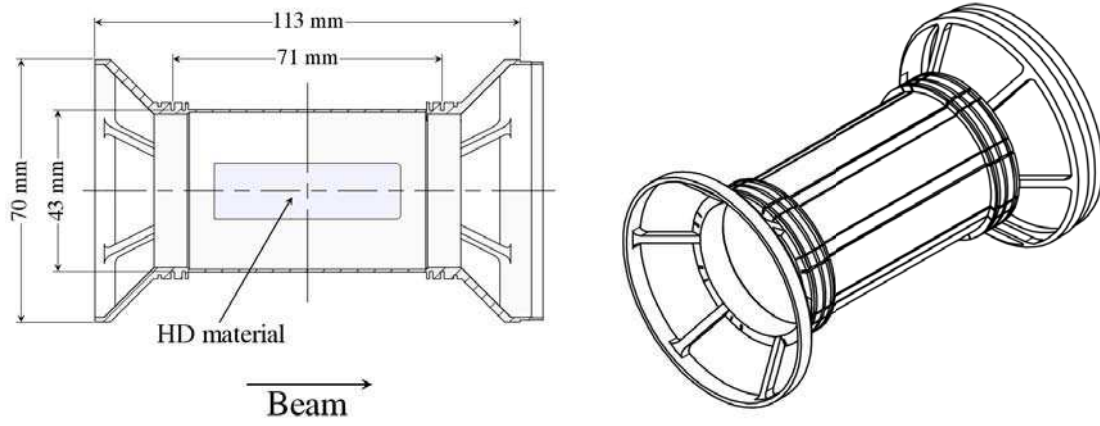


Figure 4.11: Drawing of the birdcage coil form in the IBC.

Chapter 5

Behavior of HD under electron beams

5.1 Introduction

The purpose of this analysis is to obtain the time-evolution of the target polarization during the two electron runs of the HDice experiment (section 3.1.2) by extracting the polarization from the Nuclear Magnetic Resonance (NMR) measurements.

The polarization is extracted by integrating the area under the NMR signal. The signal may require corrections or transformations, that can be made using mathematical transforms in their discrete form, such as the Fourier transform and the Kramers Kronig relations.

5.1.1 Fourier transform

The Fourier Transform (FT) is a mathematical operation (see figure 5.1). In our case of interest, it transforms a function of time, $f(t)$, into a new function of frequency (Hertz or radians per second), $\hat{f}(\nu)$, known as the Fourier transform of the

function f :

$$\hat{f}(\nu) = \int_{-\infty}^{\infty} f(t) e^{i2\pi\nu t} dt. \quad (5.1)$$

The Fourier transform is a reversible operation, as:

$$f(t) = \int_{-\infty}^{\infty} \hat{f}(\nu) e^{i2\pi\nu t} d\nu. \quad (5.2)$$

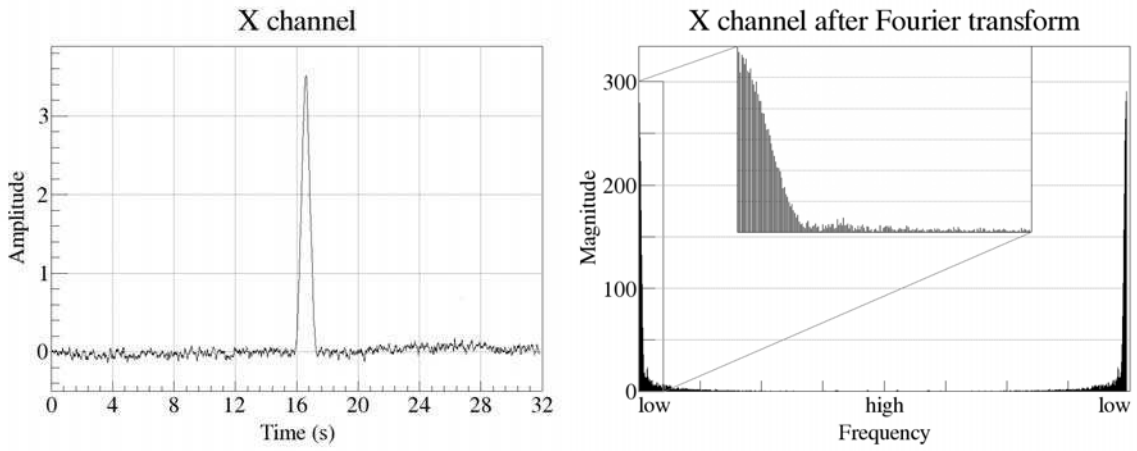


Figure 5.1: Fourier Transform of an NMR signal (Lock-in X channel).

However, for a sampled signal, such as the NMR measurements, the use of the Discrete Fourier Transform (DFT) is more adapted. Indeed, the DFT converts a list of N equally-spaced samples in the time domain, x_N , into a list of N -periodic samples in the frequency domain, X_N . Those latter samples are ordered by their frequencies; the lower ones are closer to the 0 or N indices, while the higher ones are closer to the $N/2$ index. The DFT formula is:

$$X_k = \sum_{n=0}^{N-1} x_n \cdot e^{i2\pi kn/N}, \text{ for } k = 0, 1, \dots, N-1. \quad (5.3)$$

The discrete Fourier transform is also reversible:

$$x_n = \frac{1}{N} \sum_{k=0}^{N-1} X_k \cdot e^{i2\pi kn/N}, \text{ for } n = 0, 1, \dots, N-1. \quad (5.4)$$

5.1.2 Kramers-Kronig relations

The Kramers-Kronig relations are mathematical relations which connect the real and imaginary parts of a complex function (see figure 5.2). These relations are often used to calculate the real part $\chi_1(\omega)$ from the imaginary part $\chi_2(\omega)$ (or vice versa) of response functions $\chi(\omega)$ (equation 5.5) in physical systems, such as the NMR system response (the real part is the NMR absorption spectrum, while the imaginary part is the NMR emission spectrum). They are also used in deriving nuclear and particle physics sum rules based on dispersion relations, such as the Gerasimov-Drell-Hearn (GDH) sum rule, which was the object of the E97110 experiment (see section 6.1) or of the first experiment that used a polarized HD target at the Brookhaven National Laboratory (BNL) [59].

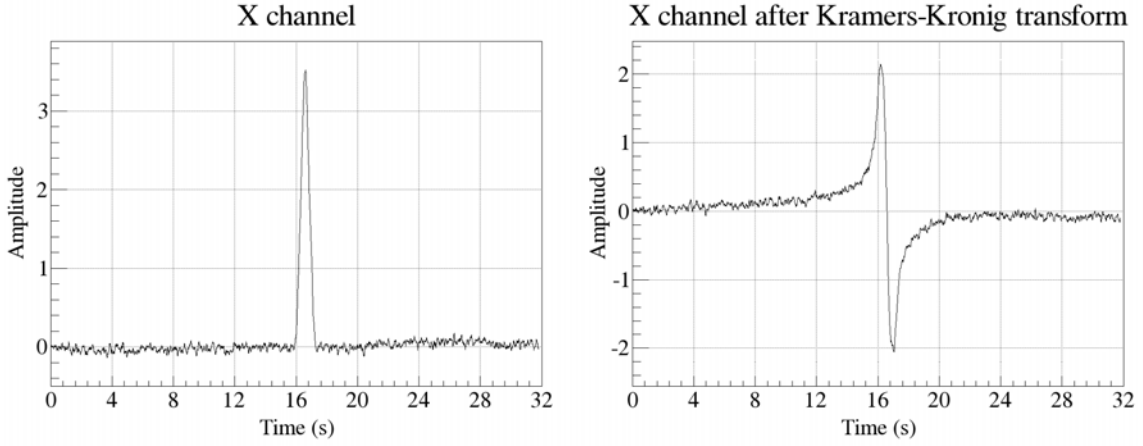


Figure 5.2: Kramers-Kronig transformation of an NMR signal (Lock-in X channel).

The response function $\chi(\omega)$ of a system has real and imaginary parts:

$$\chi(\omega) = \chi_1(\omega) + i\chi_2(\omega). \quad (5.5)$$

The Kramers-Kronig relations connect real and imaginary parts. The relations are analogous to the Hilbert transform [60] and have for expression:

$$\chi_1(\omega) = \frac{1}{\pi} \mathcal{P} \int_{-\infty}^{\infty} \frac{\chi_2(\omega')}{\omega' - \omega} d\omega', \quad (5.6)$$

$$\chi_2(\omega) = -\frac{1}{\pi} \mathcal{P} \int_{-\infty}^{\infty} \frac{\chi_1(\omega')}{\omega' - \omega} d\omega', \quad (5.7)$$

where \mathcal{P} denotes the Cauchy principal value.

Like the Fourier transform, the discrete Kramers-Kronig relations are more adapted to a sampled signal. Therefore, the following relations, similar to the basic Discrete Hilbert Transform derived by Kak [61], can be used:

$$y_k = \begin{cases} \frac{2}{\pi} \cdot \sum_{n \text{ odd}} \frac{x_n}{k - n} & \text{if } k \text{ is even} \\ \frac{2}{\pi} \cdot \sum_{n \text{ even}} \frac{x_n}{k - n} & \text{if } k \text{ is odd} \end{cases}, \quad (5.8)$$

$$x_n = \begin{cases} -\frac{2}{\pi} \cdot \sum_{k \text{ odd}} \frac{y_k}{n - k} & \text{if } n \text{ is even} \\ -\frac{2}{\pi} \cdot \sum_{k \text{ even}} \frac{y_k}{n - k} & \text{if } n \text{ is odd} \end{cases}. \quad (5.9)$$

5.2 Polarization extraction

For every NMR measurement, two signals are measured. They both contain information about the polarization. The signals represent the absorption and dispersion spectra of the NMR response of the nuclei and will be designated as the X and Y channels, which are the name of the two signal outputs of the lock-in amplifier. Because every NMR measurement passes through the NMR resonance condition twice (down and up sweeps), each channel contains two polarization signals. Consequently, a total of four polarization signals can usually be extracted from a single NMR measurement.

5.2.1 Signal normalization

Because NMR measurements were sometimes taken with different settings, the signals need to be normalized in order to be compared to each other.

First, they are rescaled to take into account the different sweep rates and Data Acquisition (DAQ) rates¹. Indeed, a higher sweep rate will result in a narrower peak, thus a smaller area, as we pass through the resonance condition faster. A higher DAQ rate will result in more data points being taken, which can cause the peak area to appear bigger. The amplitude of the signal S is scaled, by multiplying it by the sweep rate and dividing it by the DAQ sampling rate, into a new signal S' as follows:

$$S' = \frac{\text{Sweep rate in G.s}^{-1}}{\text{DAQ rate in Hz}} \cdot S. \quad (5.10)$$

Between measurements, the Radio-Frequency (RF) power applied to the sample can be changed (e.g. to compensate for the polarization losses) or the response of the NMR circuit can vary (typically after the system has been moved). Thus, the signals need to be normalized to a reference signal. If the power (expressed in dBm²) of the signal, P_{run} , and the one of the reference signal, P_{ref} , are different, the amplitude of the signal is scaled as:

$$S'' = 10^{\frac{P_{ref}-P_{run}}{20}} \cdot S', \quad (5.11)$$

since the powers are expressed in dBm. If the response of the NMR circuit has changed between measurements, additional corrections have to be applied to compensate for them. Those changes can be due to modifications in RF transmission, signal gain or background gain. Fast resonance scans (see section 4.1.2) are taken in between measurements to help to detect and to correct such changes. Fortunately, this correction was unnecessary for the data used for this analysis, because the response of the NMR system was very stable. Indeed, in the case of such problem, a recalibration of the system using the thermal equilibrium of a CH₂ target of similar geometry to the HDice target may be necessary [62].

In the case of measurements done in the IBC, another scaling correction must also be applied if the main magnetic field has been rotated. Indeed, depending on the orientation of the magnetic field, the calibration of the NMR system appeared to be different. This is not yet understood why. The scaling factor to apply is determined by doing calibration measurements in both orientations.

¹Typical sweep rates are 300 G per 32.5 s (about 554 G/min) for automatic runs and 550 G/min for manual runs. Typical DAQ rates are 128 Hz and 256 Hz.

²dBm is the power ratio in decibels of the measured power referenced to one milliwatt.

5.2.2 Baseline correction

Sometimes NMR measurements show sudden background shifts that need to be corrected (see figure 5.3). Those shifts could often be traced to human activities around the NMR system with operations such as crane work or welding. The baseline is manually re-adjusted to make it more continuous. The shifts on both channels have to be corrected as much as possible, because bumps on the baseline can greatly affect further noise estimations or transformations. If the shift is very near or on the signal peak, we typically reject the measurement altogether, as another measurement has often been made in such a case.

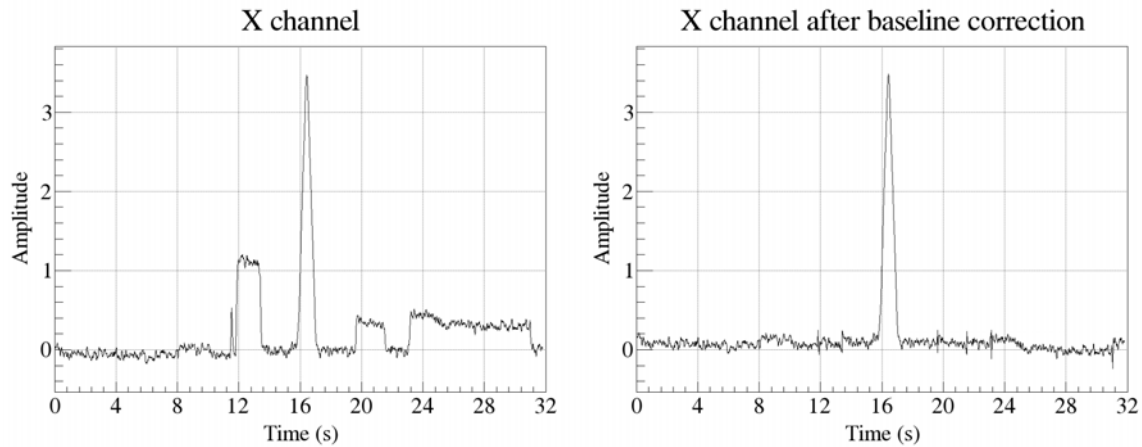


Figure 5.3: Correction of the baseline of an NMR signal (Lock-in X channel).

The baseline of each signal is also flattened and centered around zero by shifting and tilting the signal. In the case of manual operation, some runs present an exponential decay due to the fact the RF power did not have the time to settle after being turned on (see figure 5.4). They are easily corrected by subtracting the appropriate exponential decay line to the signal. The baseline must be centered around zero, because it makes transformation and integration of the peaks easier.

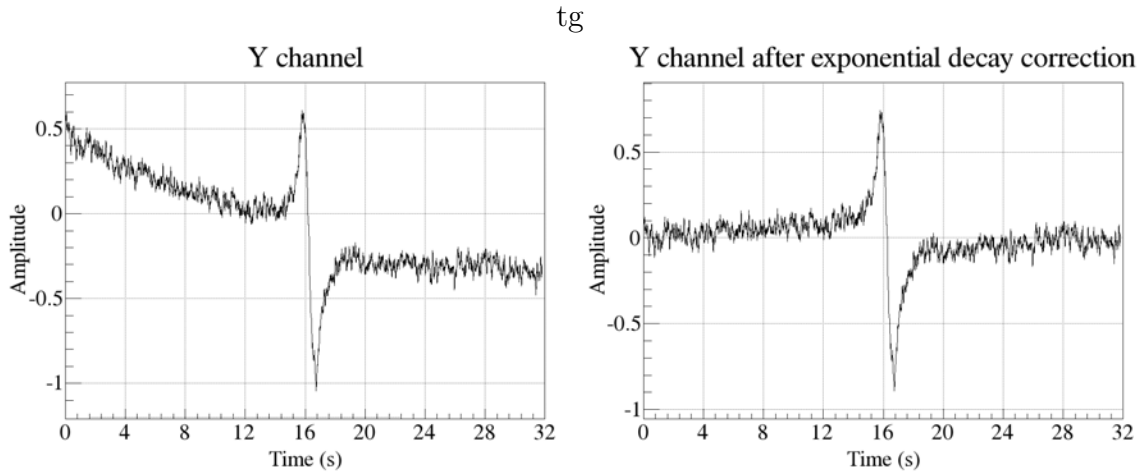


Figure 5.4: Correction of the exponential decay in an NMR signal (Lock-in Y channel).

If the noise-over-signal ratio is too large, a filter can be applied to improve the noise-to-signal ratio. By assuming the noise to be random and with faster variations than the NMR signal, a simple lowpass filter can be applied to the signal to remove those higher frequency variations. However, if such a filter is used, the same filter has to be applied to all of the considered signals including calibration signals, because it may affect the amplitude of the signal. Most of the measurements made during the electron runs were relatively clean, which has allowed us to skip this step.

5.2.3 Y channel signal transformation

Once the Y channel signal has been corrected following the procedures given in section 5.2.2, it is transformed using the Kramers-Kronig relations into a signal that can be treated like the X channel (see figure 5.5). Indeed, the peak of the X channel signal can simply be numerically integrated. The baseline of the transformed signal needs to be readjusted after this step to center it around zero.

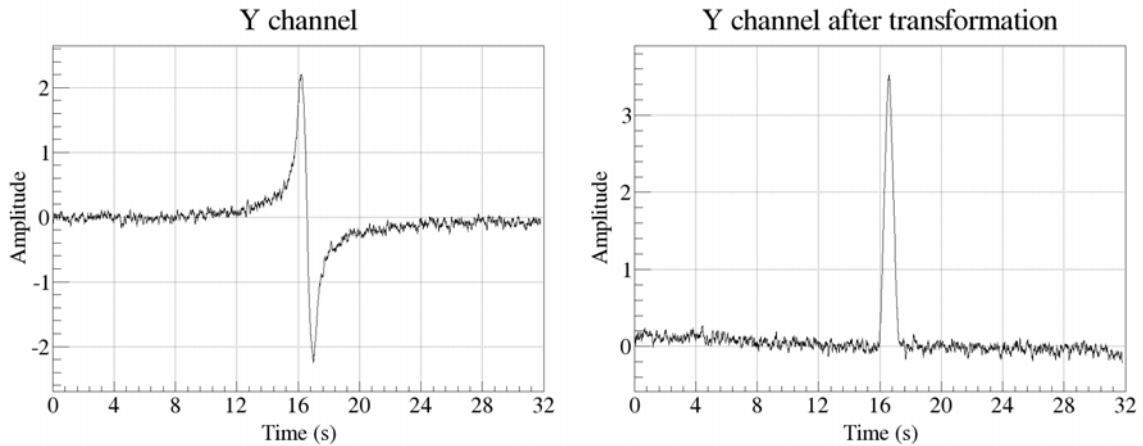


Figure 5.5: Transformation of a Y channel NMR signal.

Sudden background shifts must have been corrected before this step, especially the ones near the signal peak. Indeed, according to the Kramers-Kronig relations, a bump near the signal peak may affect the amplitude of the transformed signal.

5.2.4 Integration of the signal

Two methods can be used to obtain the area under the signal peak; numerical integration or fit of the signal. The first method has been chosen to compute the results of this analysis.

Indeed, the numerical integration is a reliable and fast way to extract the area by simply summing all the data point amplitudes in a given range. The range is chosen as small as possible around the signal peak to optimize the signal-to-noise ratio, as explained in the following section.

Performing a fit of the signal is also a good solution to obtain the area. It mostly is a matter of finding the appropriate function to fit the signal. Once the fit is made, the area and the uncertainty can be analytically computed with the parameters of the function. The advantage of the fit method is that the area is much less sensitive to the noise, but this comes with a price of additional systematic uncertainties (uncertainty on the fit functional form and uncertainty on the fit to the data itself). A Lorentzian

convoluted with a square function was shown to provide an adequate functional form for such fit [63].

5.2.5 Error estimation

By assuming the background on the edge of the signal is flat, centered around zero and that it is representative of the background at any time during the sweep, the uncertainty on one data point can be computed with the standard deviation of this background:

$$\sigma = \sqrt{\frac{1}{N} \cdot \sum_{i=0}^{N-1} (x_i - \mu)^2}, \quad (5.12)$$

where N is the number of points composing the background signal and μ is the average of those points, which should be zero.

Making the assumption that the error on each point is the same (the σ of equation 5.12), we can add in quadrature their error and compute the statistical error on the signal peak integral, ϵ :

$$\epsilon = \sqrt{n} \cdot \sigma, \quad (5.13)$$

where n is the number of points used to compute the sum (integration range), which depends on the magnetic field homogeneity, the sweep rate and the DAQ sampling rate, and does not fluctuate from one measurement to another. We can see that, while having a large integration range (large \sqrt{n}) guaranties that the full peak, including its tails (which are sometimes large due to magnetic field inhomogeneities), is accounted for, it also increases the error ϵ . Since the signal is small on the tail, a large \sqrt{n} deteriorates the signal-to-noise ratio.

If the signal edges at the start and end of the sweep are not perfectly flat, this method overestimates the error on the area. Thus, the error may appear slightly bigger than it really is.

5.3 Polarization results

Due to experimental constraints from Hall B and from the other halls' experimental programs:

- limited dedicated time (less than three weeks total);
- inadequate beam energy for elastic scattering polarimetry;
- low targets polarizations (less than 5% for H and 2% for D);
- unusual running conditions for Hall B (the sub nA beam current induced beam control issues, and the raster was inadequate for an HD target),

the electron tests have been performed in conditions far from ideal. The polarimetry monitoring by NMR was difficult and the alternate monitoring by elastic asymmetry (see section 1.2.4) was not possible. Unexpected depolarization processes made this situation worst. Thus it became a challenging task to understand the depolarization processes and the behavior of polarized HD under electron beams.

The first electron test was performed in difficult conditions with a total of 10 beam exposures spanned in 10 days. First, due to a technical issue with the NMR system, no monitoring of the polarization was possible during exposures until the last one. Then, due to miswired coils, the raster pattern was elliptical (instead of circular) for the first three exposures and the beam was even rastered over a larger area than the target during the second one. Usually, such a raster pattern problem is identified immediately from online monitoring of the scattering events (e.g. the vertex reconstruction of the events). However since, as previously mentioned, it was not useful to monitor the elastic (or any other) reactions, the CLAS DAQ was turned off. Measurements were done in many different configurations (beam current, raster size, magnetic field and temperature), which made difficult the identification of the polarization loss processes. This first set of tests was designed to search for permanent radiation damage effects (likewise ammonia targets, which cannot be polarized again after electron beam exposure) and their dependence upon the various parameters just listed; instead, unexpected beam-on loss mechanisms dominated. Finally, the proton polarization most likely reached its thermal equilibrium after the seventh beam exposure. The beam exposures (yellow areas on the figures 5.6 and 5.7) and

the different magnetic field and temperature conditions (separated by vertical lines on the figures) of this run are summarized in the tables 5.1 and 5.2. The figures 5.6 and 5.7 show the evolution of the proton and deuteron polarizations respectively. In each figure, the top and bottom panels show the polarization extracted from the X and Y channels respectively.

The second electron test was performed with two beam exposures spanning 3 days and show a much clearer dependency of the beam current intensity on the relaxation time of the target. Unlike the first test, the polarization could be monitored during the beam exposures. The first exposure was done with a beam current of 0.1 nA and the proton relaxation time was about 30h, while the current for the second one was 1 nA and the apparent proton relaxation time was less than 3 hours. At the end of the test, both proton and deuteron polarizations were set to zero and monitored while growing back to their Thermal Equilibrium (TE). The proton polarization grew back to only half of the expected TE value, while no visible growth was evidenced for the deuteron polarization. This could suggest the proton recovered within a few hours (during which their polarization grew) its frozen spin mode, while the deuteron stayed in such a mode, although the polarization loss for the deuteron appears higher than the proton one. The beam exposures (yellow areas on the figures 5.8 and 5.9) and the different magnetic field and temperature conditions (separated by vertical lines on the figures) of this run are summarized in the tables 5.3 and 5.4. The figures 5.8 and 5.9 show the evolution of the proton and deuteron polarizations respectively. The sudden polarization changes that occurred on day 14 were due to the spin transfer between H and D (with a limited efficiency due to the low polarizations). Unfortunately, for an unknown reason, the Y channel data during the second exposition were corrupted and could not be used.

Although those tests do not allow a complete understanding of the behavior of HD under an electron beam, they point to multiple explanations for the polarization loss mechanisms: immediate polarization loss, transient depolarization due to ionization of the HD and recombination with electrons of the surrounding material (most likely the aluminum wires), dependency of the relaxation time with the magnetic field and temperature, and a generally complicated parameter space (possible time dependency of the combination of different effects, such as permanent damages and beam characteristics and quality). The tests also show that the heat load on the target was a problem. The raster used for the tests was designed for DNP-type target, but was too slow to spread the beam heat evenly through the HDice-type target, which created local heating. Another issue was that the heat could not be

dissipated efficiently because the aluminum wires were too long (the heat conduction was limited and dominated by the relatively high aluminum heat resistivity at very low temperature). More completed analyses of those tests are given in [64] and [65].

The tests also suggest a possible “screening” of the RF field during NMR measurement due to the ionization of the HD. Indeed, after the first irradiation of the first test period (figure 5.6), there is an initial polarization loss, then followed by an apparent growth. Furthermore, during the second irradiation of the second test period where the beam was fairly constant at 1 nA throughout, the data could indicate a sudden drop in polarization followed by a slowing down in the polarization loss rate, hence an increase in T1 (figures 5.8 and 5.9). However, no physical mechanism can cause such an increase in the T1s. Both of those unusual observations could be explained by partial screening of the NMR by free electrons, probably from Moller scattering which produces huge numbers of very low energy electrons. Some fraction of the Moller electrons enter the conduction band of HD and screen the RF in a way similar to a metal. This is counteracted by neutralization from the aluminum wires, with the net effect that the screening isn’t complete but rather reaches an equilibrium (in about a few hours). Thus, while polarization losses were definitely observed, the apparent losses according to the NMR could be larger than the actual loss. A way to determine the impact of this screening on the NMR measurements would have been to extract the target polarization by another mean, such as the electron scattering. Unfortunately, as already stated, the target polarization was too low, as was the beam energy, to perform such an analysis. We remark that given the fast depolarization processes, polarization monitoring by elastic scattering must be done with low beam energy (this depends on the target polarization, but typically 1 GeV or lower), so that the time needed to gather statistically significant data is shorter than the characteristic depolarization or screening process time.

To conclude, those tests do not permit to prove or to disprove the validity of the usage of an HD target under an electron beam. Thus, further tests are required to understand the behavior of the HD under electron beams. In the future, such tests should be performed with a target more adapted to the electron beam (faster raster, shorter target with a bigger diameter), which could improve considerably the performance of the target with electrons.

	Current	Charge	Comments
A	0.1-0.5 nA	16 nA.min	10 mm x 4 mm raster
B	0.1-0.5 nA	60.2 nA.min	20 mm x 8 mm raster
C			unsuccessful attempt
D	1 nA	64.9 nA.min	5 mm radius raster
E	1 nA	455.7 nA.min	5 mm radius raster (4h badly misteered)
F	1 nA	541 nA.min	6.5 mm radius raster
G	0.25 nA	66.4 nA.min	5 mm radius raster
H	0.25 nA	13.3 nA.min	5 mm radius raster
I	0.25 nA	132 nA.min	2.5 mm radius raster
J	0.25 nA	45 nA.min	5.5 mm, then 5 mm radius raster (large beam tails)

Table 5.1: Beam exposures of the target during the first electron test period.

	Field	Temp.		Field	Temp.
1	0.85 T	80 mK	18	0.3 T	80 mK
2	0.3 T	80 mK	19	0.7 T	80 mK
3	0.5 T	80 mK	20	0.85 T	80 mK
4	0.5 T	160 mK	21	0.5 T	80 mK
5	0.5 T	240 mK	22	0.5 T	80 mK
6	0.3 T	240 mK	23	0.7 T	80 mK
7	0.85 T	80 mK	24	0.85 T	80 mK
8	0.5 T	80 mK	25	0.5 T	80 mK
9	0.5 T	160 mK	26	0.28 T	80 mK
10	0.3 T	80 mK	27	0.28 T	80 mK
11	0.3 T	160 mK	28	0.28 T	160 mK
12	0.3 T	240 mK	29	0.28 T	240 mK
13	0.85 T	80 mK	30	0.85 T	80 mK
14	0.3 T	160 mK	31	Field Rotation	
15	0.85 T	80 mK	32	-0.28 T	80 mK
16	0.5 T	80 mK	33	-0.28 T	160 mK
17	0.4 T	80 mK	34	-0.28 T	80 mK

Table 5.2: Magnetic field and temperature conditions of NMR measurements taken in between electron exposures during the first electron test period.

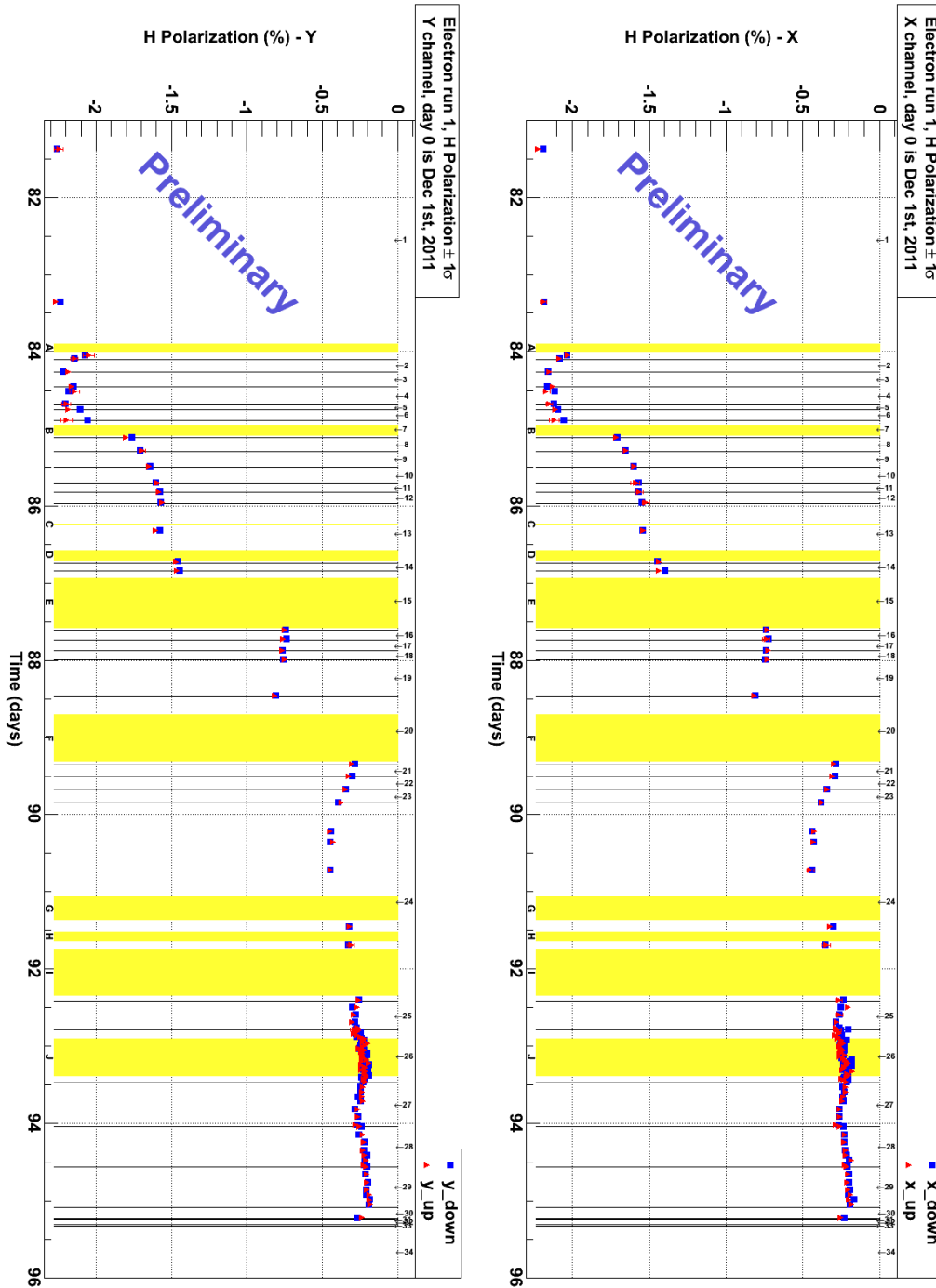


Figure 5.6: HDice target polarization for H from NMR measurements during the first electron run. The yellow areas represent the periods of exposure of the target to the electron beam.

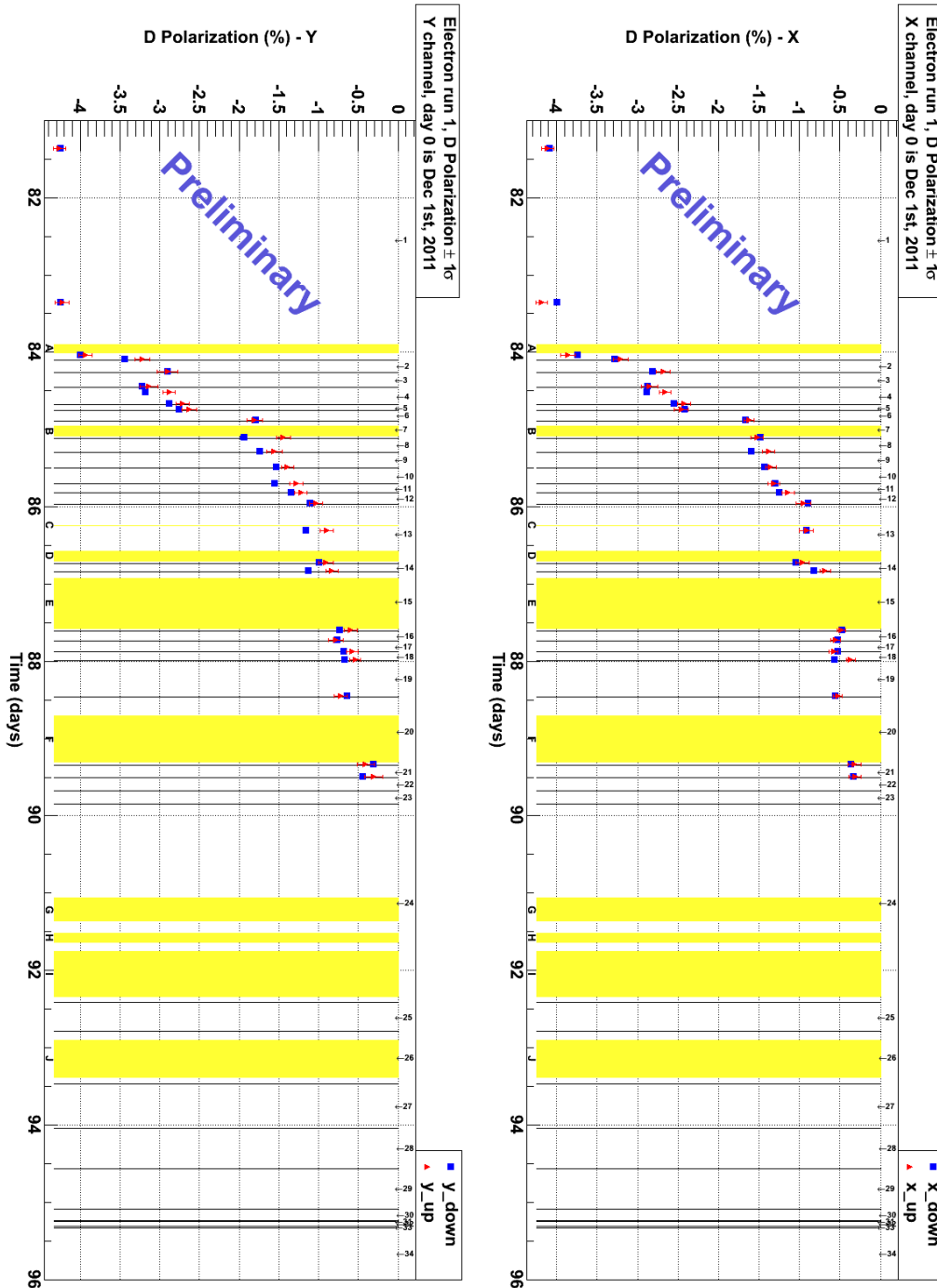


Figure 5.7: Idem as figure 5.6 but for D.

	Current	Charge	Comments
A	0.01-0.1 nA	28 nA.min	3 mm radius raster 0.1 nA (first 3 hours)
B	0.1-1 nA	800 nA.min	6.5 mm radius raster

Table 5.3: Beam exposures of the target during the second electron test period.

	Field	Temp.
1	0.9T	80mK
2	0.5T	80mK
3	0.9T	80mK
4	Spin transfer H \leftrightarrow D	
5	0.9T	80mK
6	0.28T	80mK
7	800G incident	
8	0.28T	80mK
9	0.9T	80mK
10	0.28T	80mK
11	Polarization erased	
12	0.28T	80mK

Table 5.4: Magnetic field and temperature conditions of NMR measurements taken in between electron exposures during the second electron test period.

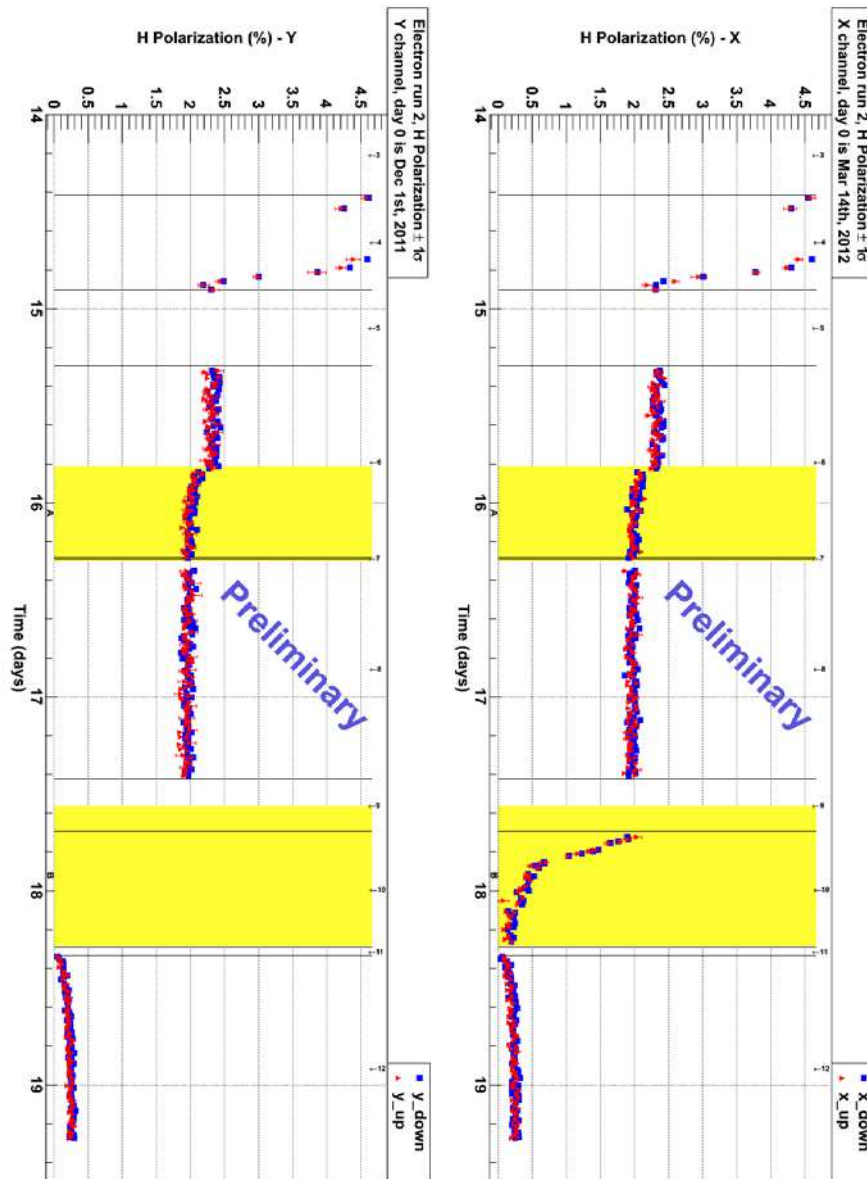


Figure 5.8: HDice target polarization for H from NMR measurements during the second electron run. The yellow areas represent the periods of exposure of the target to the electron beam.

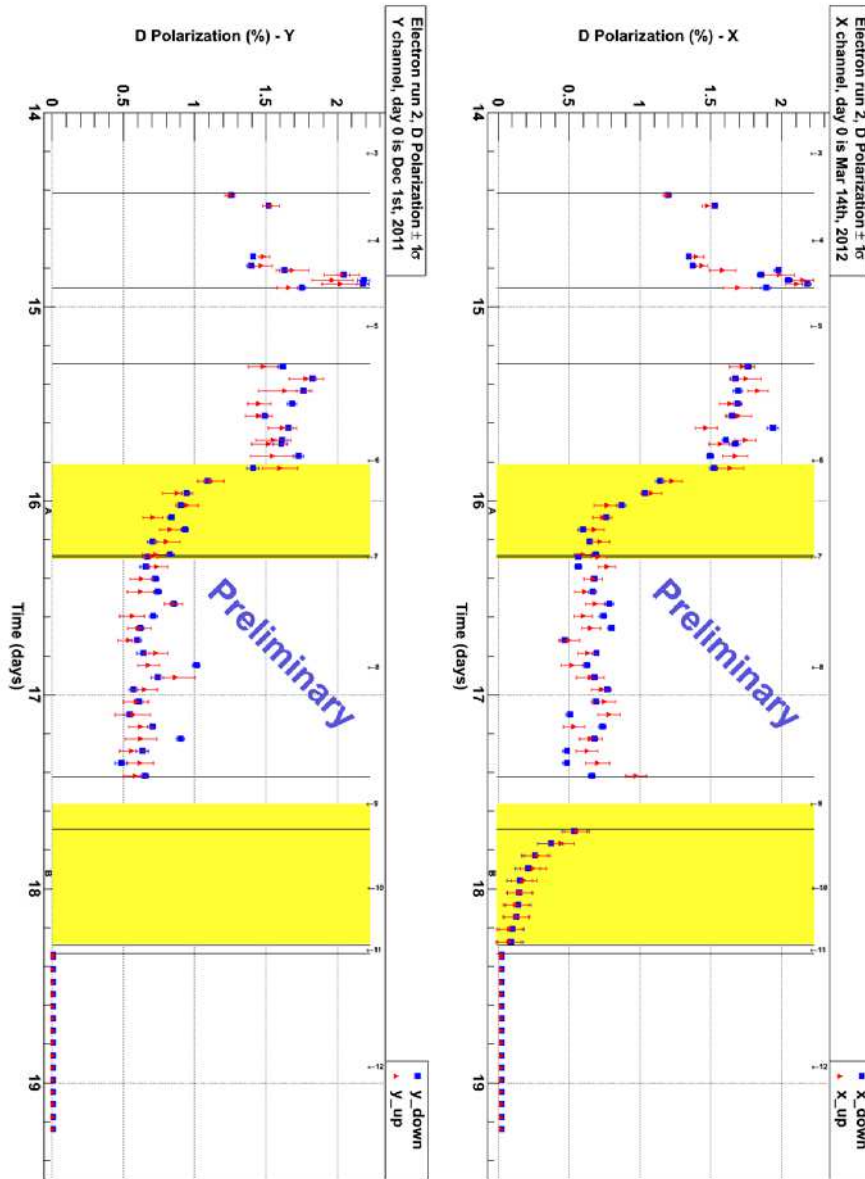


Figure 5.9: Idem as figure 5.8 but for D.

Chapter 6

Polarimetry with electron scattering

The initial purpose of the analysis presented in this chapter was to gather experience on the analysis of elastic scattering for polarimetry for the HD target electron test runs discussed in Chapter 5. However, as said earlier, the target polarizations during the HD target electron test runs during the g14 experiment were insufficient to perform the same kind of analysis discussed in this chapter.

During the Hall A E97-110 experiment, a helium-3 was used. The polarimetry of the target was performed by Nuclear Magnetic Resonance (NMR) and Electron Paramagnetic Resonance (EPR) (see section 1.2.3) measurements. However, an uncertainty about the polarimetry remains as those measurements show a discrepancy.

It was therefore important to determine which of those measurements was the most reliable by comparing them with the polarimetry obtaining using a well known physics reaction; the elastic scattering of electron on ^3He .

6.1 Experiment details

All the data used for this analysis were taken during the E97-110 experiment that ran in 2003 in Hall A [66]. The experiment consisted of scattering polarized electrons on a polarized ^3He gas target (see figure 6.1). The scattered electrons were detected by the right High Resolution Spectrometer (HRS) [67], which allows to detect charged particles and reconstruct the interaction vertices from their trajectories. The right HRS was set-up to detect nominally the electrons (inclusive experiment), while the left HRS was used as a luminosity monitoring device.

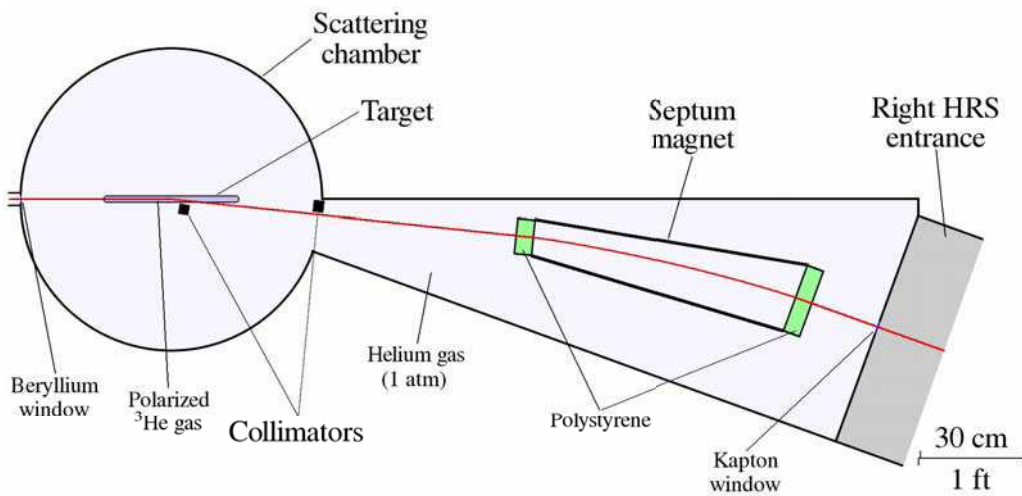


Figure 6.1: Schematic of the E97-110 experimental setup (target area).

The goal of this experiment was to perform a precise measurement of the inclusive polarized cross sections for electron scattering from the ^3He target at low momentum transfers. In order to obtain the generalized GDH sum rule at low Q^2 . As discussed in the introduction, this is another approach to understand non-perturbative QCD, because the GDH sum rule is a quantity defined and calculable at any Q^2 value [66]. Because of the small angles of the scattered electrons of 6° and 9° , a “Septum” magnet (small dipole magnet) was inserted between the target and the HRS to steer the scattered electrons to the HRS (otherwise, the minimal detection angle of the HRS pair is 15°). Two collimators were used to block electrons scattered by the target cell windows, which could contaminate events of interest and limit the statistics by saturating the DAQ.

The elastic scattering data used for this analysis were taken with a 4mm by 4mm raster pattern, and with four different settings (beam energy and scattering angle) : 2.1 GeV at 6°, 2.8 GeV at 6°, 1.1 GeV at 9° and 2.2 GeV at 9°. For each setting, alongside the polarized ^3He runs, a nitrogen reference cell run and an empty reference cell run were performed to determine the nitrogen background contribution.

The polarization of the target was monitored every 4-6 hours with NMR and/or EPR measurements. The NMR polarimetry was calibrated with two different methods; the first one used the NMR TE measurement (see section 1.2.2) of a water cell of similar geometry to the ^3He target cell with the water's hydrogen at thermal equilibrium, and the other one used the EPR measurement (see section 1.2.3).

6.2 Polarization extraction

The target polarization, P_t , can be estimated by computing the physics asymmetry, A_{exp} , (see section 1.1.1.2) of the elastic scattering reaction through simulations and by calculating the raw experimental asymmetry, A_{raw} , from the experimental data taken during the experiment. Those asymmetries are related by:

$$A_{exp} = \pm \frac{A_{raw}}{fP_tP_b}, \quad (6.1)$$

where f is the dilution factor due to the background. Those are events coming from electron scattering of nitrogen gas in the target cell and from the material surrounding the cell, such as the beam pipe and cell windows. P_b is the beam polarization (longitudinal). The sign of the equation depends on whether the target and beam polarizations are parallel or anti-parallel. The dilution factor is calculated from the nitrogen reference cell runs and the beam polarization is measured by the Møller and/or Compton polarimeters [67] of Hall A.

6.2.1 Simulation

The simulation code generates scattering events in the configuration of the experiment.

The original code was a Fortran 77 version written by Alexandre Deur [68]. However, for a better personal understanding of the code, the code was rewritten in C++. The main change between the two versions is in the way the energy losses are handled, although they remain equivalent. The C++ version computes the energy losses for each individual material region the electrons pass through (beryllium window, helium gas, target cell entrance window...) rather than an average of those materials used in the Fortran version. The goal was to be able to introduce subtle changes in the materials composition with ease. However, further work is still required, because ionization losses still slightly underestimate the energy losses by about 10% (depending on the material) and have to be corrected. Nonetheless, the impact is limited, because energy losses for these simulations are usually dominated by Bremsstrahlung losses.

The code first generates the interaction vertex inside the target and the direction and (correlated for the elastic reaction) momentum of the scattered electron. Then, it computes the position of the charged particle (here electron) before and after the various magnetic elements of the HRS. Those positions were initially obtained by a ray-tracing simulation code (SNAKE [69]) that generated many trajectories through the magnetic elements. The SNAKE results were then fitted and the fit functions used in our simulation. In addition, our code accounts for multiple scattering and energy losses (ionization and Bremsstrahlung) of the electron through the different materials. It also checks if the electron hits the aperture of the components making the HRS (mostly magnet apertures) and only stores events (weighted by the cross section in the elastic case) that reach the HRS focal plane.

Finally, by counting the number of events in the acceptance defined by the cuts used in the analysis of the experimental data, the code can predict the physics asymmetry and total cross section at the conditions (beam energy, angle, etc) specified by the user. The predicted asymmetry and cross section account intrinsically for the acceptance. Thus, they can be directly compared to the raw experimental ones to extract the target polarization.

6.2.2 Data selection and polarization calculation

The selection of the data is made by applying some cuts on the measured and simulated events, which are stored into root files. The cuts applied on the experimental

data for the calculation of asymmetries are:

- Single track cut; because a small fraction of the recorded events contain the detection of more than one electron, those events are ignored because their vertices and angles are often misreconstructed.
- Collimators cuts; a set of two-dimensional cuts on y_{tg} and ϕ_{tg} shown on figure 6.2, which exclude events in a region where the electrons should have been stopped by the collimators. This cut is necessary because the electrons may have been scattered by the edges of the collimators and this effect is not taken into account by the simulation.
- Particle IDentification (PID) cuts; which enable to remove the majority of the pion events.
- Kinematic cuts; which restrict the kinematics to the acceptance of the simulation. The kinematic cuts for the asymmetry calculations are applied to δ , ϕ_{tg} , θ_{tg} , y_{tg} and W and are listed in table 6.1. δ is defined as:

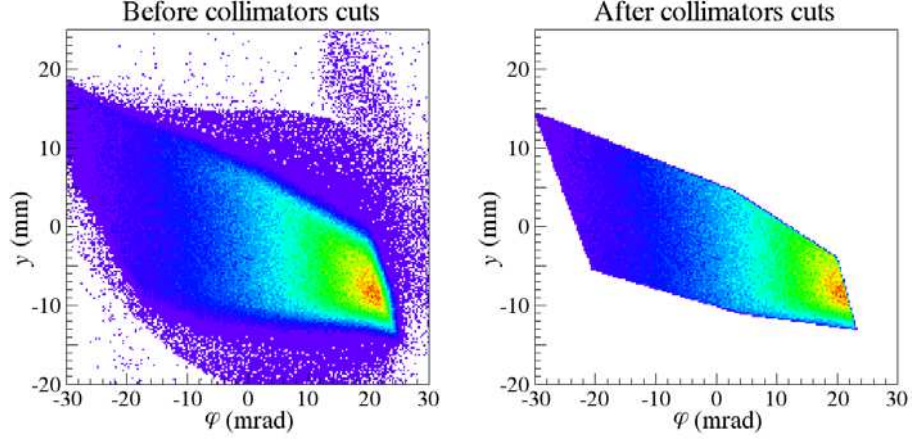
$$\delta = \frac{P - P_0}{P_0}, \quad (6.2)$$

where P is the measured particle momentum and P_0 is the spectrometer central momentum. ϕ_{tg} , θ_{tg} and y_{tg} are the reconstructed event vertex angles and y position, shown on figure 6.3. W is the invariant mass of the residual hadronic system (see section 1.1.1.1). Figure 6.4 shows a good agreement for most of the simulated and measured kinematics histograms.

During the selection of the events, the beam helicity relative to the event is also checked and the event is registered in the corresponding counter (N^+ or N^-). This allows to compute the raw asymmetry A^{raw} of those events:

$$A^{raw} = \frac{\frac{N^+}{LT^+Q^+} - \frac{N^-}{LT^-Q^-}}{\frac{N^+}{LT^+Q^+} + \frac{N^-}{LT^-Q^-}}, \quad (6.3)$$

where N^\pm is the number of events, $(1 - LT^\pm)$ the deadtime, due to acquisition and electronics, associated with the events recorded in the right HRS spectrometer, and Q^\pm the total accumulated charge for each beam helicity state.


 Figure 6.2: y_{tg} VS ϕ_{tg} before and after collimators cuts for run 2441 (6° , 2.1GeV).

Angle	Energy	Cuts
6°	2.1 GeV	$0.007 < \delta < 0.001$ $1.2\text{MeV} < W < 4.5\text{MeV}$
6°	2.8 GeV	$0.009 < \delta < 0.001$ $5.0\text{MeV} < W < 1.5\text{MeV}$
9°	1.1 GeV	$0.006 < \delta < 0.002$ $2.5\text{MeV} < W < 1.0\text{MeV}$
9°	2.2 GeV	$0.021 < \delta < 0.013$ $4.0\text{MeV} < W < 0.5\text{MeV}$
All		$18\text{mrad} < \phi_{tg} < 18\text{mrad}$ $40\text{mrad} < \theta_{tg} < 40\text{mrad}$ $10\text{mm} < y_{tg} < 4\text{mm}$

Table 6.1: Kinematic cuts for the asymmetry calculations.

Finally, the target polarization P_t is computed from this asymmetry, according to equation 6.3, as:

$$P_t = \pm \frac{A^{raw}}{f P_b A^{exp}}. \quad (6.4)$$

The dilution factor is given by:

$$f = 1 - \frac{Y_{N_2}}{Y_{He}} \frac{Y_{empty}}{\rho_{N_2}^{N_2}} \frac{\rho_{He}^{N_2}}{Y_{He}}, \quad (6.5)$$

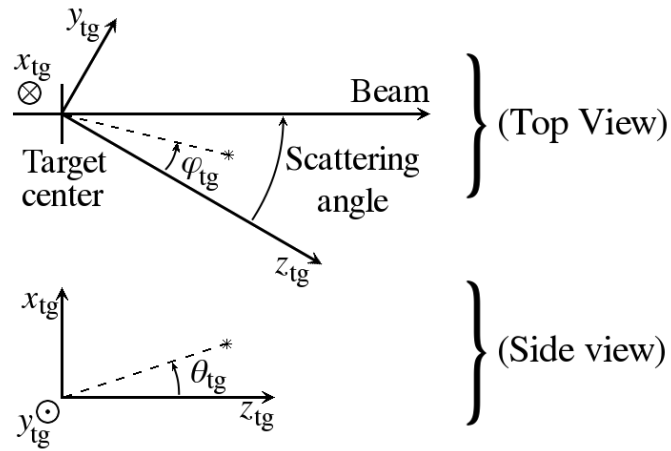


Figure 6.3: Target coordinate in the Hall A HRS system.

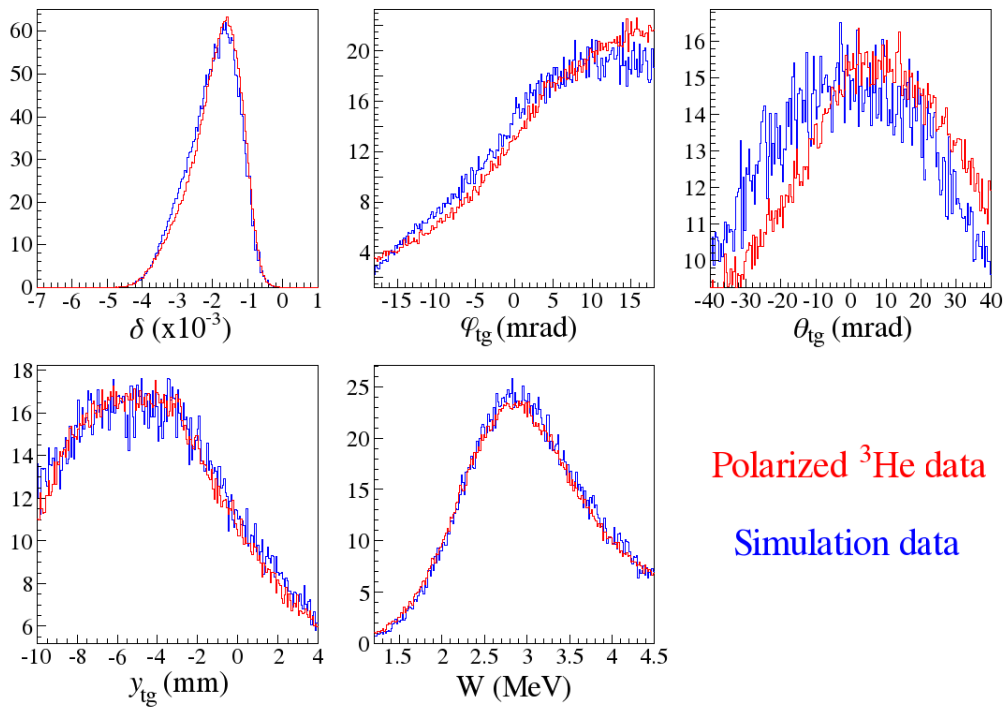


Figure 6.4: Comparison between experimental and simulated data for kinematics variables with asymmetry cuts for run 2441 (6° , 2.1GeV).

where $\rho_{^3\text{He}}^{\text{N}_2}$ is the density of the nitrogen during polarized ^3He data runs (mixed with the ^3He gas) and $\rho_{\text{N}_2}^{\text{N}_2}$ is the density of the nitrogen during nitrogen reference cell runs (pure nitrogen gas). Y_{N_2} , Y_{empty} and $Y_{^3\text{He}}$ are, respectively, the yields from the nitrogen reference cell, empty reference cell and polarized ^3He runs, which are calculated by:

$$Y = \frac{ps_1 \cdot N}{Q \cdot LT \cdot \epsilon_{det}}, \quad (6.6)$$

where N is the number of events after cuts (same for all runs), ps_1 is the prescale factor of the trigger and ϵ_{det} is the overall detector efficiency from all the detectors.

6.3 Polarization results

The extracted target polarizations from the four different settings are shown in figures 6.5, 6.6, 6.7 and 6.8. The ratios of the average extracted polarization to the NMR (or EPR) polarization for each setting are plotted on figure 6.9.

The error bars only represent the statistical error on the data and were scaled according to the “unbiased estimate” (therefore, all χ^2 are equal to 1).

It appears from this analysis that the polarizations from the EPR and NMR calibrated with EPR are always closer to the ones extracted from the asymmetries than the polarizations from the NMR calibrated with the water cell. This suggest the EPR polarizations are reliable and that the NMR polarizations are more reliable if calibrated with the EPR.

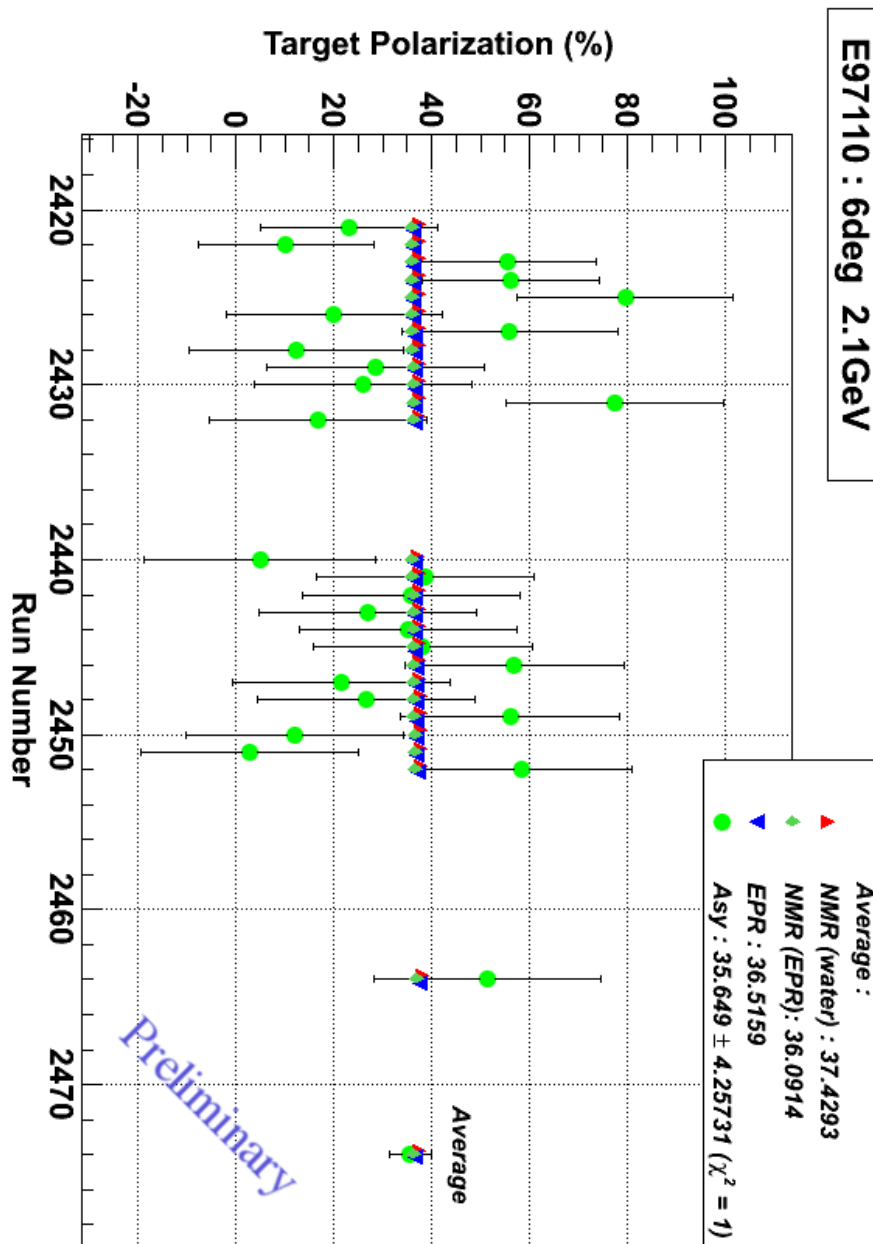


Figure 6.5: Hall A ^3He experiment E97-110 polarizations from asymmetries at 6° and 2.1 GeV.

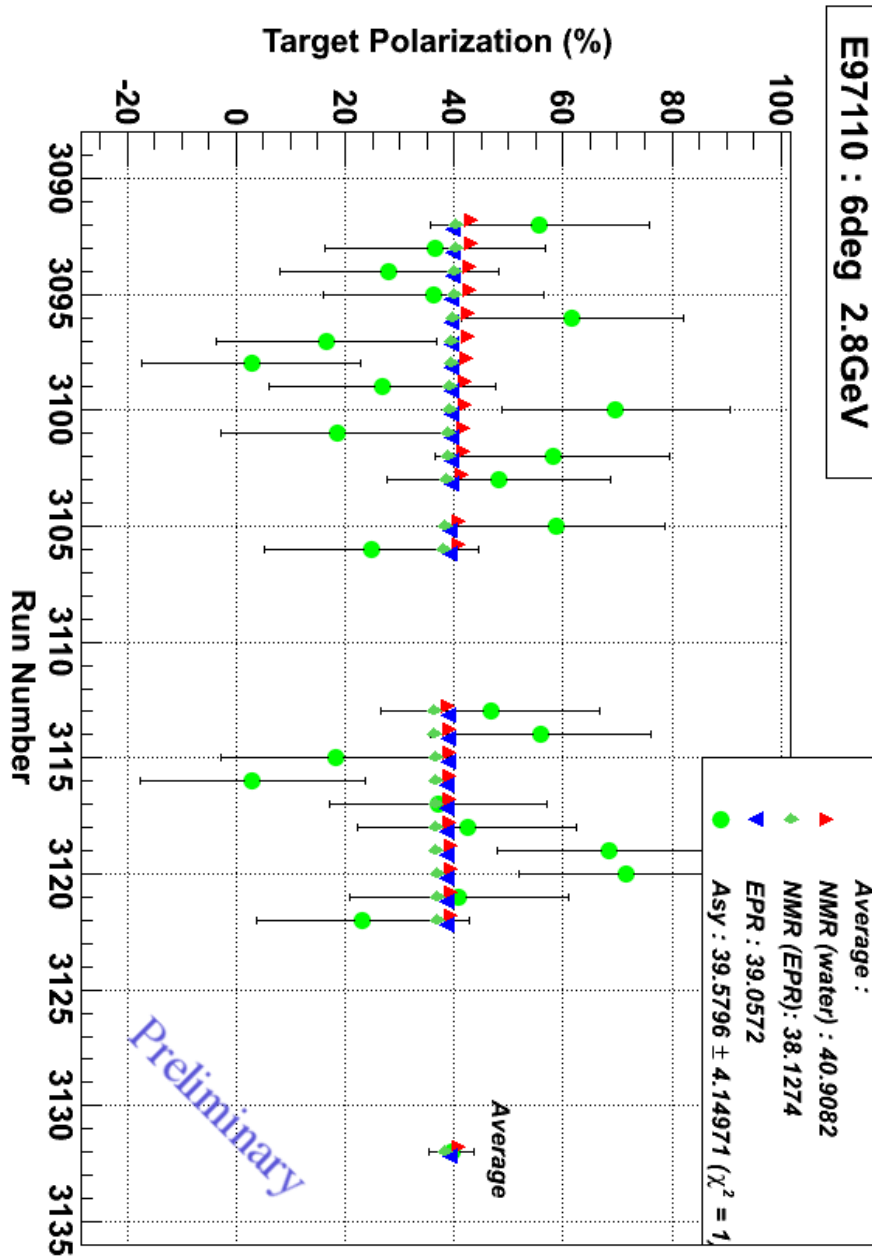


Figure 6.6: Hall A ^3He experiment E97-110 polarizations from asymmetries at 6° and 2.8 GeV.

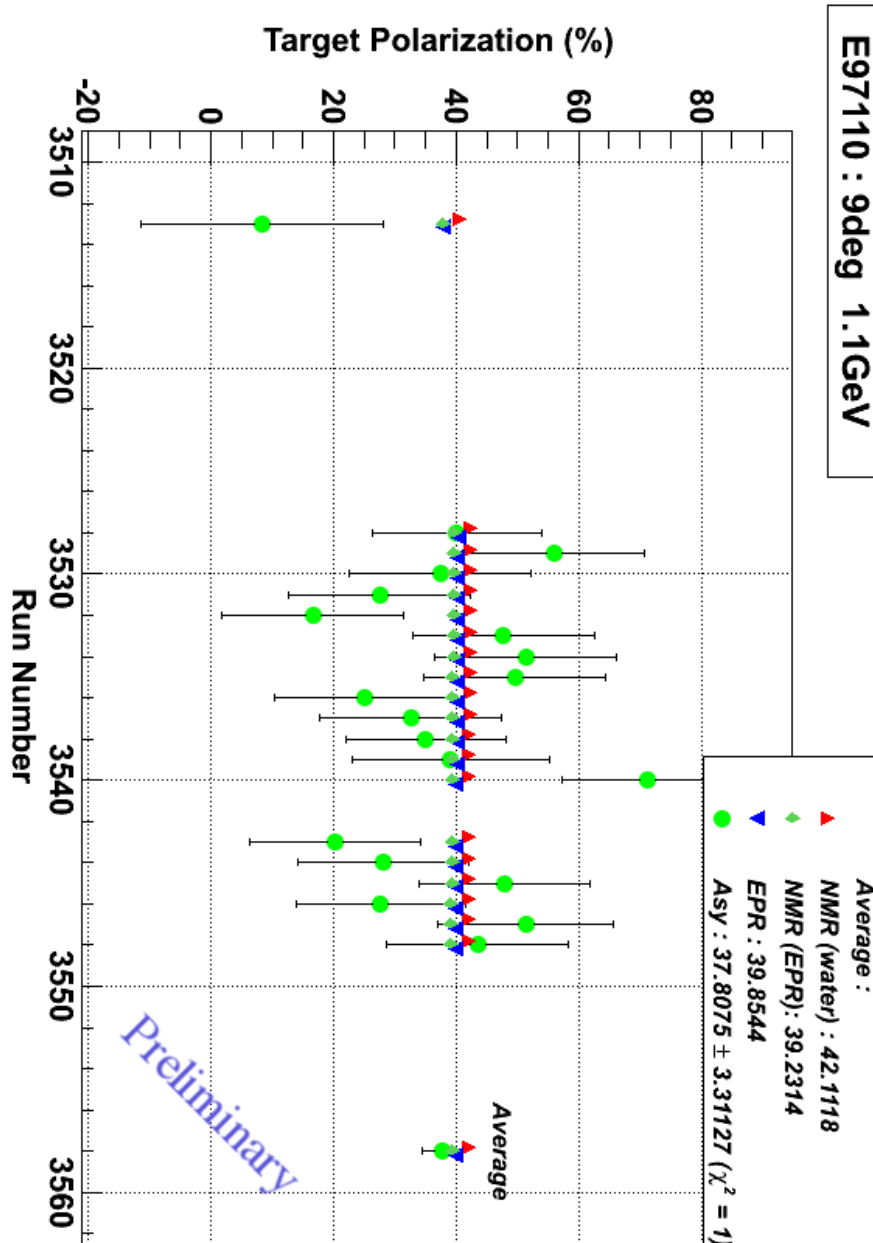


Figure 6.7: Hall A ^3He experiment E97-110 polarizations from asymmetries at 9° and 1.1 GeV.

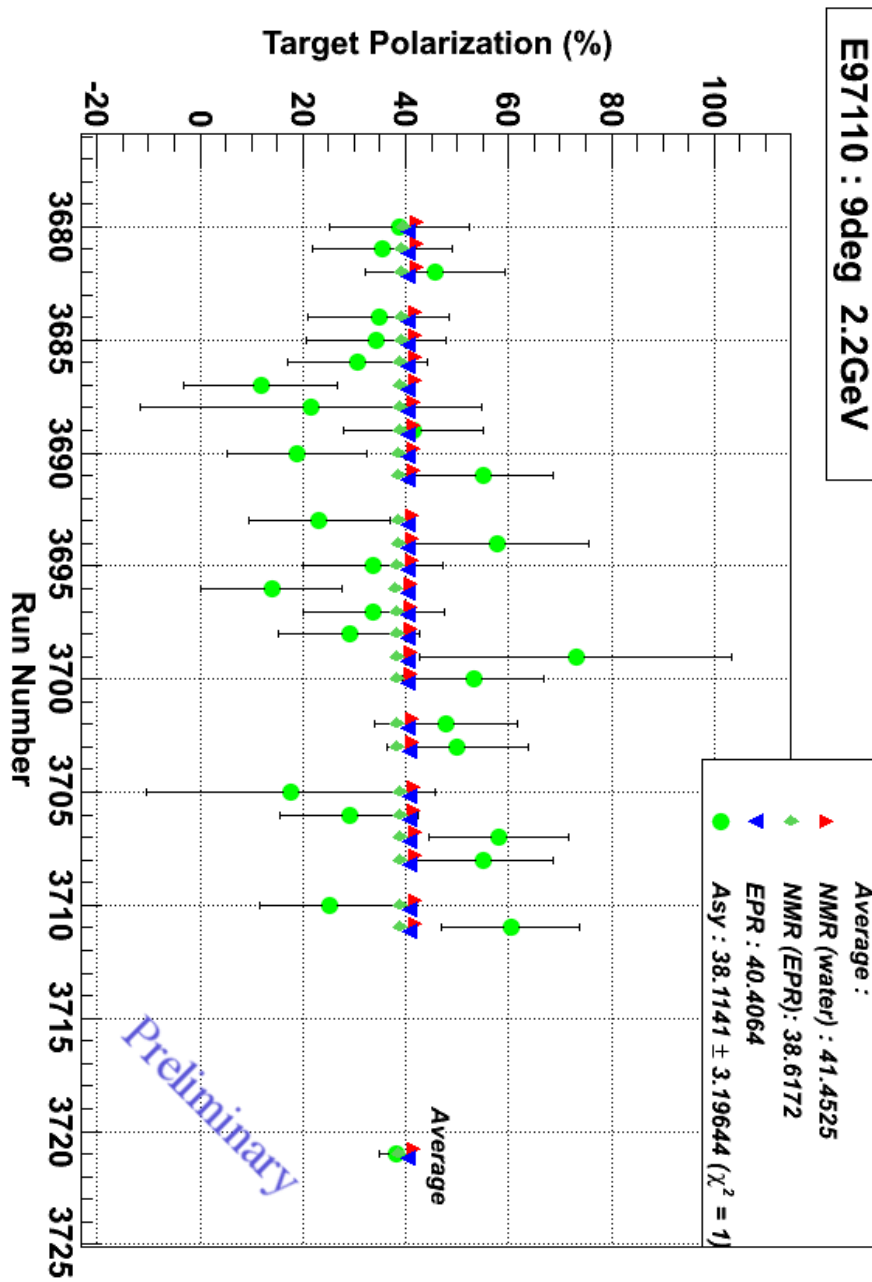


Figure 6.8: Hall A ^3He experiment E97-110 polarizations from asymmetries at 9° and 2.2 GeV.

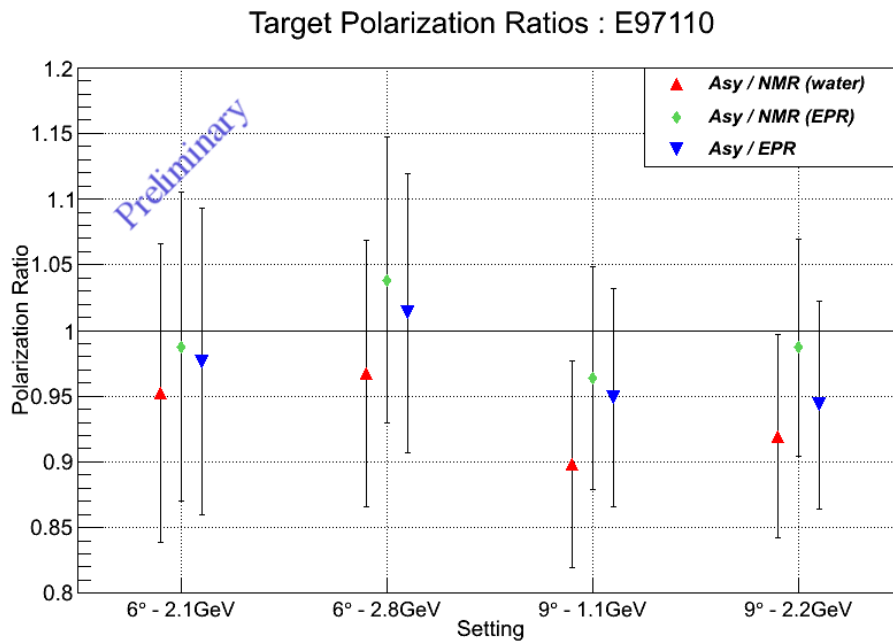


Figure 6.9: E97-110 polarizations ratios formed with the polarization extracted from the elastic reaction over the NMR or EPR results.

Conclusions

In this dissertation, we have presented advances in polarized targets in the context of experiments seeking a better understanding of the strong nuclear force and the fundamental structure of ordinary matter. We have described the principles and usage procedures for HD targets, and the improvements required to suit the experimental program using photon beams in Jefferson Lab's Hall B. Among the modifications and improvements of the HD target used in JLab, compared to the one used at LEGS, was the careful design and first use in nuclear physics experiment of birdcage-type coils for NMR and particularly HD spin operations. This new design allowed to reduce both spin operation time and polarization losses. Then, we have discussed the technical aspect of polarimetry of the HD target, as well as the method to monitor the evolution of its polarization during the two electron beam test runs. Finally, we have described another approach to determine the polarization of a target by using the elastic scattering reaction.

During the g14 experiment, the HD target was successfully used under a photon beam, providing highly polarized hydrogen (up to $\sim 50\%$) and deuterium (up to $\sim 30\%$ after spin transfer) nuclei with little dilution compared to other polarized cryogenic targets. The data taken during this experiment will help to study the excited nucleon spectrum, especially the "missing resonances" predicted by the Constituent Quark Model but yet unobserved. To complete those data, extensions of the g14 experiment could still be run during the 12 GeV era of Hall B (although its current program is focused on electron scattering) or in the new JLab Hall D, which is dedicated to photon beam experiments.

As a central part of this thesis work, we discussed in details the NMR polarimetry for HD and its off-line analysis procedure for the data taken while the HD target was tested under a low current (0.1-1 nA) electron beam. The test showed that, in the

given conditions, neither H nor D could retain their polarization. It appears that the heat deposited by the electron beam was not spread fast enough due to an inadequate raster speed. This warmed up locally the target and dramatically decreased the relaxation time, causing depolarization. In addition, other depolarization processes seem to be at work, possibly due to the ionization of HD via the Moller reaction. A faster raster and a new target design (shorter target length with an increased diameter) are under study. Those improvements should allow to keep the local heating of the target under control and to cleanly test the different depolarization processes. The new tests will take place either in Hall B or, most likely, in the small beam gun test facility that is presently being set-up in the Test Lab of Jefferson Lab. This low energy electron beam (planned to reach several tens of MeV) is adequate for HD testing. It also has the practical advantages to have more easily available beam time than for an experimental Hall, and to be closer to the HD target lab where the targets are polarized. This would greatly simplify the target transport. This should allow to complete the systematic studies of HD behavior under an electron beam. If the HD target was proven to be adequate for electron beam experiments, it could be used in Hall B for different key 12 GeV experimental programs: measurements of the Generalized Parton Distributions (GPD) of the nucleon using transverse Deep Virtual Compton Scattering (DVCS) [70], or study of transversity -the role of the transverse spin of the quarks in the spin structure of the nucleon- using Semi-Inclusive DIS (SIDIS) [71].

Finally, we discussed another mean of polarimetry. It takes advantage of well-known reactions (here elastic scattering) to extract the product of beam and target polarizations. Although it would have been very valuable, this technique could not be used for the HD electron tests due to the low polarization of the HD targets (highly polarized targets were used in priority for the g14 experiment) and constraints from other experimental halls. Nevertheless, the method was applied to Hall A polarized ^3He data for which the two standard polarimetries, NMR and EPR, disagreed. The elastic analysis favors the EPR data, as well as the NMR data calibrated with the EPR. This is compatible with the expectation that the NMR analysis had some systematic issues because of the large magnetic field gradients that were present during the experiment. The ^3He target will continue to be used extensively in Hall A for the 12 GeV program [72] [73] [74] [75] [76] and will also be used for the first time in Hall C [77]. The experiments will take place in the DIS regime and aim to better understand the longitudinal and transverse spin structure of the neutron, in a complementary program to the Hall B polarized target one.

Appendix A

Acronyms list

AdS Anti-de Sitter

AFP Adiabatic Fast Passage

AGS Alternating Gradient Synchrotron

BNL Brookhaven National Laboratory

BPM Beam Position Monitor

CC Čerenkov Counter

CEBAF Continuous Electron Beam Accelerator Facility

CFT Conformal Field Theory

CLAS CEBAF Large Acceptance Spectrometer

CQM Constituent Quark Model

D Deuterium or Deuteron

APPENDIX A. ACRONYMS LIST

DAQ Data AcQuisition
DC Drift Chamber
DF Dilution Fridge
DFT Discrete Fourier Transform
DIS Deep Inelastic Scattering
DNP Dynamic Nuclear Polarization
DVCS Deep Virtual Compton Scattering
EC Electromagnetic Calorimeter
EPR Electron Paramagnetic Resonance
FAFP Forbidden Adiabatic Fast Passage
FROST FROzen Spin Target
FRS Fast Resonance Scan
FT Fourier Transform
GaAs Gallium Arsenide
GDH Gerasimov-Drell-Hearn
GPD Generalized Parton Distributions
H Hydrogen or proton
HD Hydrogen Deuteride
He Helium

APPENDIX A. ACRONYMS LIST

HRS High Resolution Spectrometer

IBC In-Beam Cryostat

JLab Jefferson Lab (also known as TJNAF)

LHC Large Hadron Collider

LINAC LINear ACcelerator

NMR Nuclear Magnetic Resonance

PD Production Dewar

PID Particle IDentification

PMT Photo-Multiplier Tube

PWA Partial Wave Analysis

QCD Quantum ChromoDynamics

Rb Rubidium

RF Radio Frequency

RGA Residual Gas Analyzer

SD Storage Dewar

SFP Saturated Fast Passage

SIDIS Semi-Inclusive DIS

SNR Signal-to-Noise Ratio

SRF Superconducting Radio Frequency

APPENDIX A. ACRONYMS LIST

TC Transfer Cryostat

TE Thermal Equilibrium

TJNAF Thomas Jefferson National Accelerator Facility

TOF Time-Of-Flight

VI Virtual Instrument

References

- [1] The ATLAS Collaboration. *A particle consistent with the Higgs boson observed with the ATLAS detector at the Large Hadron Collider*. *Science*, **338**(6114):1576–1582, 2012.
- [2] D.J. Griffiths. *Introduction to quantum mechanics*. Pearson Prentice Hall, 2005.
- [3] N. Brambilla and A. Vairo. *Quark confinement and the hadron spectrum*. 13th annual Hampton university graduate studies at the Continuous Electron Beam Accelerator Facility, May 26-June 12, 1998.
- [4] H.J. Rothe. *Lattice gauge theories: an introduction*. World Scientific, 2005.
- [5] S. Scherer. *Introduction to chiral perturbation theory*. In *Advances in Nuclear Physics*, volume 27.
- [6] C.D. Roberts and A.G. Williams. *Dyson-Schwinger equations and their application to hadronic physics*. *Prog. Part. Nucl. Phys.*, **33**:477–575, 1994.
- [7] M.S. Bhagwat, M.A. Pichowsky, C.D. Roberts and P.C. Tandy. *Analysis of a quenched lattice-QCD dressed-quark propagator*. *Phys. Rev. C*, **68**:015203, 2003.
- [8] S.J. Brodsky and G.F. de Téramond. *AdS/QCD, light-front holography, and color confinement*. Xth quark confinement and the hadron spectrum, October 8-12, 2012, TUM campus Garching, Munich, Germany.
- [9] J.D. Bjorken. *Asymptotic sum rules at infinite momentum*. *Phys. Rev.*, **179**:1547–1553, 1969.

-
- [10] D.J. Gross and F. Wilczek. *Ultraviolet behavior of non-abelian gauge theories*. Phys. Rev. Lett., **30**:1343–1346, 1973.
- [11] H.D. Politzer. *Reliable perturbative results for strong interactions?* Phys. Rev. Lett., **30**:1346–1349, 1973.
- [12] N. Isgur and J.E. Paton. *A flux tube model for hadrons in QCD*. Phys. Rev. D, **31**:2910–2929, 1985.
- [13] J.-P. Chen, A. Deur and Z.-E. Meziani. *Sum rules and moments of the nucleon spin structure functions*. Mod. Phys. Lett. A, **20**(36):2745–2765, 2005.
- [14] R.G. Edwards, J.J. Dudek, D.G. Richards and S.J. Wallace. *Excited state baryon spectroscopy from lattice QCD*. Phys. Rev. D, **84**:074508, 2011.
- [15] A.M. Sandorfi. *Unravelling the excitation spectrum of the nucleon*. J. Phys.: Conf. Ser., **424**(1):012001, 2013.
- [16] M. Bellis, V. Crede, S. Strauch *et al.* *Measurement of $\pi^+\pi^-$ photoproduction in double-polarization experiments using CLAS*. Jefferson Lab experiment proposal E06-013.
- [17] C.D. Keith *et al.* *A polarized target for the CLAS detector*. Nucl. Instrum. Meth. A, **501**(23):327 – 339, 2003.
- [18] X. Wei *et al.* *New improvements leading to higher polarization frozen spin HD targets at the LEGS facility*. Nucl. Instrum. Meth. A, **526**:157–162, 2004.
- [19] F.J. Klein, A.M. Sandorfi *et al.* *N^* resonances in pseudoscalar-meson photo-production from polarized neutrons in $\vec{H}\vec{D}$ and a complete determination of the $\gamma n \rightarrow K^0\Lambda$ amplitude*. Jefferson Lab experiment proposal E06-101/g14.
- [20] S.D. Drell and T.-M. Yan. *Massive lepton-pair production in hadron-hadron collisions at high energies*. Phys. Rev. Lett., **25**:316–320, 1970.
- [21] S.D. Drell and T.-M. Yan. *Massive lepton-pair production in hadron-hadron collisions at high energies*. Phys. Rev. Lett., **25**:902–902, 1970.

-
- [22] A.W. Thomas and W. Weise. *The structure of the nucleon*. Wiley, 2001.
- [23] V. Breton and H. Fonvieille. *La nature de la sonde électromagnétique*. 11ème école internationale Joliot-Curie de physique nucléaire, IN2P3, 1992.
- [24] A. Deur. *Étude expérimentale de la structure en spin du neutron (^3He) à bas Q^2 : Une connexion entre les règles de somme de Bjorken et Gerasimov-Drell-Hearn*. Ph.D. thesis, Université Blaise Pascal, 2000.
- [25] B. Frois. *Les grandes lignes du programme de recherches à CEBAF*. 11ème école internationale Joliot-Curie de physique nucléaire, IN2P3, 1992.
- [26] M. Diehl and S. Sapeta. *On the analysis of lepton scattering on longitudinally or transversely polarized protons*. Eur. Phys. J. C, **41**(4):515–533, 2005.
- [27] J. Pierce, J. Maxwell *et al.* *Dynamically polarized target for the g_2^p and G_E^p experiments at Jefferson Lab*. ArXiv:1305.3295, 2013.
- [28] W.A. Tobias. *Measurement of the proton and deuteron spin structure functions g_1 and g_2* . Ph.D. thesis, University of Virginia, 2001.
- [29] W.C. Chen, T.R. Gentile, C.B. Fu, S. Watson, G.L. Jones, J.W. McIver, D.R. Rich *et al.* *Polarized ^3He cell development and application at NIST*. J. Phys.: Conf. Ser., **294**(1):012003, 2011.
- [30] M. Bassan, S. Bouchigny, C. Commeaux, J.-P. Didelez, G. Rouillé, C. Schaerf *et al.* *Static and dynamic polarization of HD*. Nucl. Instrum. Meth. A, **526**(12):163 – 167, 2004.
- [31] M. Tanaka, J.-P. Didelez, G. Rouillé *et al.* *Polarized HD target for future LEPS experiments at SPring-8 in Japan*. Int. J. Mod. Phys. E, **19**(05n06):903–914, 2010.
- [32] M. Romalis. *Laser polarized ^3He target used for a precision measurement of the neutron spin structure*. Ph.D. thesis, Princeton University, 1997.
- [33] A. Honig. *Highly spin-polarized proton samples—large, accessible, and simply produced*. Phys. Rev. Lett., **19**:1009–1010, 1967.

-
- [34] M.C. Gupta. *Statistical Thermodynamics*. New Age International (P) Limited, 1990.
- [35] C.S. Whisnant, P.A. Hansen and T.D. Kelley. *Measuring the relative concentration of H_2 and D_2 in HD gas with gas chromatography*. Rev. Sci. Instrum., **82**(2):024101, 2011.
- [36] T. Ohta *et al.* *Distillation of hydrogen isotopes for polarized HD targets*. Nucl. Instrum. Meth. A, **664**(1):347 – 352, 2012.
- [37] A. D’Angelo *et al.* *HD gas distillation and analysis for HD frozen spin targets*. In *Polarized Sources, Targets and Polarimetry*, pages 123–130, 2011.
- [38] C.D. Bass *et al.* *A portable cryostat for the cold transfer of polarized solid HD targets: HDice-I*. Nucl. Instrum. Meth. A, **737**(0):107 – 116, 2014.
- [39] K. Halbach. *Design of permanent multipole magnets with oriented rare earth cobalt material*. Nucl. Instrum. Meth., **169**(1):1 – 10, 1980.
- [40] N. Craig and T. Lester. *Hitchhiker’s guide to the dilution refrigerator*. Technical report, Marcus Lab, Harvard University, 2004.
- [41] A.M. Sandorfi. *Energy-loss materials around HD targets in the In-Beam-Cryostat (IBC) used for g14*. Technical report, Thomas Jefferson National Accelerator Facility, 2012.
- [42] L. Emsley. *Spin Diffusion for NMR Crystallography*. eMagRes, 2009.
- [43] H. Mano and A. Honig. *Resistance of solid HD polarized-proton targets to damage from high-energy proton and electron beams*. Nucl. Instrum. Meth., **124**(1):1 – 10, 1975.
- [44] M. Steigerwald. *MeV Mott polarimetry at Jefferson Lab*. AIP Conf. Proc., **570**(1):935–942, 2001.
- [45] P.S. Cooper, M.J. Alguard, R.D. Ehrlich, V.W. Hughes, H. Kobayakawa *et al.* *Polarized electron-electron scattering at GeV energies*. Phys. Rev. Lett., **34**:1589–1592, 1975.

-
- [46] N. Falletto *et al.* *Compton scattering off polarized electrons with a high-finesse Fabry-Pérot cavity at JLab.* Nucl. Instrum. Meth. A, **459**(3):412 – 425, 2001.
- [47] C. Yan *et al.* *Beam raster system at CEBAF.* In *Particle Accelerator Conference, 1993., Proceedings of the 1993*, pages 3103–3105, 1993.
- [48] D.I. Sober *et al.* *The bremsstrahlung tagged photon beam in hall B at JLab.* Nucl. Instrum. Meth. A, **440**(2):263 – 284, 2000.
- [49] B.A. Mecking *et al.* *The CEBAF large acceptance spectrometer (CLAS).* Nucl. Instrum. Meth. A, **503**(3):513 – 553, 2003.
- [50] J. O’Meara *et al.* *A superconducting toroidal magnet for the CEBAF large acceptance spectrometer.* IEEE T. Magn., **25**(2):1902–1905, 1989.
- [51] M.D. Mestayer *et al.* *The CLAS drift chamber system.* Nucl. Instrum. Meth. A, **449**(12):81 – 111, 2000.
- [52] G. Adams *et al.* *The CLAS Cherenkov detector.* Nucl. Instrum. Meth. A, **465**(23):414 – 427, 2001.
- [53] E.S. Smith *et al.* *The time-of-flight system for CLAS.* Nucl. Instrum. Meth. A, **432**(23):265 – 298, 1999.
- [54] M. Amarian *et al.* *The CLAS forward electromagnetic calorimeter.* Nucl. Instrum. Meth. A, **460**(23):239 – 265, 2001.
- [55] C. Thorn and A. Caracappa. *Precision HD polarimetry with the LEGS crossed-coil NMR polarimeter.* AIP Conf. Proc., 2008.
- [56] J.A. de Zwart, P.J. Ledden, P. Kellman, P. van Gelderen and J.H. Duyn. *Design of a SENSE-optimized high-sensitivity MRI receive coil for brain imaging.* Magnet. Reson. Med., **47**(6):1218–1227, 2002.
- [57] J.T. Vaughan, G. Adriany, C.J. Snyder, J. Tian, T. Thiel *et al.* *Efficient high-frequency body coil for high-field MRI.* Magnet. Reson. Med., **52**(4):851–859, 2004.

-
- [58] Computer Simulation Technology (CST), CST Design Studio, <http://www.cst.com/Content/Products/DS/Overview.aspx>.
- [59] S. Hoblit, A.M. Sandorfi *et al.* *Measurements of polarized photo-pion production on longitudinally polarized HD and implications for convergence of the GDH integral*. Phys. Rev. Lett., **102**:172002, 2009.
- [60] E.C. Titchmarsh. *Introduction to the Theory of Fourier Integrals*. Clarendon Press, 1937.
- [61] S. Kak. *The discrete Hilbert transform*. P. IEEE, **58**(4):585–586, 1970.
- [62] A. Deur. *Description and polarimetry of the HDice reference targets (and test of the oxford PD power supply)*. Technical report, Thomas Jefferson National Accelerator Facility, 2011.
- [63] A. Deur. Personal communication.
- [64] A.M. Sandorfi, A. Deur, M. Lowry, X. Wei and C.D. Bass. *Summary of the February 2012 and March 2012 eHD test run*. Technical report, Thomas Jefferson National Accelerator Facility, 2013.
- [65] A. Deur. *Analysis of the electron beam tests done during g14*. Technical report, Thomas Jefferson National Accelerator Facility, 2013.
- [66] V. Sulkosky. *The spin structure of ^3He and the neutron at low Q^2 : A measurement of the generalized GDH integrand*. Ph.D. thesis, College of William and Mary, 2007.
- [67] J. Alcorn *et al.* *Basic instrumentation for Hall A at Jefferson Lab*. Nucl. Instrum. Meth. A, **522**(3):294 – 346, 2004.
- [68] A. Deur. *Single arm Monte Carlo for polarized ^3He experiments in Hall A*. Technical report, Université Blaise Pascal, 2000.
- [69] Continuous Electron Beam Accelerator Facility and Southeastern Universities Research Association (U.S.) and Joint IN2P3-IRF Commission. *Research program at CEBAF (II): report of the 1986 Summer Study Group, June 2-August*

- 29, 1986. Continuous Electron Beam Accelerator Facility, 1987.
- [70] H. Avakian, V. Burkert, L. Elouadrhiri, M. Guidal, M. Lowry, L. Pappalardo, S. Procureur *et al.* *Deeply virtual Compton scattering at 11 GeV with transversely polarized target using the CLAS12 detector*. Jefferson Lab experiment proposal PR12-12-010.
- [71] H. Avakian, A. Courtoy, K. Griffioen, S. Pereira, M. Radici *et al.* *Measurement of transversity with dihadron production in SIDIS with transversely polarized target*. Jefferson Lab experiment proposal PR12-12-009.
- [72] J. Annand, T. Averett, G. Cates, N. Liyanage, Z.-E. Meziani, G. Rosner, B. Wojtsekhowski, X. Zheng *et al.* *Measurement of neutron asymmetry A_1^n in the valence quark region using 8.8 GeV and 6.6 GeV beam energies and Bigbite spectrometer in Hall A*. Jefferson Lab experiment proposal E12-06-122.
- [73] G. Cates, S. Riordan, B. Wojtsekhowski *et al.* *Measurement of the neutron electromagnetic form factor ratio G_E^n/G_M^n at high Q^2* . Jefferson Lab experiment proposal E12-09-016.
- [74] G. Cates, E. Cisbani, G. Franklin, B. Wojtsekhowski *et al.* *Measurement of the semi-inclusive π and K electro-production in DIS regime from transversely polarized ^3He target with the SBS&BB spectrometers in Hall A*. Jefferson Lab experiment proposal E12-09-018.
- [75] J.-P. Chen, H. Gao, X. Jiang, J.-C. Peng, X. Qian *et al.* *An update to PR12-09-014: Target single spin asymmetry in semi-inclusive deep-inelastic electro pion production on a transversely polarized ^3He target at 8.8 and 11 GeV*. Jefferson Lab experiment proposal E12-10-006.
- [76] J.-P. Chen, J. Huang, Y. Qiang, W. Yan *et al.* *Asymmetries in semi-inclusive deep-inelastic electro-production of charged pion on a longitudinally polarized ^3He target at 8.8 and 11 GeV*. Jefferson Lab experiment proposal E12-11-007.
- [77] G. Cates, J.-P. Chen, Z.-E. Meziani, X. Zheng *et al.* *Measurement of neutron spin asymmetry A_1^n in the valence quark region using an 11 GeV beam and a polarized ^3He target in Hall C*. Jefferson Lab experiment proposal E12-06-110.

Abstract

The study of the nucleon structure has been a major research focus in fundamental physics in the past decades and still is the main research line of the Thomas Jefferson National Accelerator Facility (Jefferson Lab). For this purpose and to obtain statistically meaningful results, a highly efficient polarized target is essential. This means high polarization and high relative density of polarized material. This dissertation presents the principles and usage procedures of a Hydrogen Deuteride (HD) target that presents both such characteristics. Although the HD target has been shown to work successfully under a high intensity photon beam, it remained to be seen if the target could stand an electron beam of reasonably high current (nA). In this perspective, the HD target was tested for the first time in its “frozen spin” mode under an electron beam during the g14 experiment in the Jefferson Lab’s Hall B in 2012. Two methods of polarimetry are also discussed in this dissertation: one with Nuclear Magnetic Resonance of this HD target during the electron beam tests, and another with the elastic scattering of electrons off a polarized target by using data taken on helium-3 during the E97-110 experiment that occurred in Jefferson Lab’s Hall A in 2003.

Keywords: Polarimetry, Nuclear Magnetic Resonance, NMR, Polarized Target, Hydrogen Deuteride, HD, Helium-3

Résumé

L’étude de la structure du nucléon est un sujet actif de la recherche et un des objectifs majeurs du Thomas Jefferson National Accelerator Facility (Jefferson Lab). Dans cette optique et afin d’obtenir des résultats statistiquement significatifs, il est essentiel d’avoir une cible polarisée ayant à la fois une haute polarisation et une densité de matériel polarisé élevée. Cette thèse présente les principes et utilisations d’une cible de deutéride d’hydrogène (ou cible de HD) qui remplit les deux conditions précédemment énoncées. Bien qu’il ait été prouvé que la cible de HD pouvait être utilisée avec succès sous un faisceau de photons de haute intensité, il restait à montrer si elle pouvait résister un faisceau d’électrons de courant relativement élevé (nA). Dans ce but, la cible de HD a été testée pour la première fois dans son mode de “spin gelé” sous un faisceau d’électrons pendant l’expérience g14 dans le Hall B de Jefferson Lab en 2012. Deux méthodes de polarimétrie sont également décrites dans cette thèse: une par Résonance Magnétique Nucléaire appliquée à la cible de HD pendant les tests sous un faisceau d’électrons, et une autre utilisant la réaction de diffusion élastique d’un faisceau d’électrons sur une cible en utilisant des données élastiques sur l’hélium-3 prises en 2003 pendant l’expérience E97-110 dans le Hall A de Jefferson Lab.

Mots clés: Polarimétrie, Résonance Magnétique Nucléaire, RMN, Cible Polarisée, Deutéride d’Hydrogène, HD, Hélium-3